β-relaxation and Its Correlations with Spatial Heterogeneity and Mechanical Properties of Metallic Glasses

Ph. D. Thesis

β-RELAXATION AND ITS CORRELATIONS WITH SPATIAL HETEROGENEITY AND MECHANICAL PROPERTIES OF METALLIC GLASSES

Fan Zhu

Department of Materials Science

Graduate School of Engineering

Tohoku University

Sendai, Japan

Jun 2015

Tohoku University

THESIS

SUBMITTED IN PARTIAL FULFILLMENT OF THE REQUIREMENTS FOR THE DEGREE OF DOCTOR OF PHILOSOPHY

TITLE

β-RELAXATION AND ITS CORRELATIONS WITH SPATIAL HETEROGENEITY AND MECHANICAL PROPERTIES OF METALLIC GLASSES

PRESENTED BY Fan ZHU (B2TD9505)

ACCEPTED BY Department of Materials Science

APPROVED BY THE ADVISORY COMMITTEE MEMBER

Prof. Mingwei CHEN

Prof. Junji SAIDA

Prof. Hidemi KATO

Abstract

Metallic glasses are amorphous metals or alloys showing glass transition when heated to their supercooled liquid regions. Commonly, there are two relaxation mechanisms involved with metallic glasses. One is the primary α-relaxation related to the glass transition and the other is the secondary β-relaxation. Recent studies indicate that the β-relaxations play important roles in physical aging, accelerated partial devitrification and deformation of metallic glasses. However, the underlying origin of the correlations has not been fully understood.

We performed sub-T_g relaxation on a hyper-quenched metallic glass. The excess enthalpy relaxation of the metallic glass annealed below ~0.8T_g (glass transition temperature) gave an activation energy $E_\beta = 27.2RT_g$ in accord with the empirical value for β-relaxations, demonstrating that the enthalpy released during the sub-T_g relaxation was mainly processed by β-relaxation.

We investigated the evolution of nanoscale spatial heterogeneity in a metallic glass during sub-T_g structural relaxation by utilizing the amplitude-modulation atomic force microscopy (AM-AFM). The successive shrinkage of spatial heterogeneity after the sub-T_g relaxation can be well expressed by the Kohlrausch-Williams-Watts (KWW) equation. The measured characteristic relaxation times and activation energy were close to those for β-relaxation.

The nanoindentation was used to measure the effects of sub-T_g relaxation on the mechanical properties of metallic glasses. Both the hardness and modulus increased after the sub-T_g relaxation. The creep of the samples after sub-T_g relaxation showed

the deterioration of relaxation amplitude and the slowing down of the response of rheology. The hardness and creep were found to have strong correlations with the sizes of spatial heterogeneity. The activation energy of the creep in hyper-quenched metallic glass was determined to be close to that for β-relaxation.

We introduced the scanning transmission electron microscopy (STEM) to directly observe the spatial heterogeneity in 14 kinds of metallic glasses of different compositions or conditions. The sizes of spatial heterogeneity observed using STEM were comparable with those measured by AM-AFM before and after the sub-T_g relaxation. The strong and fragile metallic glasses exhibited the opposite geometric features of spatial heterogeneity. The volumes of spatial heterogeneity determined the relative intensity of β-relaxations to α-relaxations. The higher volume and more isotropic geometry of strong regions could enhance the glass-forming abilities. The ABED mapping indicated that the spatial heterogeneity was more disordered than other parts in metallic glasses.

Our work correlated β-relaxation with the spatial heterogeneity and mechanical properties of metallic glasses. The STEM was introduced to see the spatial heterogeneity in metallic glasses. The spatial heterogeneity was determined to be the basic structural unit accounting for the dynamic and mechanical properties of metallic glasses. These findings will contribute to better understandings of dynamic, mechanical and other properties of metallic glasses, and facilitate the further investigations and developments of metallic glasses.

TABLE OF CONTENTS

Chapter 1.

Introduction

1.1 Glass

The definition of a glass is an amorphous solid which exhibits a glass transition [1]. It is easy to understand the amorphous solid which does not possess long-range order or periodicity and has certain viscosity as shown in **Fig. 1.1**. However, the glass transition is a unique feature of glassy materials distinguished from other materials, and still remains puzzling for researchers on glasses [2]. Phenomenally, the glass transition is a process where the supercooled liquid forms a glass below a certain temperature. Commonly, upon cooling below the melting point T_m, a liquid will transform to a crystalline solid which is thermodynamically stable. However, if the liquid is cooled sufficiently fast, the molecules or atoms in the liquid will have no enough time to rearrange themselves to sample thermal-equilibrium configurations and the crystallization can be avoided. The structure of the liquid seems to be frozen on the laboratory timescale and the resultant product is a glass.

The glass transition temperature T_g corresponds to a temperature at which the glass transition occurs. However, its value for one glass changes under different testing conditions and lies in a wide range. At a higher cooling rate (case b in **Fig. 1.2**), the glass transition will occur at a higher temperature, i.e. T_{gb} is larger than T_{ga}. The physical nature of glass transition is still in controversy.

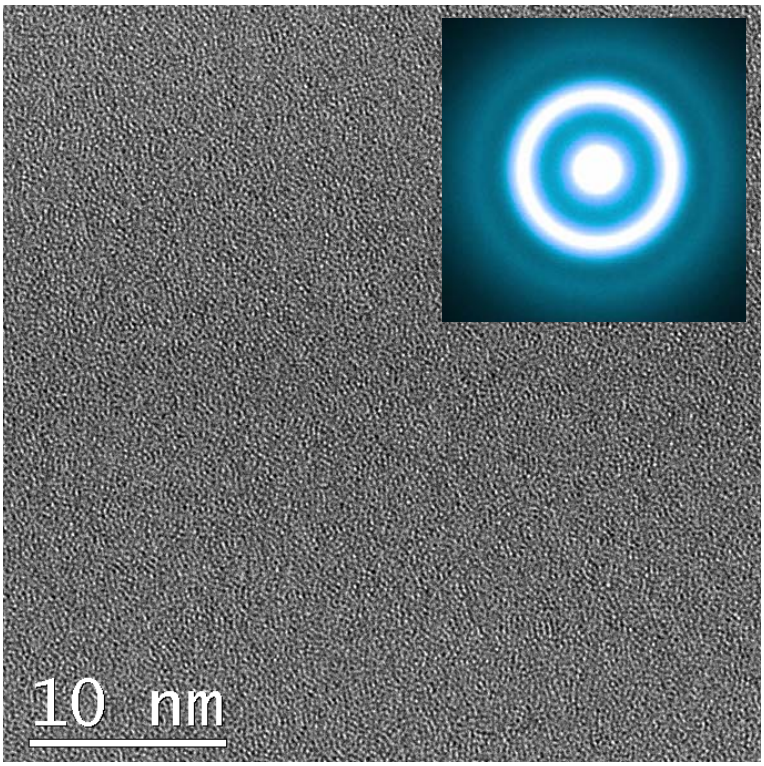

Fig. 1.1. Microstructure of a metallic glass showing a typical amorphous structure with no long-range order. The image was taken by high resolution transmission electron microscopy (HRTEM) and the inset is the corresponding diffraction halo.

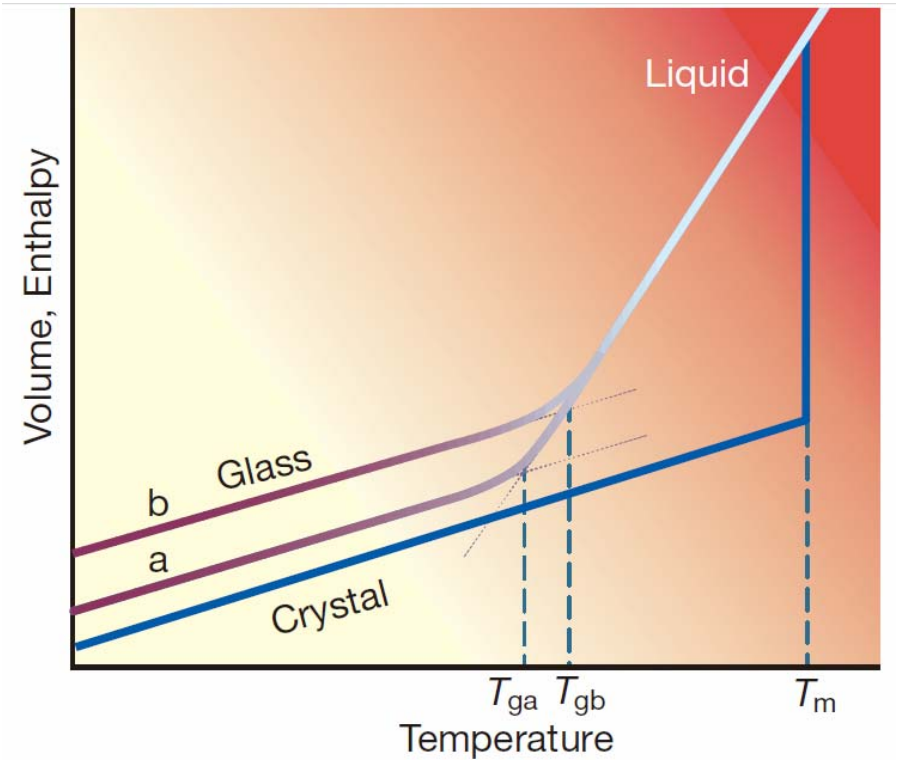

Fig. 1.2. A schematic of glass transition when a liquid is cooled below T_g. During the cooling the volume and enthalpy of the liquid will change depending on temperature. When glass transition occurs, the changing slop will continuously decrease to be close to that of a crystal. A slow cooling rate leads to a glass transition at T_{ga}, while a fast cooling rate leads to a glass transition at T_{gb}. (Adapted from ref. 2.)

1.2 Relaxations

If a system was applied by a perturbation, it tends to be in a new equilibrium by a set of processes [3, 4]. The temporal processes are called relaxations. Supercooled liquids or glasses also show relaxations, such as the time-dependent deformation in response to applied stress or the time-dependent stress in response to an imposed strain etc. Commonly, there are several relaxation mechanisms contributing to the temporal behavior of response to the external perturbation in supercooled liquids or glasses.

1.2.1 Decoupling

At different temperature regimes, the supercooled liquids or glasses will exhibit different relaxation mechanisms [4-7]. As shown in **Fig. 1.3**, at high enough temperature there is just one relaxation mechanism. However, when the liquid is cooled to the moderately supercooled regime, the single relaxation mechanism splits into slow α and fast β relaxations [5, 6]. While the α-relaxation behaves non-Arrhenius and disappears at T_g, the β-relaxation obeys the Arrhenius equation and continues below T_g.

1.2.2 α and β relaxations

α and β relaxations are two main relaxation processes involved with glasses [2]. The α-relaxation is also termed primary relaxation and believed to contribute to the glass transition. It can be expressed by the Vogel-Tammann-Fulcher (VFT) equation and disappears at T_g. The β-relaxation is also termed secondary relaxation and considered as a precursor to the α-relaxation. The β-relaxation remains in glasses below T_g.

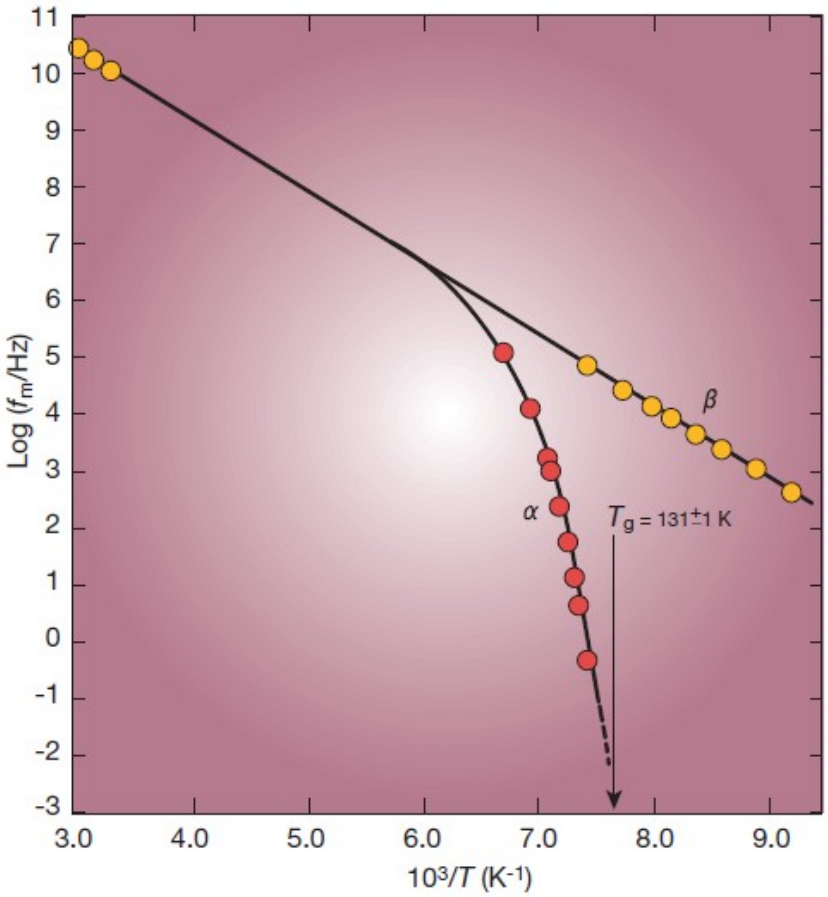

Fig. 1.3. The representative plot of the peak dielectric relaxation frequency of the glass forming mixture as functions of temperature. (Adapted from ref. 2.)

The α and β relaxations are envisaged to correspond to different atomic or molecular diffusion processes as shown in **Fig. 1.4** [8]. The diffusion via α-relaxation is processed by the cooperative motions of atoms or molecules and leads to the large scale diffusion (**Fig. 1.4a**). On the other hand, the β-relaxation corresponds to thermally-activated localized motions (**Fig. 1.4b**). As the temperature increases or the system becomes more ergodic, the percolation of localized β-relaxation will eventually give rise to the *a*-relaxation or glass transition.

1.2.3 KWW function

Near or below T_g, the relaxations in viscous liquids or glasses are non-exponential, which is in contrast with the behaviour of liquids above the melting point whose relaxations are simply exponential [2]. The Kohlrausch-Williams-Watts or KWW function [9, 10] is often used to describe such non-exponential temporal behavior of disordered systems in response to external stimulus, e.g. applied electric field, stress, and imposed deformation etc.. The KWW function has a form as expressed below:

$$\Delta F_{remain} / \Delta F_{total} = \exp\left[-(t/\tau)^{\beta_{KWW}}\right] \quad (1)$$

where ΔF_{reamin} is the measure quantity after relaxation for certain time t and ΔF_{total} is the initial quantity before the relaxation. τ is the characteristic relaxation time which can be used to evaluate the speed of the relaxation. β_{KWW} is the non-exponential parameter for fitting. The KWW function indicates a slowing down of the long-time relaxation near or below T_g. Nowadays this function has been applied on the enthalpy relaxation [11] and stress relaxation [12] of glasses.

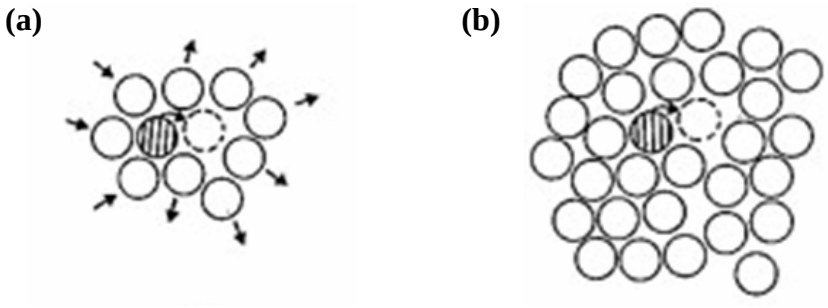

Fig. 1.4. An illustration for atomic or molecular diffusion of α-relaxation and β-relaxation in glasses. (a) Collective motions corresponding to α-relaxation. (b) Localized motions corresponding to β-relaxation. (Adapted from ref. 8.)

1.2.4 Spatially heterogeneous dynamics

The spatial heterogeneous dynamics have been proposed to explain the slowing down of dynamics in supercooled liquids and glasses [13]. In this scenario, the slow-down dynamics are attributed to the growth of distinct relaxing domains or spatially dynamic heterogeneity when a liquid is cooled below its melting point.

As show in **Fig. 1.5a** on the same timescale, the particles in some regions have a fixed structure while the particles in other regions have rearranged substantially, indicating different characteristic relaxation times of these regions. The dynamics in some regions can be much faster than those in other regions, and the intermediate regions exist between them (see **Fig. 1.5b**). These regions are termed spatial heterogeneity. Their sizes are evaluated to be several nanometers in dimension.

The KWW function indicative of the non-exponential relaxation can be derived based on the scheme of spatially heterogeneous dynamics. Relaxation in a given spatial heterogeneity might be exponential. However, the relaxation times vary from one spatial heterogeneity domain to another. The total relaxation behavior of the sample is an integration of the relaxations of the spatial heterogeneity domains. In mathematic, it can be expressed as

$$\int_0^\infty G(\tau)e^{-t/\tau}d\tau = \exp\left[-(t/\tau)^{\beta_{KWW}}\right] \quad (2)$$

where $G(\tau)$ represents a spatial distribution of relaxation times. The right side is the expression of KWW function which can be equal to the left side in mathematic. However, the origin of the existence of the spatial heterogeneity in supercooled liquids and glasses is still unclear.

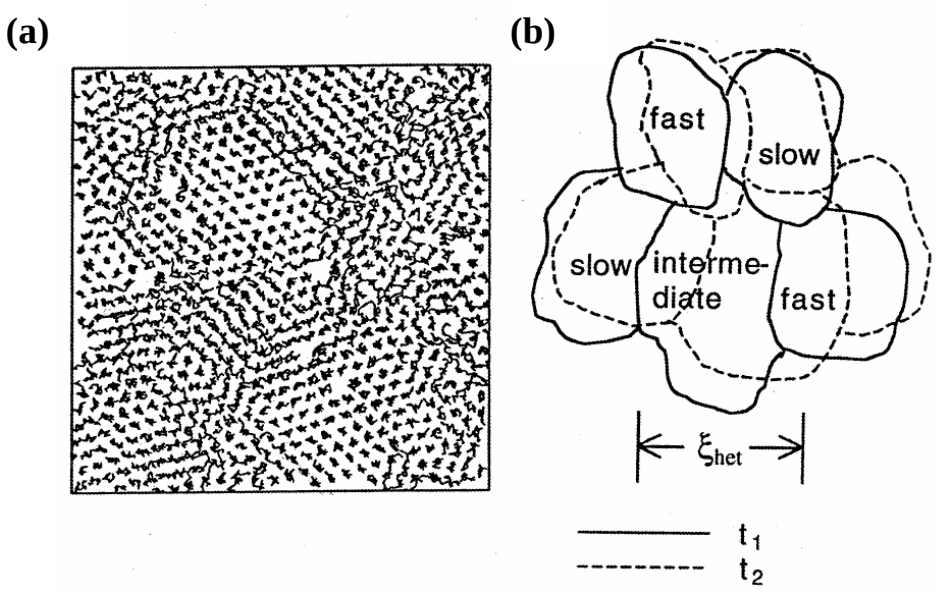

Fig. 1.5. Schematics of spatially heterogeneous dynamics. (a) Overlaid maps of particle positions at various times. (b) Illustration of spatially dynamic heterogeneity with different relaxation times. ξ_{het} indicates the dimension of the spatially dynamic heterogeneity. (Adapted from ref. 13.)

1.2.5 Fragility

Fragility is an important parameter for glasses proposed by C. A. Angell which is directly related to the slowing downing of the dynamics [2, 4]. **Fig. 1.6** is the plot of the shear viscosity η for glass-forming liquids of different kinds as a function of reduced coordinate T_g/T. One can see clear differences in curvature of the curves for the glass-forming liquids. Based on the plot, the fragility *m* can be defined as:

$$m = \frac{\partial \log \eta(T)}{\partial (T_g / T)}\Big|_{T=T_g} \tag{3}$$

which indicates how fast the viscosity increases with decreasing temperature approaching T_g where the structure of glass-forming liquid is arrested. The glass-forming liquids which have small curvature in the plot or small values of fragility are termed “strong” glass former. The “fragile” glass formers, however, show a rapid rising of curvature near T_g and result in large values of fragility.

The fragility implied the different structures for the strong and fragile glass-forming liquids responding to the temperature [4]. As the temperature increased or decreased, the structure of the strongest glass-forming liquids doesn’t change much and their plots behave obeying the Arrhenius fashion which means the activation energy for the thermal-activated process is independent of temperature before the structural arrest. The rapid rising of the curvature in the fragile glass-forming liquids comes from the destruction of the structure resulting in the super-Arrhenius behavior which means the activation energy for the thermal-activated process increases with the decreasing temperature [2].

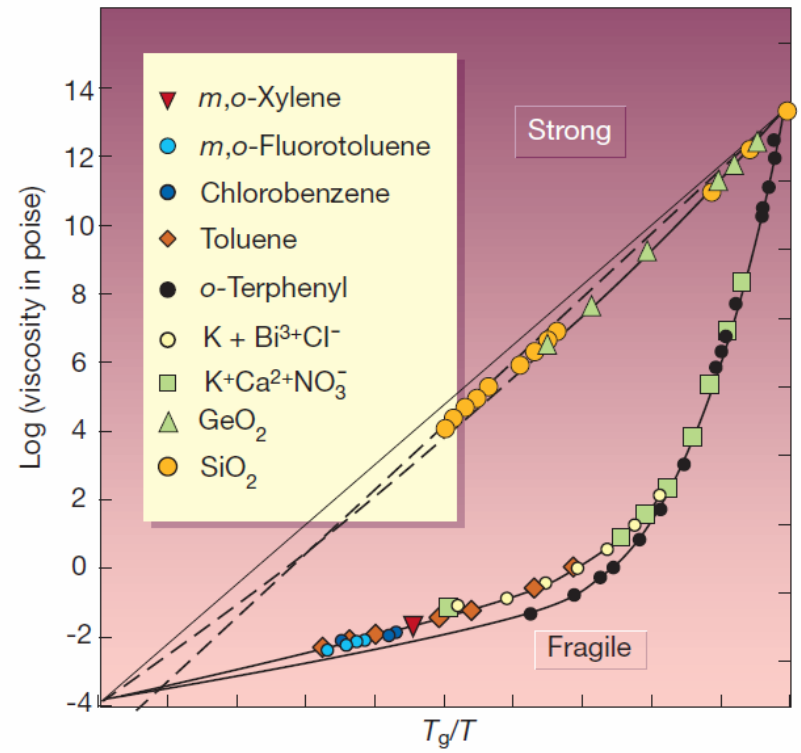

Fig. 1.6. T_g-scaled Arrhenius representation of liquid viscosities showing Angell's strong-fragile pattern. (Adapted from ref. 2.)

1.3 Metallic glass

Although people have discovered and utilized glasses for more than two thousand years, glasses produced from melting metals are thought to be impossible until 1959 [14-17]. At Caltech Prof. Pol Duwez and his Ph.D. students William Klement and Ron Willens fabricated non-crystalline alloys based on Gold and Silicon using splat quenching [14]. Since then, the metallic glasses have aroused more and more interests from researchers and developed significantly for extensive applications across many fields.

The developments of metallic glasses go through two peaks [17]. The first one is from 1960 to 1980. After the first report of Au-Si non-crystalline alloys in 1960s, even Prof. Duwez himself doesn't believe them as metallic glasses. 8 to 9 years later, H. S. Chen and David Turnbull at Harvard University reported the existences of glass transition in Au-Ge-Si and Pd-Si amorphous alloys, confirming them as glassy materials [18, 19]. And then the term metallic glass was accepted. In 1971, H. S. Chen *et al.* produced Fe-base metallic glasses with superior soft magnetism and efficient electrode, and commercialized them as the materials for electrical transformer [20].

The second peak started at the end of 1980s with the discovery of bulk metallic glasses [21-24]. The traditional metallic glasses composed of two to three elements need a critical cooling rate higher than 10^3 K/s and therefore their dimensions are limited to ribbons or strips. The groups led by A. Inoue at Tohoku University and W. L. Johnson at Caltech developed multi-component metallic glasses with a critical cooling rate less than 1 K/s, and now they can be produced as large as 8 cm [25]. In 2014, the bulk metallic glass appears in iPhone as the logo of Apple (see **Fig. 1.7**).

Fig. 1.7. Metallic glass applied as the shining Apple logo in iPhone 6 and 6 plus. The metallic glasses have much smoother and brighter finish than the crystalline metals. (Adapted from Apple Inc..)

1.4 β-relaxation in metallic glasses

1.4.1 Its existence in metallic glasses

Whether the β-relaxations exist in metallic glass or not is unambiguous until a recent decade [6, 26-34]. The reason is that in metallic glass the basic units are rigid atoms rather than the flexible molecules in some other glasses. The origin of β-relaxation process in some molecular glasses is commonly attributed to the small angle reorientational motion of molecules where part of each molecule is translationally displaced by rotation on the lattice site. However, it fails for metallic glasses in which the reorientation of spherical atoms can not contribute to translational motions for β-relaxations [6, 26].

In 1976, H. S. Chen *et al.* reported the secondary relaxation in structural relaxation spectrum of Pd-base metallic glasses (see **Fig. 1.8a**) [35]. He observed a low-temperature relaxation peak before the occurrence of glass transition and suggested there should be two distinct mechanisms involved with the structural relaxation in metallic glasses. Recently, the secondary relaxation peaks were also observed in dynamic mechanical analysis (DMA) for Pd-base [29-31] and Zr-base [32, 33] metallic glasses (see **Fig. 1.8b**).

Using the hyperquenching-annealing-calorimetric scan (HAC) approach, L. N. Hu and Y. Z. Yue *et al.* gave an answer that the activation energy and the characteristic relaxation time near T_g of the secondary relaxation in metallic glasses is in accord with the empirical value for the β-relaxations in various glass systems [11].

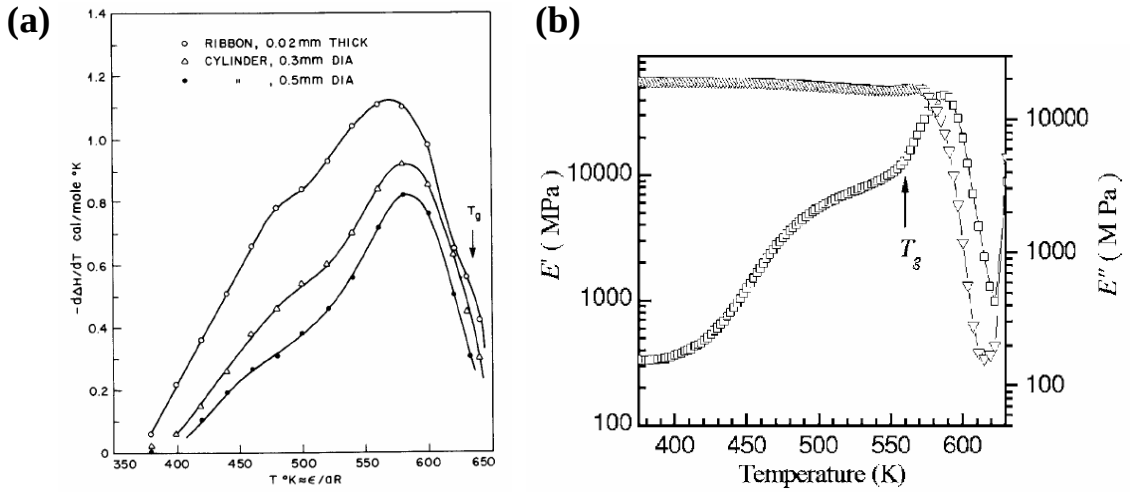

Fig. 1.8. Characterization of β-relaxations in metallic glasses. (a) Difference in the apparent specific heat of $Pd_{0.775}Cu_{0.06}Si_{0.165}$ glass between the annealed and as-quenched state for various quenching states. (b) Temperature dependence of the storage elastic modulus E' and the loss elastic modulus E of the as-cast $Pd_{40}Ni_{10}Cu_{30}P_{20}$ measured at 4 Hz at a heating rate of 3 K/min. (Adapted from ref. 31 and ref. 35.)

1.4.2 Structural origin of β-relaxation

G. P. Johari [26] has pointed out that the β-relaxation in mechanically rigid glasses, especially in metallic glasses, should be processed by the translational motion of atoms localized in loosely packed regions. In the mechanically rigid glasses, the β-relaxation can not be contributed by the reorientation of spheres about their axis alone, thus the translational motions of small molecules or atoms should take place. However, if all molecules or atoms were involved with such process an external stress will lead to a permanent macroscopic deformation at β-relaxation time scale which has never been observed. If the translational motions were confined to the spatial heterogeneity of loose packing, the above contradiction can be eliminated. The latest synchrotron X-ray investigations demonstrated that the process of β-relaxation in metallic glass was involved with short-range collective rearrangement of large solvent atoms by local cooperative bonding switch (**Fig. 1.9**) [36].

1.4.3 Empirical value of activation energy

The activation energy of β-relaxations were found to have a simple relation with their glass transition temperatures that $E_\beta = 26RT_g$ [11, 37-40]. This empirical relation was first discovered in organic glasses [38-40]. Later K. L. Ngai [37] provided a theoretic explanation for the relation based on the model coupling. L. N. Hu and Y. Z. Yue *et al.* [11] found the empirical relation can be also applied on metallic glasses as shown in **Fig. 1.10**. The ratio between the activation energies and the corresponding RT_g of Fe-base, Pd-base, Zr-base and other metallic glasses are almost a constant around 26.1.

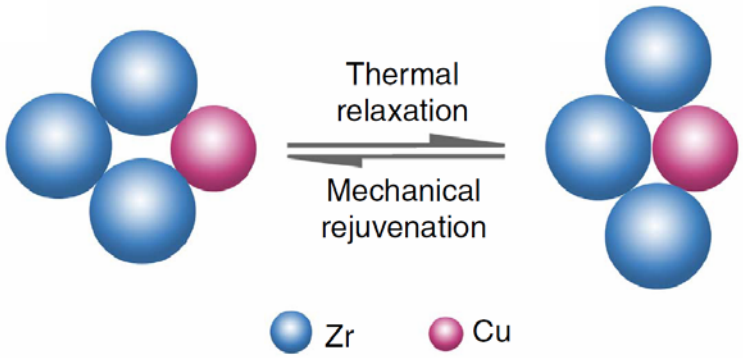

Fig. 1.9. Schematic of β-relaxation by local bonding switch. The β-relaxation was processed by the break of Zr-Zr bonding and the formation of Zr-Cu bonding. (Adapted from ref. 36.)

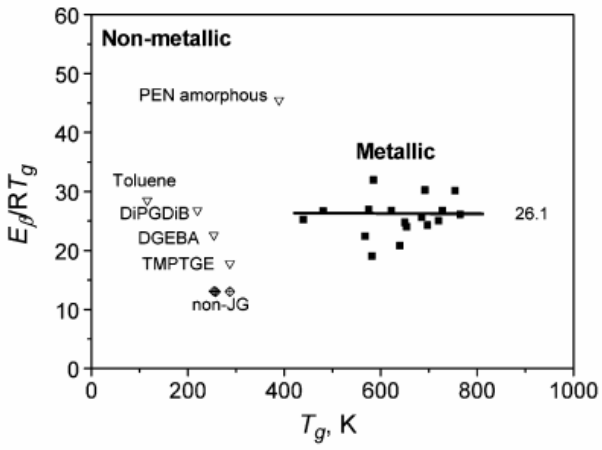

metallic glasses	E_β, kJ/mol	T_g, K
$(Fe_{0.85}Ni_{0.15})_{83}P_{17}$	134	650
$(Fe_{0.85}Cr_{0.15})_{83}P_{17}$	150	720
$(Fe_{0.85}V_{0.15})_{83}P_{17}$	162	728
$(Fe_{0.85}Mo_{0.15})_{83}P_{17}$	189	754
$(Fe_{0.75}Ni_{0.25})_{83}P_{17}$	111	640
$(Fe_{0.75}Co_{0.25})_{83}P_{17}$	146	685
$(Fe_{0.75}Mn_{0.25})_{83}P_{17}$	141	697
$(Fe_{0.75}Cr_{0.25})_{83}P_{17}$	166	765
$(Fe_{0.5}Ni_{0.5})_{83}B_{17}$	172	650
$(Fe_{0.5}Ni_{0.5})_{83}P_{17}$	154	645
$Pd_{48}Ni_{32}P_{20}$	92.4	582
$Al_{82}Ni_{10}Ce_8$	158	585
$Pd_{43}Ni_{10}Cu_{27}P_{20}$[a]	105.9	568
$Pd_{40}Ni_{10}Cu_{30}P_{20}$[a]	128.9	575
$Zr_{46.75}Ti_{8.25}Cu_{7.5}Ni_{10}Be_{27.5}$[a]	138.4	628
$Zr_{65}Cu_{15}Ni_{10}Al_{10}$[a]	130.8	654
$(Cu_{50}Zr_{50})_{92}Al_8$[a]	174.1	692
$La_{57.5}(Cu_{50}Ni_{50})_{25}Al_{17.5}$[a]	92.4	435

Fig. 1.10. The ratios between the activation energy and RT_g for various kinds of metallic glasses. (Adapted from ref. 11.)

1.5 β-relaxation and deformation

For the last ten years, more and more experimental results have supported β-relaxation as the origin of deformation in metallic glasses [41-44]. The stress-strain response in a metallic glass-forming liquid deformed to different strains attributed the reversible anelastic deformation to the configurational hopping by β-relaxation [42]. Moreover, a La-based metallic glass possessing strong β-relaxation was reported to show a pronounced macroscopic tensile plasticity [43].

1.5.1 Deformation mechanism

Metallic glasses show high strength well in excess of their crystalline counterparts as a result of the non-periodic microstructure and the absence of dislocation-based flow [45-50]. At a temperature far below T_g, the metallic glasses deform by shear banding, a highly localized shearing plane zone embedded in the undeformed matrix as shown in **Fig. 1.11a** [51-55]. Since 1970s several theories have been proposed to explain the plastic deformation in metallic glasses [51-53, 56]. These models are mainly based on two atomic-scale mechanisms: one is the stress-driven individual atomic jump termed free volume [51], and the other one is the local shear transformation (ST) by the cooperative shearing of atomic clusters which exist instantaneously during the transformation [52]. The cooperative shearing model (CSM) assumed the pre-existence of shear transformation zones (STZs) including certain number of atoms with loose packing as the fundamental unit of plasticity (**Fig. 1.11b**) [53, 56]. The STZ volume has been determined to be several nanometers using the rate-jump nanoindentation. [57]

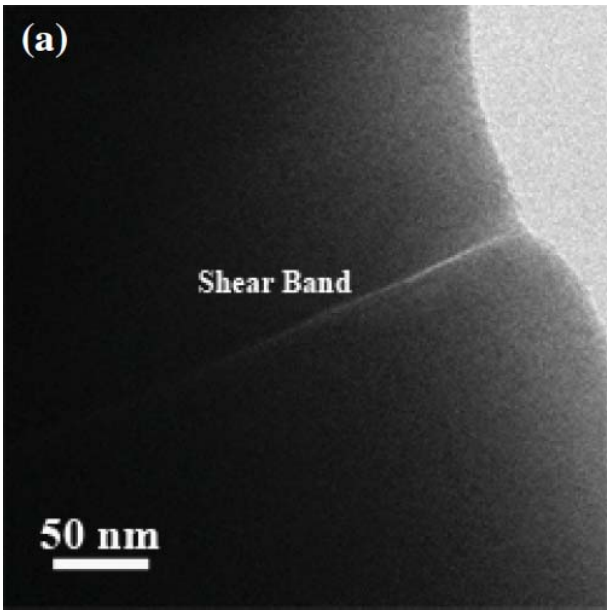

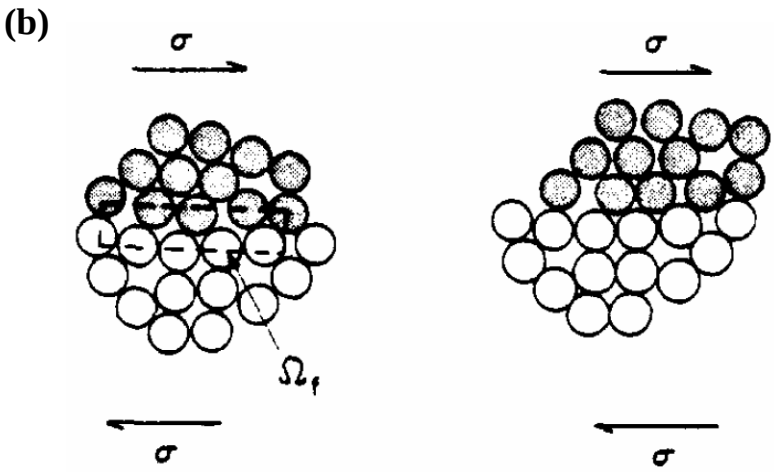

Fig. 1.11. (a) TEM observation of shear band in a deformed $Zr_{50}Cu_{50}$ bulk metallic glass. (Adapted from ref. 54.) (b) A schematic of shear transformation zone at low temperature. The plastic deformation in metallic glass was realized by the transition from one relatively stable configuration to the second one. (Adapted from ref. 51.)

1.5.2 β-relaxation and STZs

The systematic analysis on the potential-energy barrier of STZs and the activation energy of β-relaxation has showed equivalence between them for various kinds of metallic glasses (**Fig. 1.12**) [44]. This is the most convincing evidence for the correlation between β-relaxation and deformation mechanism in metallic glasses.

1.6 Heterogeneity observed in metallic glasses

Spatial heterogeneity is a concept proposed to explain the slowing down of dynamics in glass-forming liquids and glasses near their T_g [13]. G. P. Johari used a similar concept "density fluctuation" to explain the β-relaxations in rigid small molecular or atomic glasses [26]. The concept of STZs, cluster of atoms with loose packing, was assumed to play as the deformation unit for metallic glasses [51, 53, 56]. All these models envisaged the pre-existing of spatial or structural heterogeneity in glasses which accounts for the properties of glasses. It is intriguing to characterize such heterogeneity in glasses by some methods [13].

The atomic force microscopy (AFM) has been proven to be a useful tool to characterize the local elastic heterogeneity [58] or nanoscale viscoelastic heterogeneity (**Fig. 1.13**) in metallic glasses [59, 60]. Besides AFM, the nanoscale density fluctuation was detected by H. Okuda *et al.* in a quenched Zr-Cu-Ni-Al metallic glass using the anomalous small angle X-ray scattering (ASAXS) [61]. A partially crystallized Pd-Cu-Ni-P metallic glass induced by the ultrasonic annealing showed a pattern composed of nanoscale crystals and amorphous solids [62].

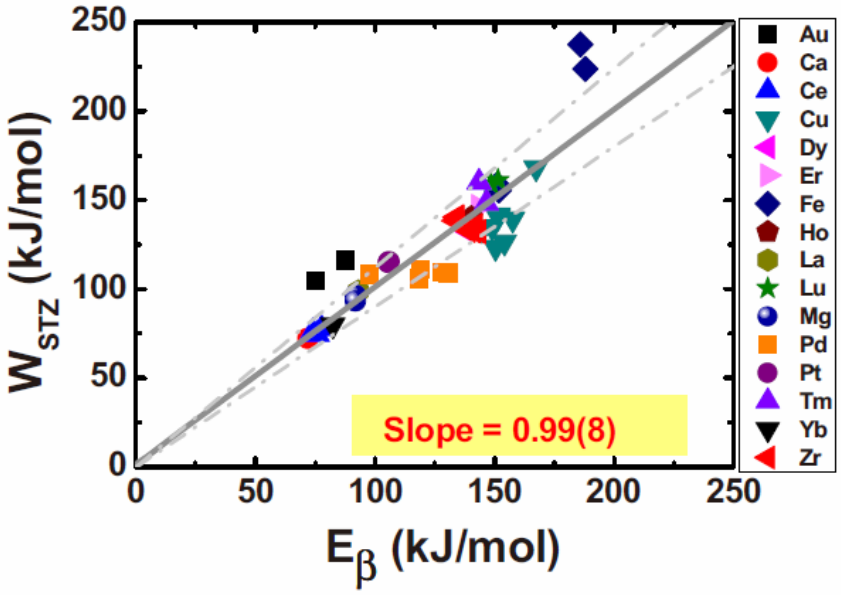

Fig. 1.12. The plot of energy barrier of STZs as a function of the corresponding activation energy of β-relaxation for various kinds of metallic glasses showing equivalence between them. (Adapted from ref. 44.)

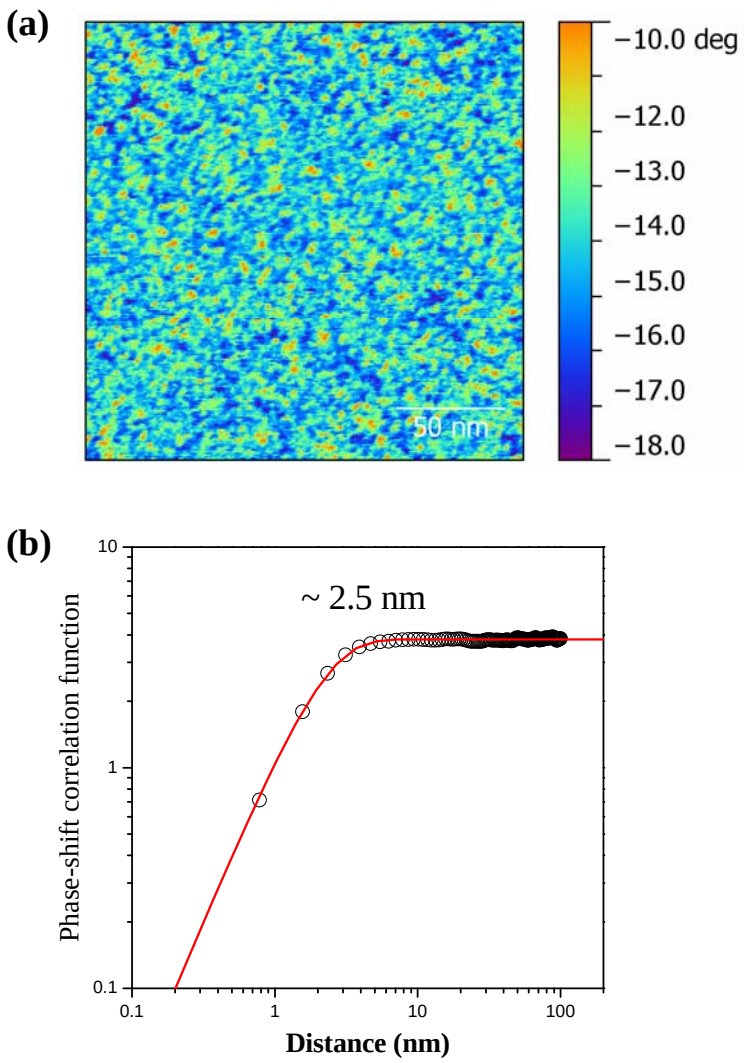

Fig. 1.13. Nanoscale spatial heterogeneity in metallic glass. (a) The phase shift image of a $Zr_{55}Cu_{30}Ni_5Al_{10}$ metallic glass. (b) The correlation function for the phase shift image gives an estimation of around 2.5 nm for the size of spatial heterogeneity in metallic glass. (Adapted from ref. 59.)

1.7 Objectives of this research

The β-relaxation in metallic glasses is the focus of our research (**Fig. 1.4**). It plays as the principal source of dynamics in glasses below T_g. However its importance has not been fully realized. In the later chapters we will show that the β-relaxation contributes to the enthalpy relaxation below T_g, strongly correlates with the spatial heterogeneity and dominates the mechanical behaviors of metallic glasses. The structural origin of β-relaxation will be investigated by the scanning transmission electron microscopy (STEM) and Angstrom-beam electron diffraction (ABED).

The background of glasses, dynamics, β-relaxation, metallic glasses, deformation mechanisms and spatial heterogeneity were presented in chapter 1.

The experiment methods and details were introduced in chapter 2.

The enthalpy relaxation in a hyper-quenched metallic glass below T_g was studied in chapter 3 and utilized as a probe to tune the intensity of β-relaxation.

In chapter 4, the evolution of spatial heterogeneity during the sub-T_g relaxation was characterized by the amplitude-modulation dynamic atomic microscopy.

In chapter 5, the mechanical properties and creep behaviors of metallic glass after sub-T_g relaxation were measured using the nanoindentation.

In chapter 6, the STEM was introduced to directly observe the spatial heterogeneity. The correlations of spatial heterogeneity with sub-T_g relaxation, fragility, β-relaxation and glass-forming ability were investigated.

In the last chapter, the general conclusions of the key findings of chapters 3, 4, 5 and 6 will be summarized.

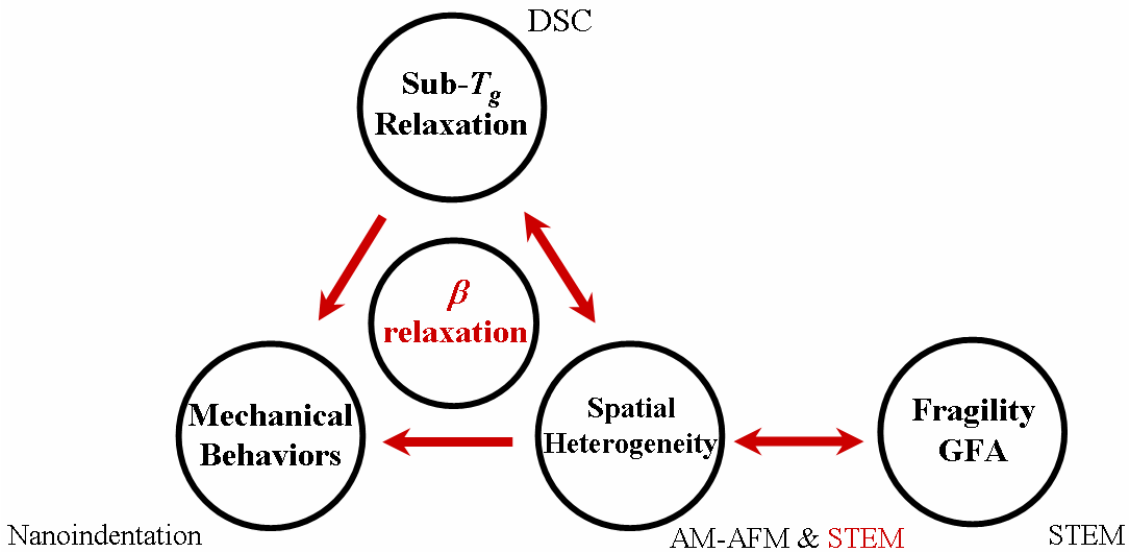

Fig. 1.14. Structure of the dissertation. This dissertation focused on the β-relaxation. Its correlations with the sub-T_g relaxation, spatial heterogeneity and mechanical behaviors were investigated and discussed. The correlations of spatial heterogeneity with fragility and glass-forming ability (GFA) were also studied.

References

[1] S. R. Elliott, Physics of amorphous materials, Longman, New York, USA (1984).

[2] P. G. Debenedetti, and F. H. Stillinger, Nature 410, 259 (2001).

[3] E. Donth, The glass transition: relaxation dynamics in liquids and disordered materials, Springer (2011).

[4] C. A. Angell, K. L. Ngai, G. B. McKenna, P. F. McMillan and S. W. Martin, J. Appl. Phys. 88, 3113 (2000).

[5] G. P. Johari, J. Chem. Phys. 58, 176 (1973).

[6] G. P. Johari, and M. Goldstein, J. Chem. Phys. 53, 2372 (1970).

[7] E. Rossler, U. Warschewske, P. Eiermann, A. P. Sokolov and D. Quitmann, J. Non-Cryst. Solids 172, 113 (1994).

[8] G. P. Johari, J. Chim. Phys. 89, 2073 (1992).

[9] R. Kohlrausch, Ann. Phys. Chem. 91, 179 (1874).

[10] G. Williams, and D. C.Watts, Trans. Faraday Soc. 66, 80 (1970).

[11] L. Hu, and Y. Z. Yue, J. Phys. Chem. C 113, 15001 (2009).

[12] Z. Wang, B. A. Sun, H. Y. Bai and W. H. Wang, Nature Commun. 5, 5823 (2014).

[13] M. D. Ediger, Annu. Rev. Phys. Chem. 51, 99 (2000).

[14] W. Klement, R. H. Willens, and P. Duwez, Nature 187, 869 (1960).

[15] M. W. Chen, NPG Asia Mater. 3, 82 (2011).

[16] W. H. Wang, Prog. Phys. (CPS) 33, 177 (2013).

[17] W. H. Wang, Physics (Sin.) 40, 701 (2011).

[18] H. S. Chen, and D. Turnbull, Acta Metall. 17, 1021 (1969).

[19] H. S. Chen, and D. Turnbull, Acta Metall. 18, 261 (1970).

[20] J. J. Gilman, J. Appl. Phys. 44, 675 (1973).

[21] A. Inoue, T. Zhang, and T. Masumoto, Mater. Trans. JIM 31, 425 (1990)

[22] A. Inoue, Acta Mater. 48, 279 (2000).

[23] A. Peter, and W. L. Johnson, Appl. Phys. Lett. 63, 2342 (1993).

[24] W. L. Johnson, MRS Bull. 24, 42 (1999).

[25] N. Nishiyama, K. Takenaka, H. Miura, N. Saidoh, Y. Zeng, and A. Inoue, Intermetallics 30, 19 (2012).

[26] G. P. Johari, J. Non-crystal. Solids. 307, 317 (2002).

[27] H. B. Yu, W. H. Wang, K. Samwer, Mater. Today 16, 183 (2013).

[28] H. B. Yu, W. H. Wang, H. Y. Bai, and K. Samwer, *Natl. Sci. Rev.* 1, 429-461 (2014).

[29] J. M. Pelletier, B. Van de Moortele, I. R. Lu, Mater. Sci. Eng. A 336, 190 (2002)

[30] J. Hachenberg, and K. Samwer, J. Non-Cryst. Solids 352, 5110 (2006).

[31] Z. F. Zhao, P. Wen, W. H.Wang, and C. H. Shek, Appl. Phys. Lett. 89, 071920 (2006).

[32] P. Rosner, K. Samwer, P. Lunkenheimer, Euro. Phys. Lett. 68, 226 (2004).

[33] P. Wen, D. Q. Zhao, M. X. Pan, W. H. Wang, Y. P. Huang, and M. L. Guo, Appl. Phys. Lett. 84, 2790 (2004).

[34] H. B. Yu, K. Samwer, W. H. Wang and H. Y. Bai, Nature Commun. 4, 2204 (2013).

[35] H. S. Chen, Appl. Phys. Lett. 28, 245 (1976).

[36] Y. H. Liu, T. Fujita, D. P. B. Aji, M. Matsuura and M. W. Chen, Nature Commun. 5,

3328 (2014).

[37] K. L. Ngai, and S. Capaccioli, Phys. Rev. E 69, 031501 (2004).

[38] A. Kudlik, C. Tschirwitz, S. Benkhof, T. Blochowicz, and E. Rössler, Europhys. Lett. 40, 649 (1997).

[39] A. Kudlik, C. Tschirwitz, T. Blochowicz, S. Benkhof, and E. Rössler, J. Non-Cryst. Solids 235–237, 406 (1998).

[40] A. Kudlik, S. Benkhof, T. Blochowicz, C. Tschirwitz, and E. Rössler, J. Mol. Struct. 479, 210 (1999).

[41] W. H. Wang, J. Appl. Phys. 110, 053521 (2011).

[42] J. S. Harmon, M. D. Demetriou, W. L. Johnson, and K. Samwer, Phys. Rev. Lett. 99, 135502 (2007)

[43] H. B. Yu, X. Shen, Z. Wang, L. Gu, and W. H. Wang, Phys. Rev. Lett. 108, 015504 (2012).

[44] H. B. Yu, W. H. Wang, H. Y. Bai, Y. Wu and M. W. Chen, Phys. Rev. B 81, 220201 (2010).

[45] A. L. Greer, Science 267, 1947 (1995).

[46] W. L. Johnson, MRS bull. 24, 42 (1999).

[47] C. A. Schuh, T. C. Hufnagel, and U. Ramamurty, Acta Mater. 55, 4067 (2007).

[48] M. W. Chen, Annu. Rev. Mater. Res. 38, 445 (2008).

[49] Y. Q. Cheng, and E.Ma, Prog. Mater. Sci. 56, 379 (2011).

[50] W. H. Wang, Prog. Mater. Sci. 57, 487 (2012).

[51] F. Spaepen, Acta Metall. 25, 407 (1977).

[52] A. S. Argon, Acta Metall. 27, 47 (1979).

[53] W. L. Johnson, and K. Samwer, Phys. Rev. Lett. 95, 195501 (2005).

[54] M. W. Chen, A. Inoue, W. Zhang, and T. Sakurai, Phys. Rev. Lett. 96, 245502 (2006).

[55] A. L. Greer, Y. Q. Cheng, and E. Ma, Mater. Sci. Eng. R-Rep. 74, 71 (2013).

[56] J. S. Langer, Phys. Rev. E 70, 041502 (2004).

[57] D. Pan, A. Inoue, T. Sakurai, and M. W. Chen, Proc. Natl. Acad. Sci. U.S.A. 105, 14769 (2008).

[58] H. Wagner, D. Bedorf, S. Küchemann, M. Schwabe, B. Zhang, W. Arnold, and K. Samwer, Nature Mater. 10, 439 (2011).

[59] Y. H. Liu, D. Wang, K. Nakajima, W. Zhang, A. Hirata, T. Nishi, A. Inoue and M. W. Chen, Phys. Rev. Lett. 106, 125504 (2011).

[60] Y. Yang, J. F. Zeng, A. Volland, J. J. Blandin, S. Gravier, and C. T. Liu, Acta Mater. 60, 5260 (2012).

[61] H. Okuda, I. Murase, R. Kurosaki, E. Nakagawa, S. Oshiai, Y. Yokoyama, J. Saida, and K. Inoue, Intermetallics 14, 1038 (2006).

[62] T. Ichitsubo, E. Matusbara, T. Yamamoto, H. S. Chen, N. Nishiyama, J. Saida, and K. Anazawa, Phys. Rev. Lett. 95, 245501 (2005).

Chapter 2

Experimental Methods

2.1 Sample preparation

2.1.1 Arc melting

The as-cast ingots with homogeneous nominal compositions are prepared from high-purity elements (at least 3 N) by arc melting (NEV-AD03, Nissin Giken, **Fig. 2.1**) in a Ti-getter Ar atmosphere. The as-cast ingots are then utilized as master alloys.

2.1.2 Spin casting

The as-quenched ribbon samples are prepared using spin casting (RQM-T-20, Makabe Tech., **Fig. 2.2**). The revolutions per minute (RPM) of the water-cooled copper roller (20 cm in diameter) are controlled to be around 3000 to get enough cooling rates to produce metallic glass ribbons under Ar atmosphere of 0.05 cm Hg.

2.1.3 RF sputtering

The hyper-quenched metallic glass is prepared by deposition onto the silicon (100) substrates using radio frequency (RF) sputtering (ZDK-916-2 and SPE-220, Toei Electric, **Fig 2.3**) at room temperature [1]. The work power and Ar pressure are set to be 50 W and 0.3 Pa, respectively. The targets for the RF sputtering around 50 mm in diameter are machined from the as-cast ingots.

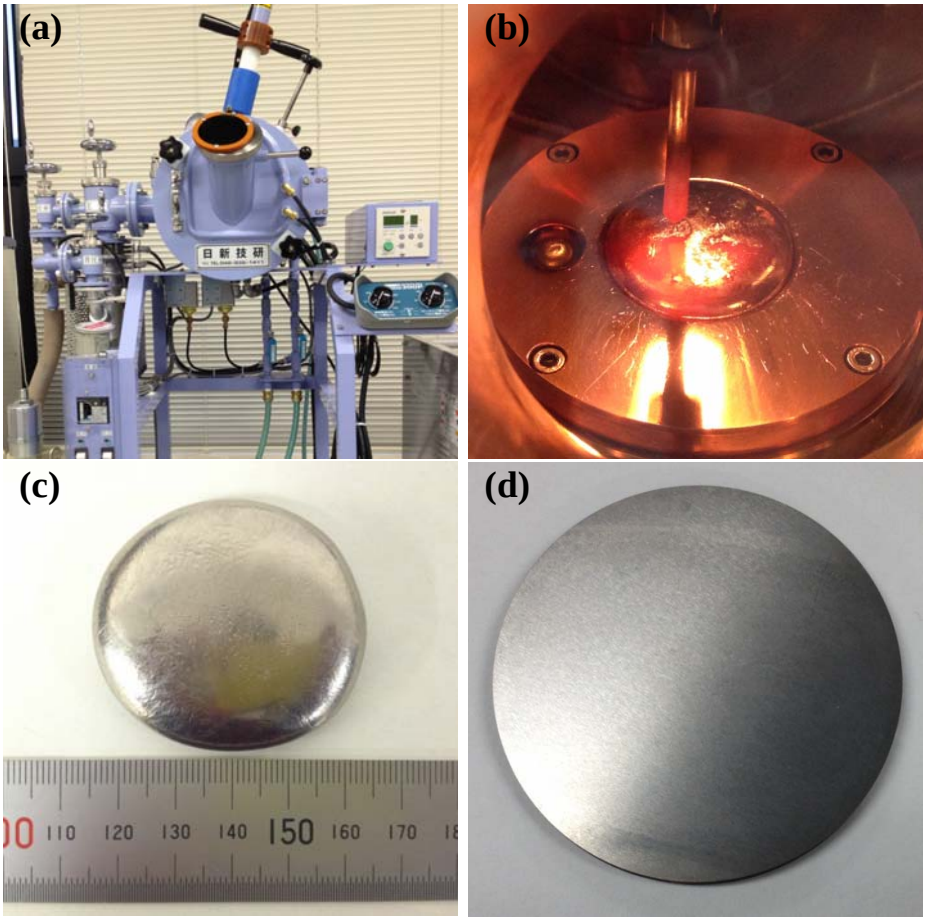

Fig. 2.1. Arc melting and as-cast ingots. (a) Arc melting machine. (b) A customized copper mold with a diameter of 50 mm inside the chamber of arc melting. (c) An as-prepared ingot. (d) An as-cast ingot sliced for the target of sputtering.

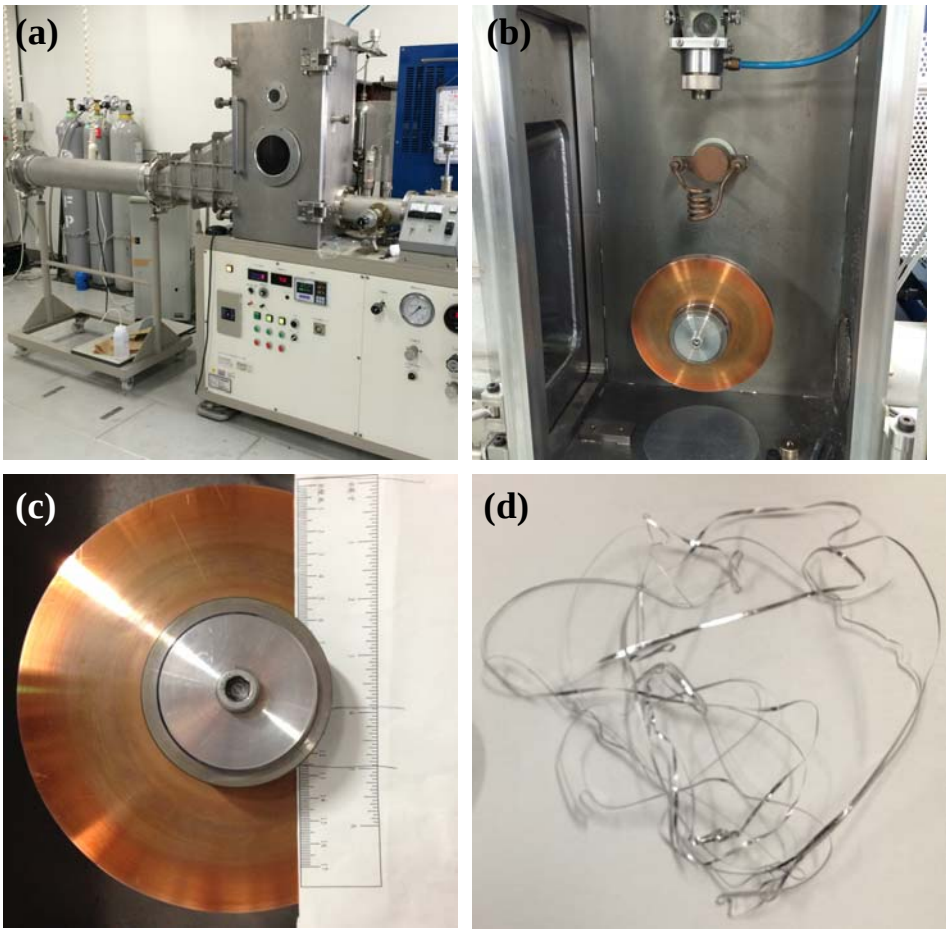

Fig. 2.1. Spin casting and as-quenched ribbons. (a) Spin casting machine. (b) Chamber of spin casting. (c) The copper roller inside the chamber. (d) As-spun ribbons prepared using the spin casting.

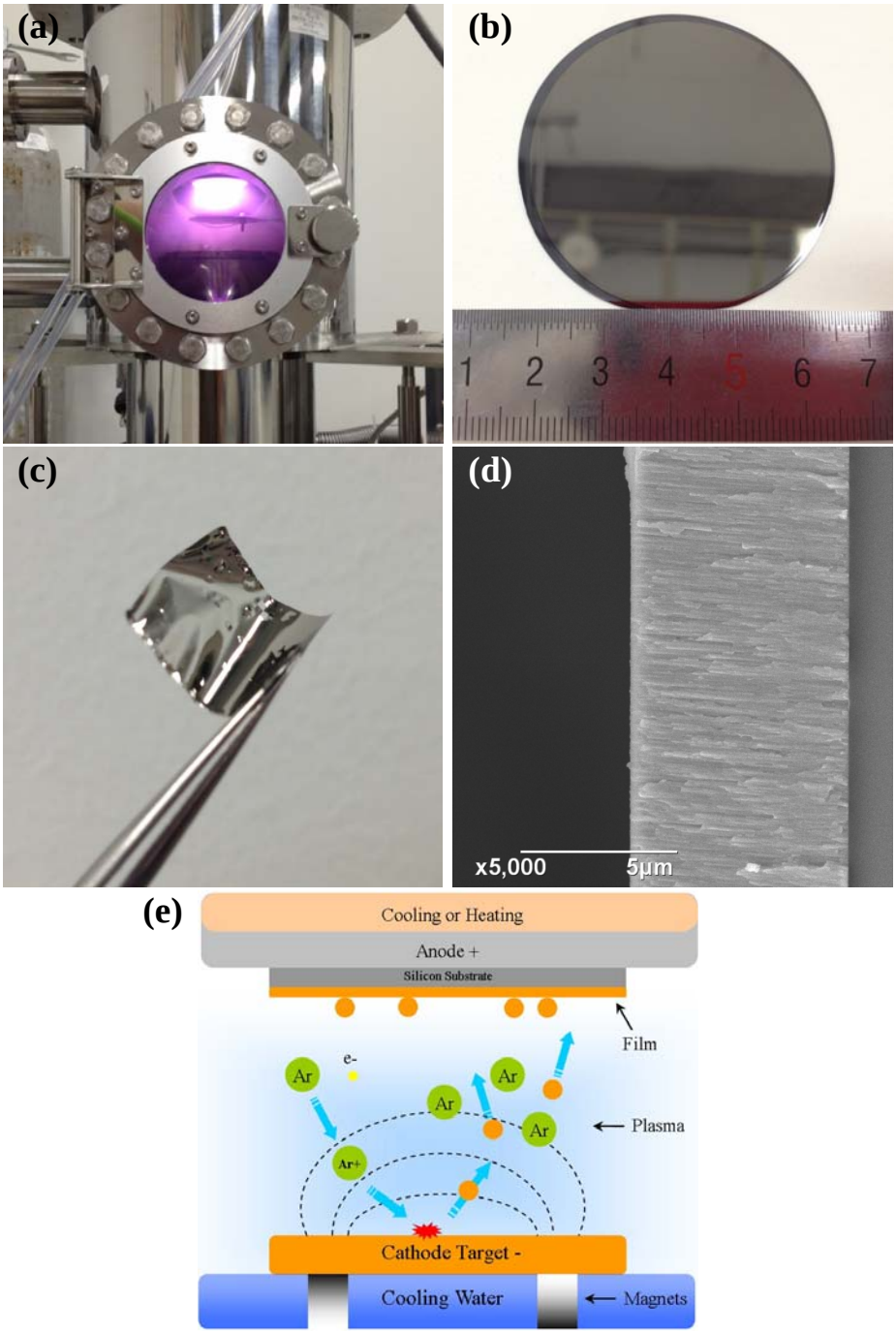

Fig. 2.3. RF sputtering and as-deposited film. (a) RF sputtering machine SPE-220. (b) As-deposited film on Si substrate. (c) The free-standing film by solving the Si in 30 vol. % KOH solution. (d) The cross section of the film. (e) A schematic illustration of RF sputtering. During the sputtering, the target materials are vaporized by the ionized Ar and condense on the Si substrate to form the film.

2.2 Structural characterizations

2.2.1 X-ray diffraction

The structures of the samples are characterized by X-ray diffraction (XRD, SmartLab, Rigaku, **Fig. 2.4**). Height adjustment is performed before the testing.

2.2.2 Multibeam scanning electron microscopy

The surface morphologies of the samples are measured using scanning electron microscopy (JIB 4600F, JEOL, **Fig. 2.5**). The equipped energy dispersive spectroscopy (EDS) is used to check the chemical compositions of the samples. The focused ion beam is applied to process the area of interest at micrometer scale with Gallium ion

2.2.3 Cs-corrected transmission electron microscopy

The TEM samples are prepared using ion-milling (Fischione Model 1050, **Fig. 2.6a**) and twin-jet electrochemical polishing (Struers TenuPol-5, **Fig. 2.6b**). The thick samples are thinned using the twin-jet polishing with electrolyte of 10 vol. % $HClO_4$ alcohol cooled by liquid nitrogen. The thin samples are thinned by the ion-milling with a low milling angle of 3^o and a voltage of 3 keV at -160^{o}C.

High-resolution TEM (HRTEM), scanning TEM (STEM) and Angstrom-beam electron diffraction (ABED) are taken by transmission electron microscopy (Cs-corrected TEM, JEM-2100F, JEOL, **Fig. 2.7**) operated at 200 kV. The TEM is equipped with two correctors to minimize the spherical aberrations of the probe-forming and image-forming lenses, respectively.

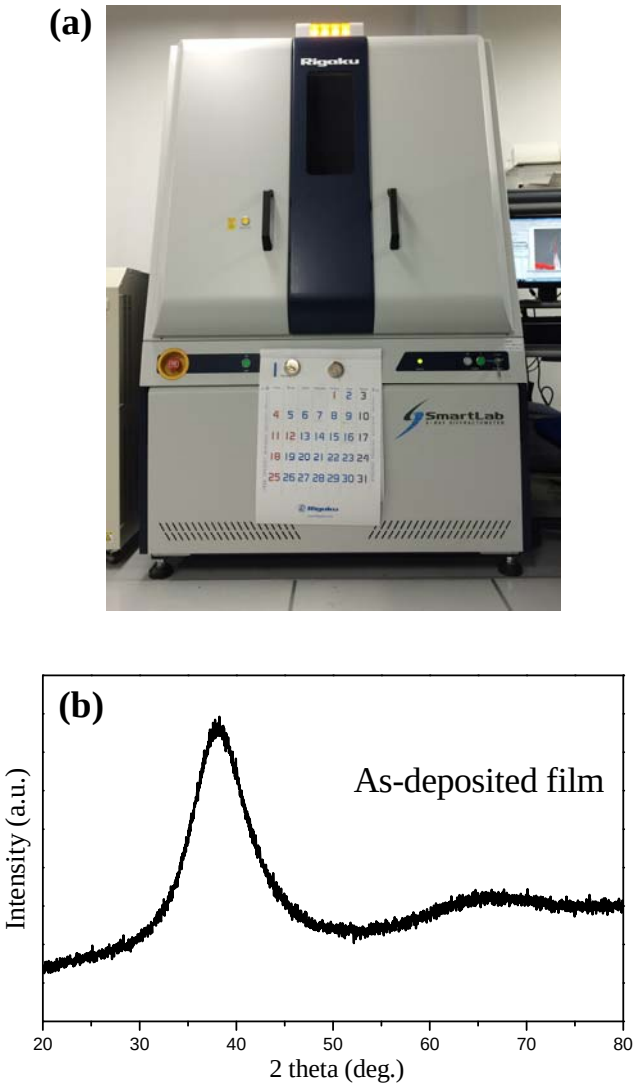

Fig. 2.4. X-ray diffraction. (a) Riguku SmartLab. (b) One XRD pattern for the as-deposited film.

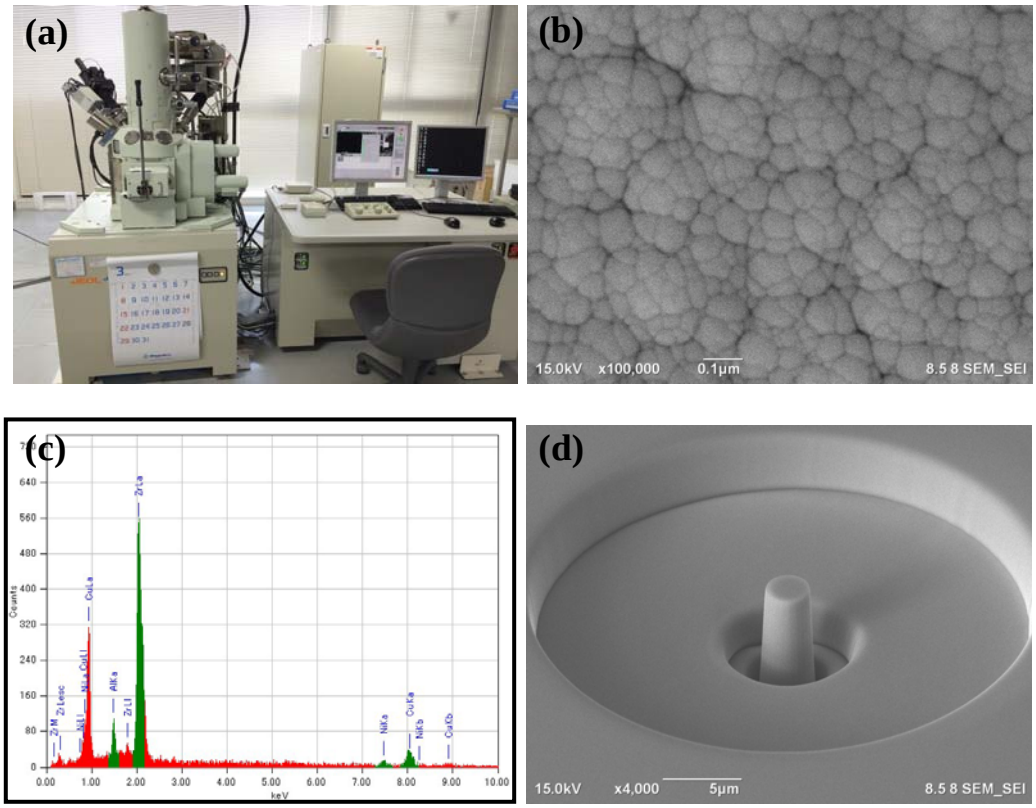

Fig. 2.5. Multibeam scanning electron microscopy. (a) JIB 4600F. (b) One SEM secondary electron images. (c) Energy dispersive spectroscopy. (d) Micropillar fabricated using focused ion beam.

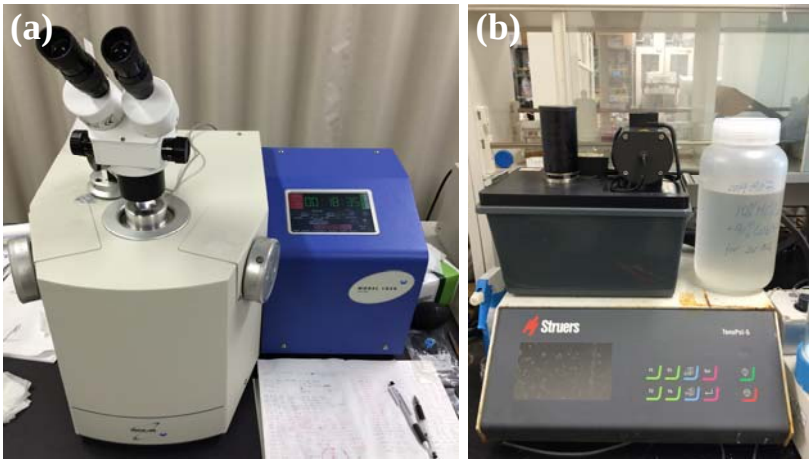

Fig. 2.6. TEM sample preparation. (a) Ion milling. (b) Twin-jet electrochemical polishing.

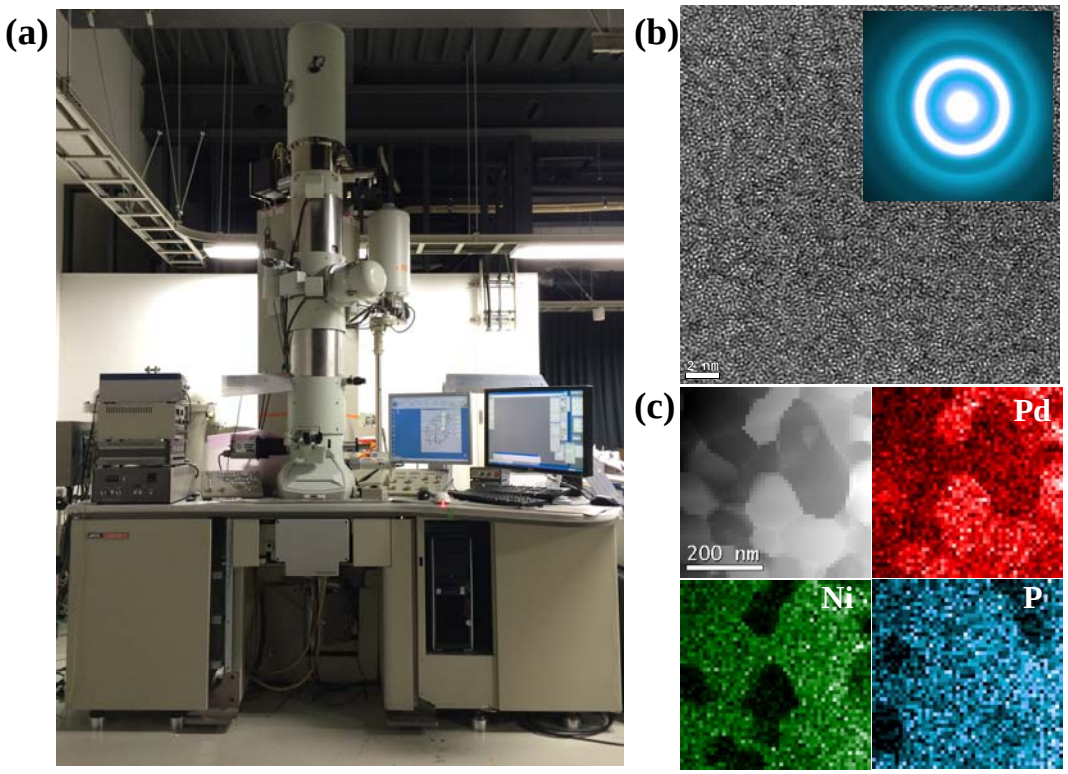

Fig. 2.7. Cs-corrected transmission electron microscopy. (a) JEM 2100F. (b) High resolution image and the diffraction patten. (c) STEM-EDS mapping for a Pd-Ni-P metallic material.

With the scanning electron probe controlled by Gatan Digiscan Ⅱ model 788, high-angle annular dark field (HAADF) STEM images are detected by an annular-type detector while the bright field (BF) STEM images are simultaneously recorded by a BF detector. The chemical distributions of the samples can be mapped using both energy dispersive spectroscopy (STEM-EDS) and electron energy loss spectroscopy (STEM-EELS) with different detectors.

2.3 Differential Scanning Calorimetry

The thermal properties of the samples are determined using differential scanning calotimeter (DSC 8500, Perkin-Elmer, **Fig. 2.8**) [3]. The baselines are recorded with empty pans before the measurement. The samples around 20 mg are enclosed in Al pans and subjected to up-scans at 20 K/min to get heat flow traces. The flowing Ar of high purity is used to protect the sample with a flow rate of 20 cm^3/min. The standard sample was prepared by slowly cooling the as-quenched sample from its supercooled liquid region at 20 K/min [4]. The DSC needs thermal stabilization at 300^oC for 180 min when neighboring heat flow curves show a large difference between them.

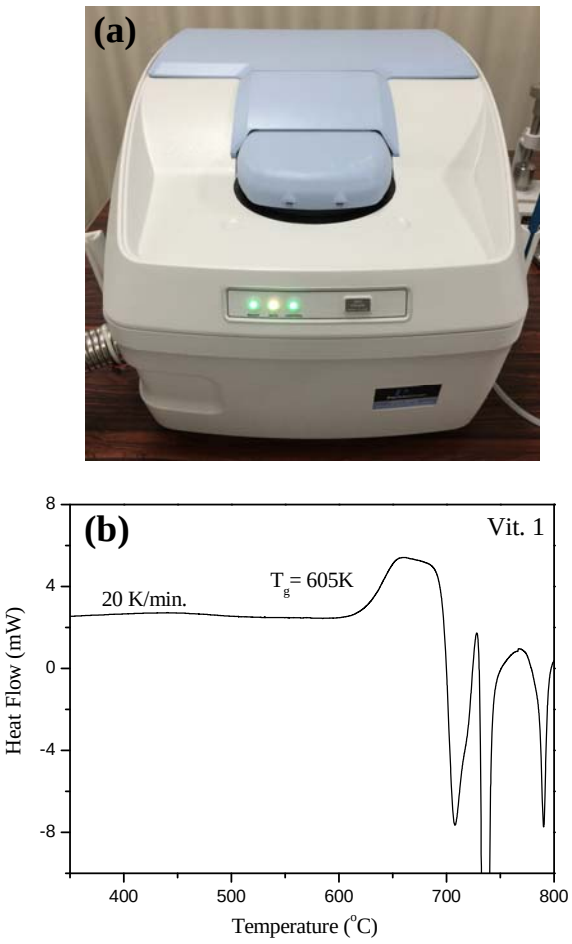

Fig. 2.8. Differential scanning calorimetry. (a) Perkin Elmer DSC 8500. (b) Heat flow traces for a metallic glass (Vitreloy 1) from which we can determine the glass transition temperature to be 605 K.

2.4 Amplitude-modulation dynamic atomic force microscopy

The AM-AFM measurement is performed by a scanning probe microscopy (Veeco CP-II, **Fig. 2.9**) set at tapping mode with a Nanoscope V controller [5]. A pyramidal silicon tip with a sharp diamond-like spike of ~1 nm is driven vibrating near the resonant frequency (~ 160 kHz) of Si cantilever to scan across the surfaces of samples. Surface height, phase shift and amplitude images are recorded simultaneously during the scanning. The amplitude ratio is set to be ~0.85 during the scanning. We found little dependence of the phase shift images on the amplitude ratio from ~0.6 to ~0.93.

2.5 Nanoindentation

The mechanical properties are measured by Nanoindenter (MTS G200, **Fig. 2.10**) equipped with a Berkovich indenter tip with a maximum loading of 50 mN at 0.1 mN/s [6-8]. At least 25 areas with spacing of 50 um are indented for each sample to get the mean value of hardness and modulus. The creep testing is set to automatically start when the thermal drift was less than 0.02 nm/s.

The accuracy and reliability of the instrumented nanoindentation depend on the bluntness of tip and its calibrations. During the indenter, the contact between sample and tip will wear down the tip. The tip will become blunt after many indenters and the tip area function should be calibrated. When the radius of a tip is larger than 200 nm, we should change a new one to get reliable results. After installing an indenter tip, the machine compliance changes and should be recalibrated. The nanoindenter is sensitive to the noise and the measurement at night and weekend will be better.

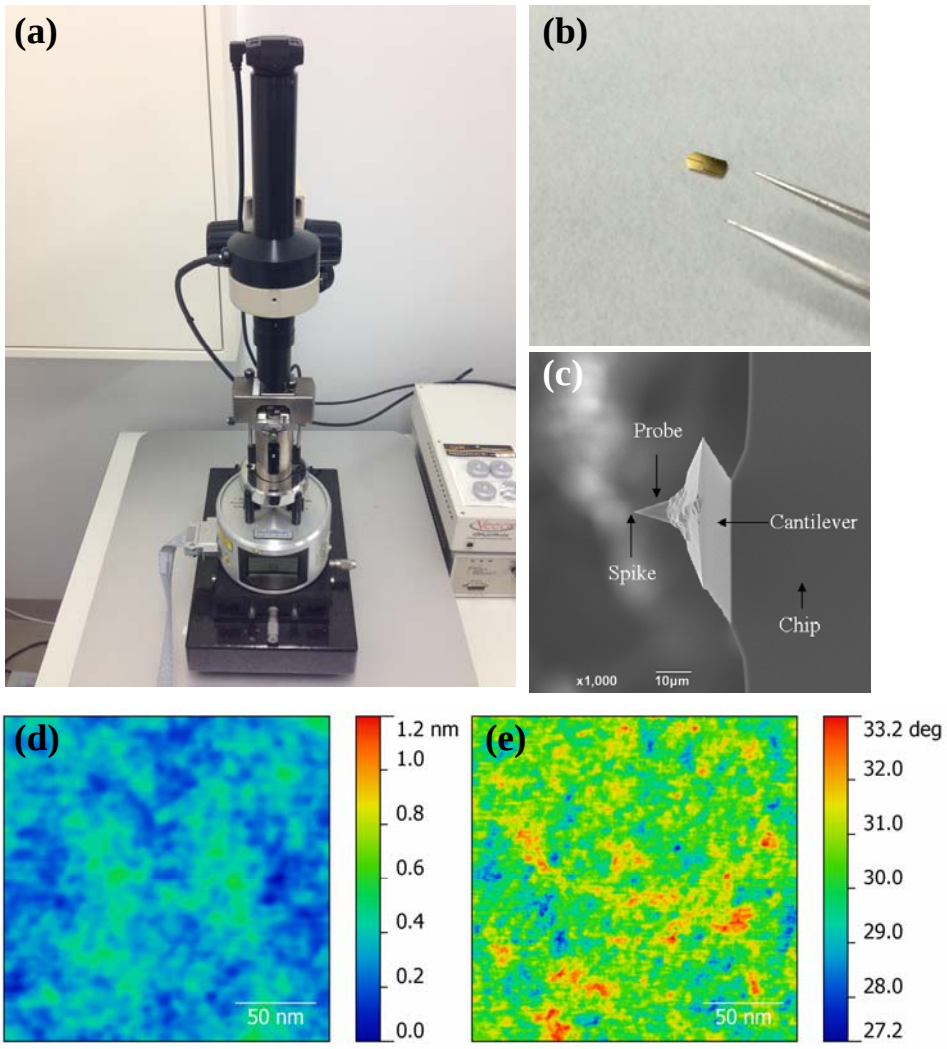

Fig. 2.9. Amplitude-modulation dynamic atomic force microscopy. (a) Veeco CP-II. (b) The outer shape of an AM-AFM tip. (c) The constitution of AM-AFM tip. (d) A height image and (e) a phase shift image recorded simultaneously.

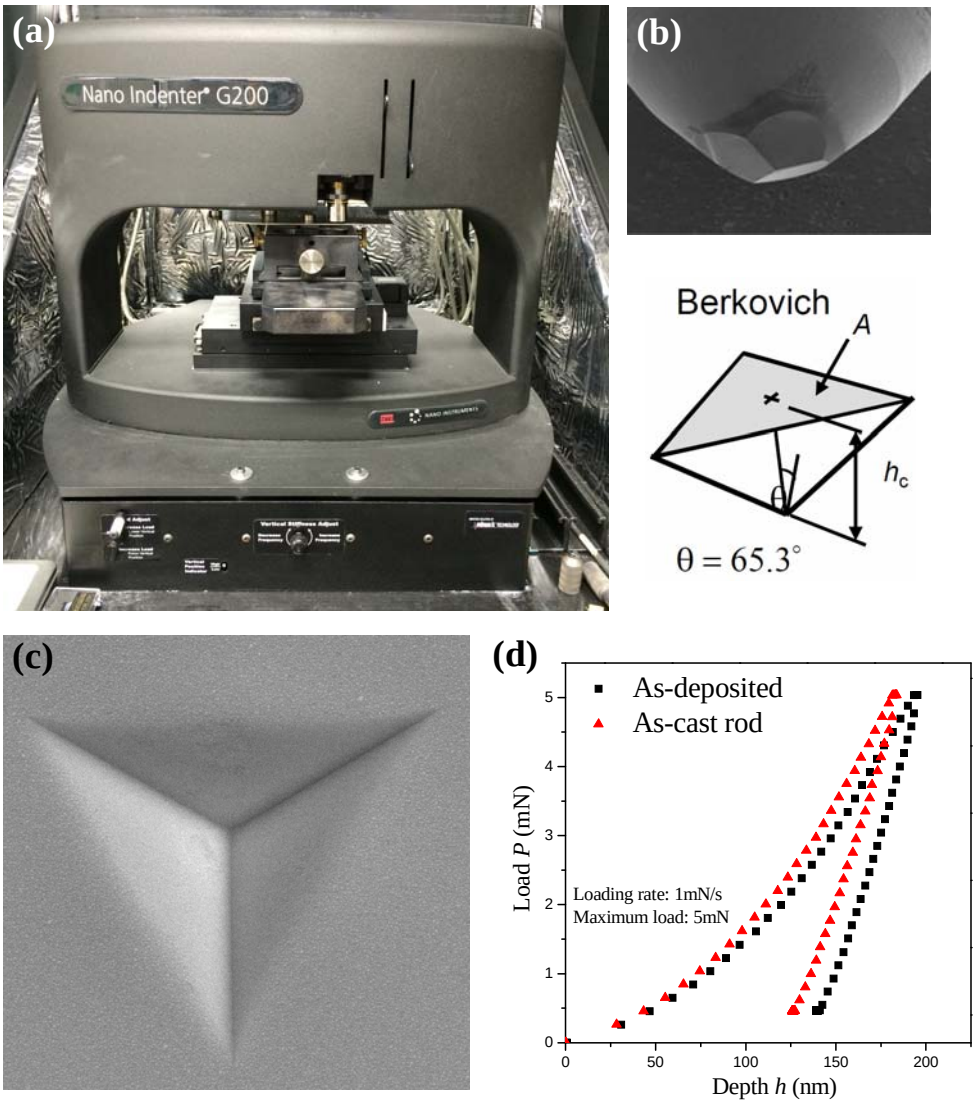

Fig. 2.10. Instrumented nanoindentation. (a) Nano Indenter G200. (b) Berkovich indenter tip and its geometry. (c) Impression in the sample's surface after indentation. (d) The force-depth curve from the indentation.

References

[1] Y. H. Liu, T. Fujita, A. Hirata, S. Li, H.W. Liu, W. Zhang, A. Inoue and M. W. Chen, Intermetallics 21, 105 (2012).

[2] A. Hirata, L. J. Kang, T. Fujita, B. Klumov, K. Matsue, A. R. Yavari and M. W. Chen, Science 341, 376 (2013).

[3] Y. H. Liu, T. Fujita, D. P. B. Aji, M. Matsuura and M. W. Chen, Nature Commun. 5, 3328 (2014).

[4] L. Hu, and Y. Z. Yue, J. Phys. Chem. C 113, 15001 (2009).

[5] Y. H. Liu, D. Wang, K. Nakajima, W. Zhang, A. Hirata, T. Nishi, A. Inoue and M. W. Chen, Phys. Rev. Lett. 106, 125504 (2011).

[6] D. Pan, A. Inoue, T. Sakurai, and M. W. Chen, Proc. Natl. Acad. Sci. U.S.A. 105, 14769 (2008).

[7] D. Pan, and M. W. Chen, J. Mater. Res. 24, 1466 (2009).

[8] Y. H. Liu, F. Zhao, Y. L. Li, and M. W. Chen, J. Appl. Phys. 112, 063504 (2012).

Chapter 3.

Sub-T_g Relaxation

3.1 Introduction

In 1976 H. S. Chen *et al.* reported the secondary enthalpy relaxation peak at low temperature prior to the primary relaxation at T_g in Pd-base metallic glasses using differential scanning calorimeter and found that the relative intensity of the secondary relaxation decreases with decreasing quenching rate [1]. Recently, L. N. Hu and Y. Z. Yue *et al.* proved that such secondary relaxation or sub-T_g relaxation observed in structure relaxation spectrum of $La_{55}Al_{25}Ni_{20}$ was β-relaxation as the activation energy of sub-T_g relaxation equaled to $26.8RT_g$ in accord with the empirical value for β-relaxations [2]. By a survey of the sub-T_g relaxation in other metallic glass systems, they declared that the simple correlation $E_\beta = 26.1RT_g$ is universal in metallic glasses.

Commonly, the metallic glasses are produced by quenching the glass-forming liquids with cooling rates ranging from ~1 K/s to ~10^6 K/s to prevent the competitive crystallization. Recently, an ultra-quenched metallic glass with a nominal cooling rate as high as ~10^9 has been reported [3]. The ultra-quenched metallic glass was produced by deposition of metallic atoms on cooled substrates using RF sputtering. The as-deposited metallic glass showed much broader excess enthalpy peak than the normally quenched metallic glasses and it is interesting to see if the sub-T_g relaxation of the as-deposited metallic glass is β-relaxation and obeys the correlation $E_\beta = 26.1RT_g$.

In this work the sub-T_g enthalpy relaxation of an as-deposited Zr-Cu-Al metallic glass was investigated using the hyperquenching-annealing-calorimetric scan (HAC) approach [2]. The nominal cooling rates of the as-deposited metallic glass was evaluated to be around 10^7 K/s, much larger than the bulk and ribbon metallic glasses and termed hyper-quenched metallic glass (**Fig. 3.1**). The hyper-quenched metallic glass samples were annealed at temperatures ranging from $0.68T_g$ to $0.9T_g$ and the remaining excess heat for each sample was measured. The derived activation energy of the enthalpy relaxation was $27.2RT_g$, confirming that the sub-T_g relaxation in the hyper-quenched metallic glass was β-relaxation.

3.2 Experimental

Hyper-quenched metallic glass. An as-cast ingot with a nominal composition of $Zr_{50}Cu_{40}Al_{10}$ (at. %) was prepared by arc melting, and then machined to a target for the sputtering. The hyper-quenched metallic glasses with a composition of $Zr_{53}Cu_{36}Al_{11}$ (at. %) were prepared by deposition of the vaporized target materials onto the silicon substrates using RF magnetron sputtering at 0.2 nm/s. The thickness of the sample was around 4 μm. Its nominal cooling rate was evaluated to be ~2.4×10^7 K/sec (**Fig. 3.1**).

Sub-T_g relaxation. The hyper-quenched metallic glasses were annealed in a Pt furnace for 5 min, 30 min, 180 min and 720 min at 473 K ($0.68T_g$), 503 K ($0.72T_g$), 523 K ($0.75T_g$), 553 K ($0.8T_g$), 573 K ($0.82T_g$) and 623 K ($0.9T_g$) under the flowing high-purity Ar as shown in **Fig. 3.2**. The sample marked with t_a = 0 min indicates the hyper-quenched metallic glass without annealing.

DSC measurement. The heat flow traces of the samples before and after sub-T_g relaxation were measured using differential scanning calotimeter (DSC, Perkin-Elmer 8500). The heating and cooling rates were 20 K/min. The standard sample was prepared by slowly cooling the hyper-quenched sample from its supercooled liquid.

3.3. Results and Discussion

3.3.1 Relaxed samples

In order to make sure that the annealing below T_g didn't induce phase separation or crystallization in the hyper-quenched metallic glasses, the structures of hyper-quenched metallic glasses before and after sub-T_g relaxation were checked. X-ray diffraction patterns for the hyper-quenched sample and the samples annealed at 553 K from 5 min to 720 min were shown in **Fig. 3.3**. The XRD patterns showed broad 1st diffraction peaks for all the samples, typical features of glassy materials. The sharp 2nd peak came from the Si substrate. No obvious peak shift can be observed in the XRD patterns. High resolution TEM images (**Fig. 3.4**) for the hyper-quenched and the sample annealed at 553 K for 720min indicated no crystalline feature or phase separation happening in the metallic glasses. The corresponding diffraction halos (Insets in **Figs. 3.4b, d**) also confirmed their amorphous nature. The SEM and EDS results (**Fig. 3.5**) showed that the long time annealing didn't introduce oxidation or contamination in the metallic glasses. The above structural characterizations confirmed that the annealing below T_g just leads to structural relaxation of the metallic glasses.

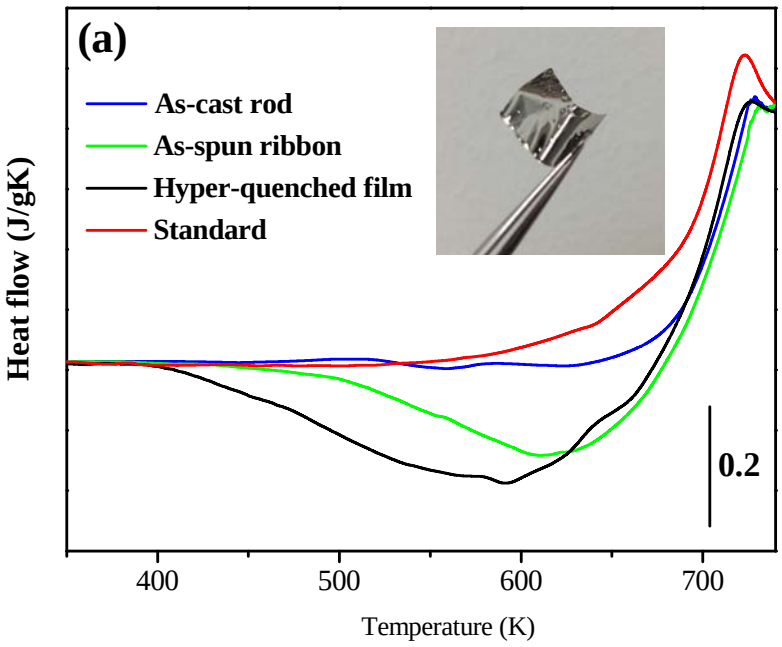

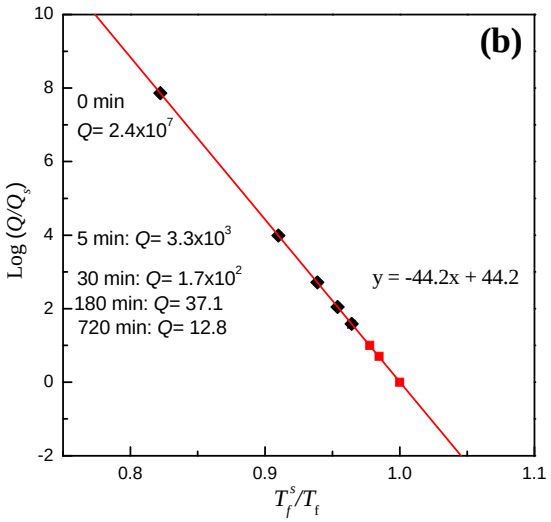

Fig. 3.1. Hyper-quenched metallic glass. (a) The heat flow traces of the as-cast rod, as-spun ribbon and hyper-quenched metallic glass with a similar composition around $Zr_{50}Cu_{40}Al_{10}$ (at. %). (b) The nominal cooling rate of the hyper-quenched metallic glass is evaluated to be ~2.4×10^7 K/sec according to the scaled Arrhenius plot of T_f versus cooling rates. Inset is the photo of the free-standing hyper-quenched metallic glass.

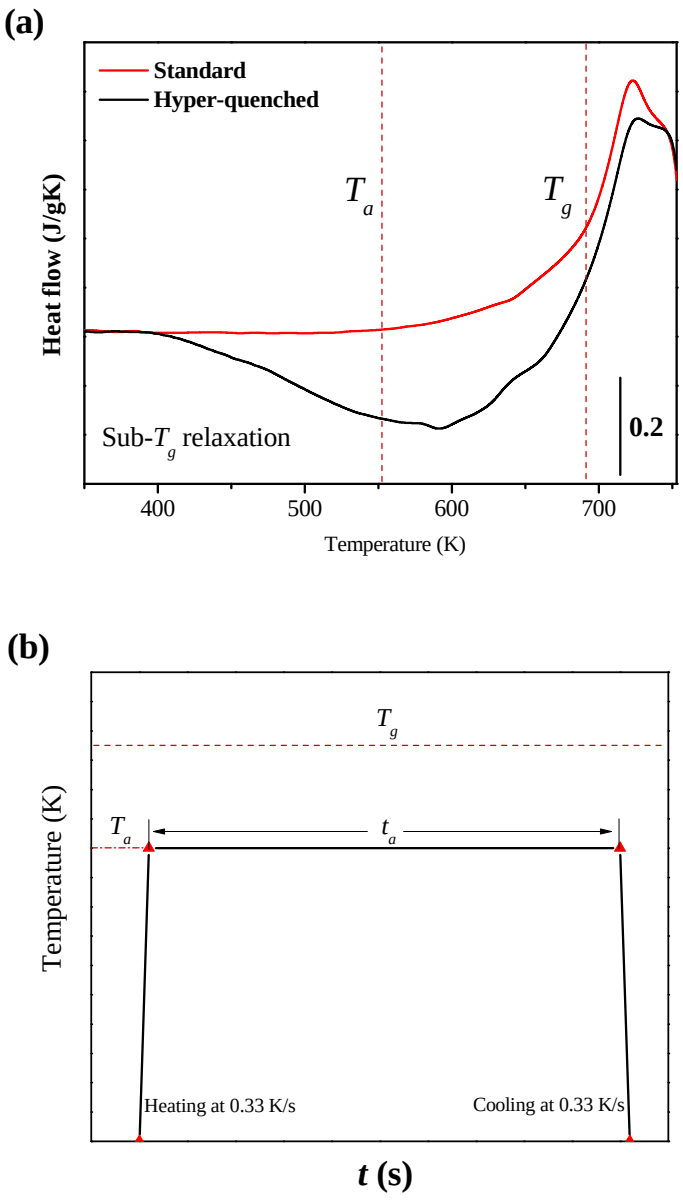

Fig. 3.2. Experimental procedure of the sub-T_g relaxation. (a) The annealing temperature T_a was selected below the glass transition temperature T_g. (b) The hyper-quenched metallic glass was annealed at T_a for certain time t_a.

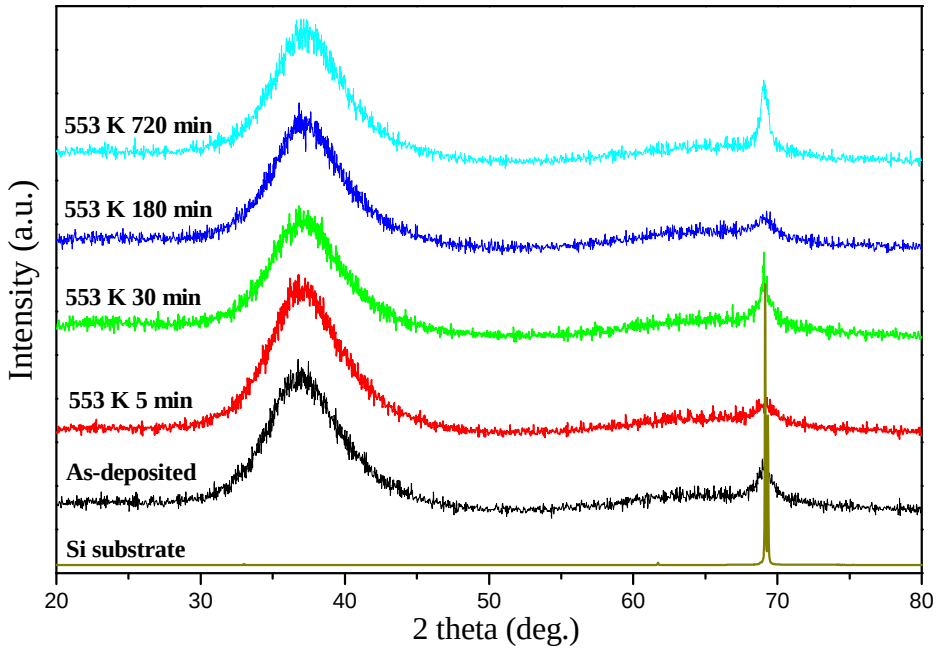

Fig. 3.3. XRD patterns for the samples annealed at 553 K for different durations. The sharp peaks overlapping with the second diffraction halos come from the Si substrate.

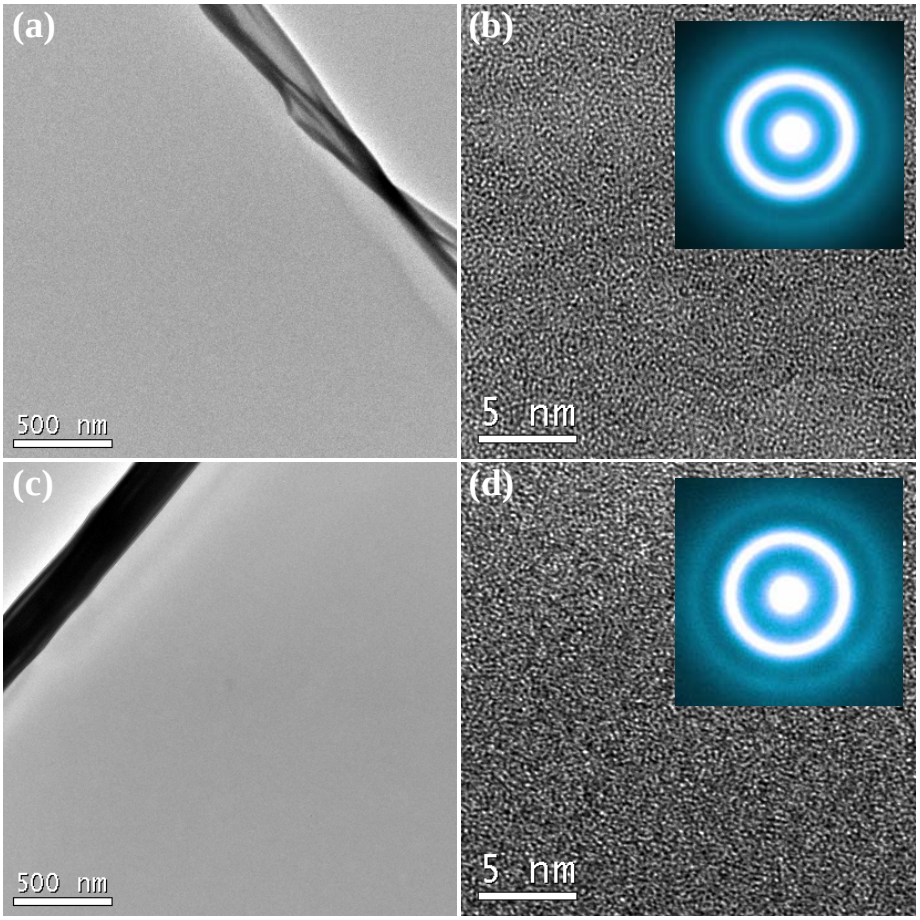

Fig. 3.4. Microstructure characterization using electron microscopy. **(a)** TEM and **(b)** HRTEM images of hyper-quenched metallic glass. **(c)** TEM and **(b)** HRTEM images of metallic glass relaxed at 553 K for 720 min showing typical amorphous structures in both samples. Insets are the corresponding diffraction halos for the samples.

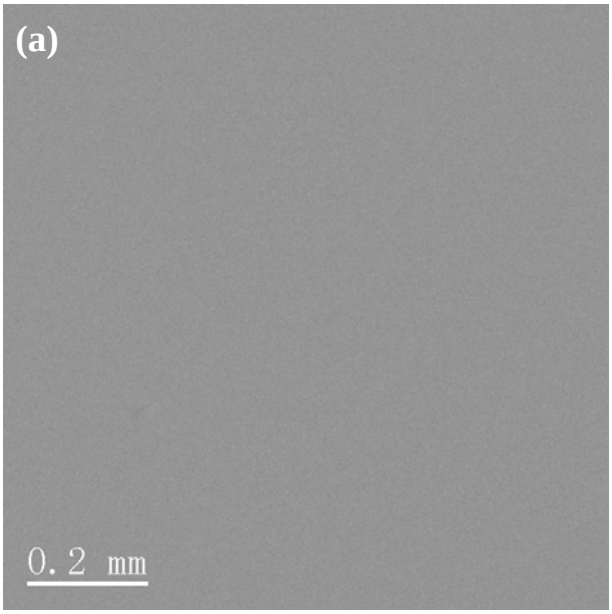

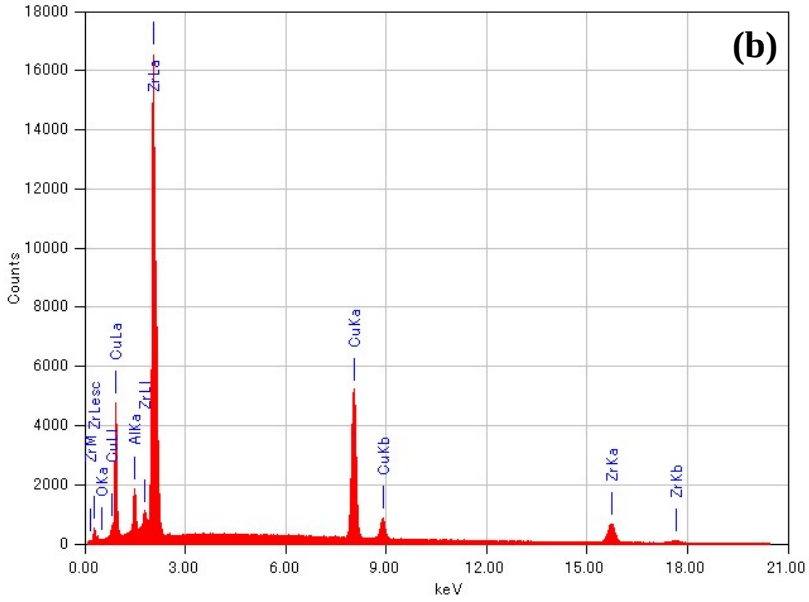

Fig. 3.5. Check of metallic glass samples after long-time annealing at 553 K for 720 min. **(a)** SEM image of the sample surface showing no contamination introduced by the annealing. **(b)** Energy dispersive X-ray spectrum of the samples indicating no oxidation occurred during the annealing.

3.3.2 Heat flow traces

Fig. 3.6 presented the heat flow traces of the hyper-quenched sample and samples after sub-T_g relaxation. Compared with the standard sample, the hyper-quenched sample exhibited a broad exothermic peak below T_g, indicating that abundant excessive enthalpy was trapped in it and its structure was far away from equilibrium [3]. At T_a = 473 K, the heat was sequentially released with t_a (**Fig. 3.6a**). For a constant t_a = 5 min, the heat release became faster at higher T_a (**Fig. 3.6b**). At T_a below 553 K the glass transition was little influenced by the sub-T_g relaxation as the DSC traces above T_g were almost overlapping before and after annealing (**Fig. 3.7)**. However, the sub-T_g relaxation at 573 K showed deviations of DSC profiles when the annealing time t_a was longer than 180 min, implying that only one relaxation process was involved with the sub-T_g relaxation below 553 K.

3.3.3 KWW fittings

The remaining excess enthalpy ΔH_{remain} can be calculated by integrating the difference in the apparent specific heat between the relaxed samples and the standard sample. The remaining excess enthalpies of the samples annealed below 553 K were normalized by the total excess enthalpy ΔH_{total} (ΔH_{remain} (t_a = 0)) and plotted against t_a as shown in **Fig. 3.8**. The plots were well fitted by the Kohlrausch-Williams-Watts (KWW) function $\Delta H_{remain} / \Delta H_{total} = \exp\left[-(t_a / \tau_\beta)^{\beta_{KWW}}\right]$, where τ_β was the characteristic relaxation time for the sub-T_g relaxation and β_{KWW} was the stretch parameter for the fitting. The fitting parameters for the fitting plots were summarized in **Tab. 3.1**.

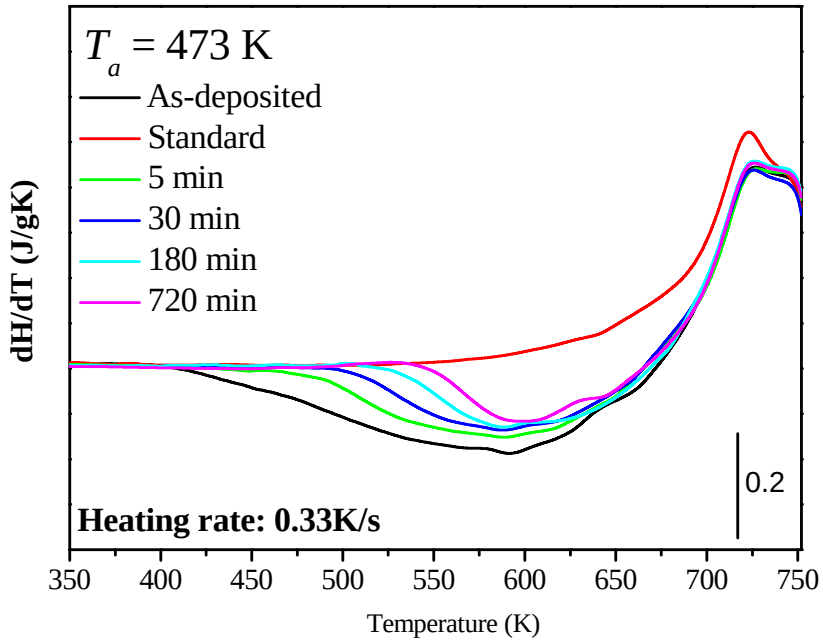

Fig. 3.6. Heat flow traces of hyper-quenched metallic glasses relaxed at T_a = 553 K for different durations.

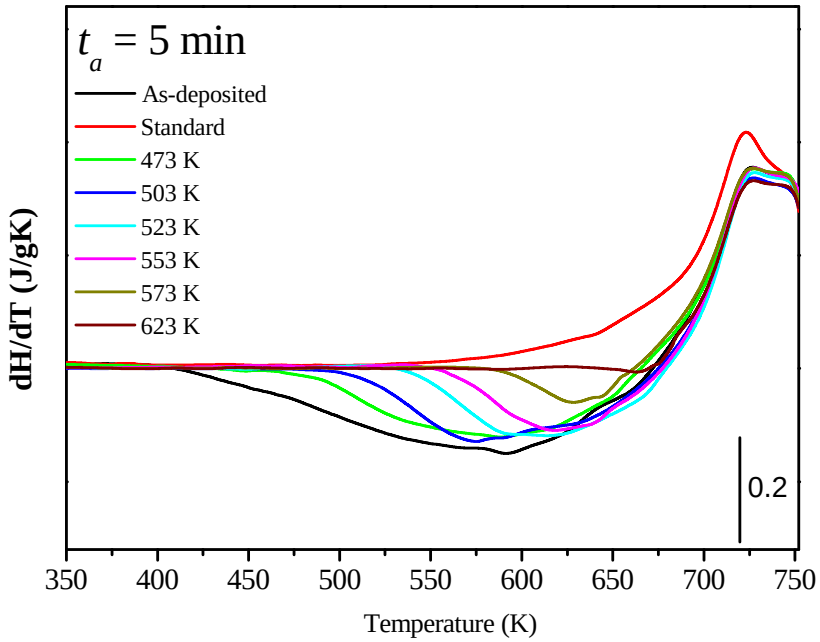

Fig. 3.7. Heat flow traces of hyper-quenched metallic glasses annealed at different temperatures T_a for t_a = 5 min.

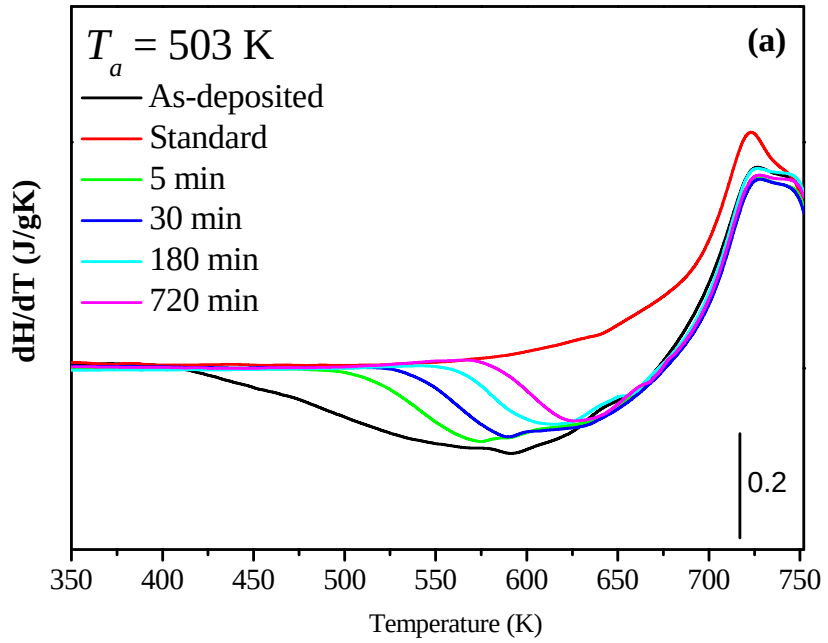
T_a = 503 K
(a)
As-deposited
Standard
5 min
30 min
180 min
720 min
dH/dT (J/gK)
0.2
350
400
450
500
550
600
650
700
750
Temperature (K)

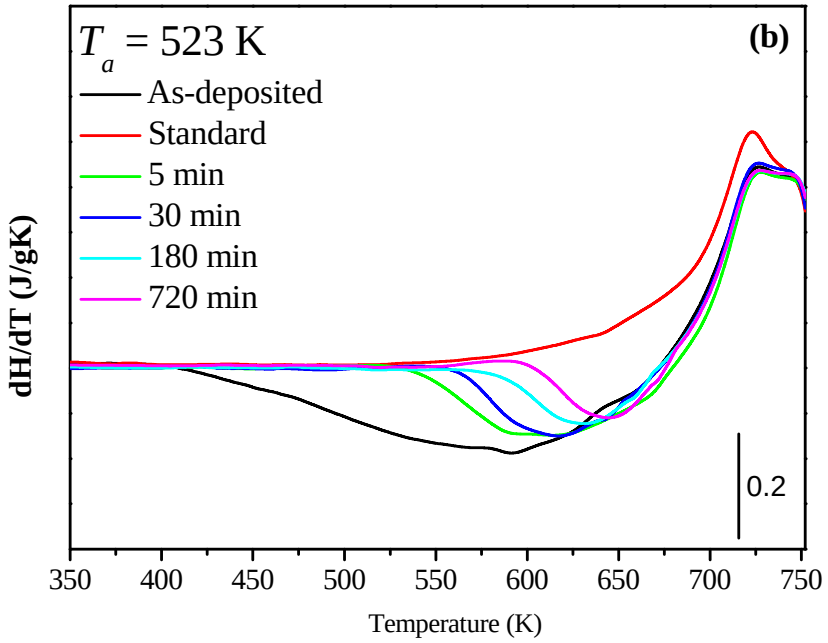
T_a = 523 K
(b)
As-deposited
Standard
5 min
30 min
180 min
720 min
dH/dT (J/gK)
0.2
350
400
450
500
550
600
650
700
750
Temperature (K)

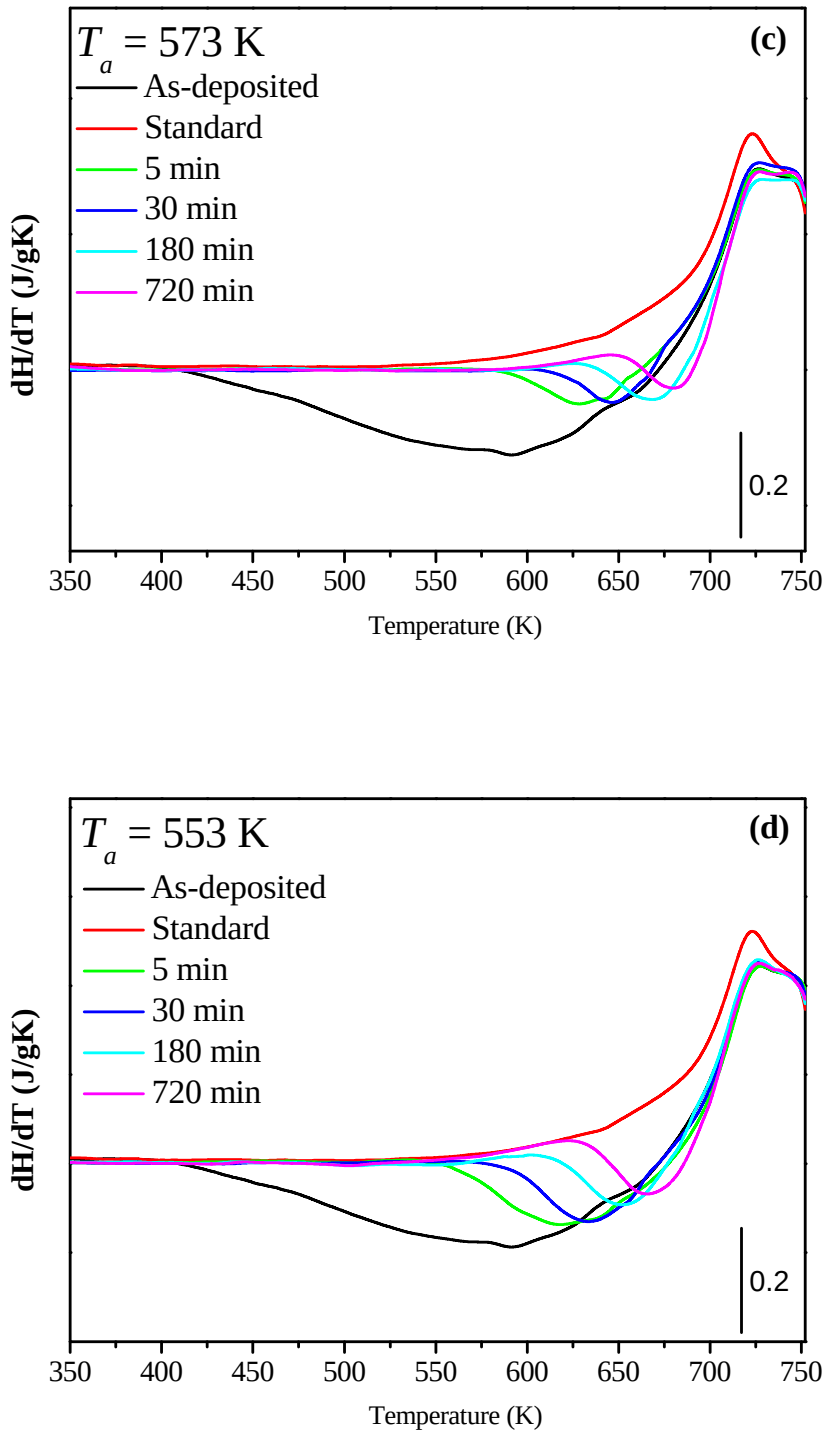

Fig. 3.7. Heat flow traces of sub-T_g structural relaxation at **(a)** T_a = 503 K (0.68T_g); **(b)** 523 K (0.72T_g); **(c)** 553 K (0.75T_g) and **(d)** 573 K (0.82T_g) for 5 min, 30 min, 180 min and 720 min.

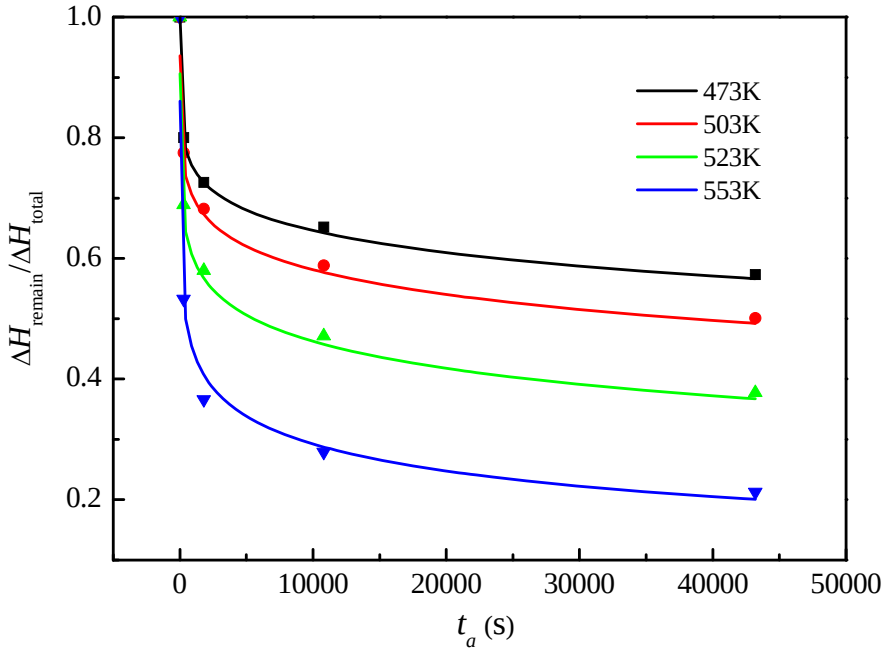

Fig. 3.8. Annealing time t_a dependence of the normalized remaining enthalpy after relaxation for the samples annealed at 473 K, 503 K, 523 K and 553 K and their corresponding fittings by KWW function.

TABLE 3.1. Characteristic relaxation time τ_β and stretch parameters β_{KWW} for the KWW fittings in **Fig. 3.6**. At higher T_a the characteristic relaxation time was shorter, which means the process became more active. The stretch parameter increased a little with the annealing temperature which is in accord with previous report.

T_a	**ln** τ_β	β_{KWW}
473 K	13.8	0.180
503 K	12.6	0.182
523 K	10.7	0.183
553 K	8.1	0.185

3.3.4 Activation energy

At temperature below T_g the β-relaxations obey the Arrhenius equation $\tau_\beta = \tau_{0,\beta} \exp(E_\beta / RT)$ [4]. The activation energy E_β for the sub-T_g relaxation can be calculated by plotting the relaxation time τ_β versus the reciprocal annealing temperature ($1/T_a$). The linear relationship in **Fig. 3.9** gave a value of E_β around 157 kJ/mol or $27.2RT_g$, which is in accord with the empirical value ($26.1RT_g$) for β-relaxation as found in the metallic glasses, polymers and rigid molecules etc. [2, 5-8]. The activation energy of sub-T_g relaxation was much smaller than $54.4RT_g$ for the glass transition and $52RT_g$ for the crystallization (**Fig. 3.10**).

If we extrapolated the plot in **Fig. 3.9** to the glass transition temperature T_g = 695 K, the characteristic relaxation time was evaluated to be 56.2 s (**Fig. 3.11**). This value is close to the characteristic relaxation time of α-relaxations around T_g from 40 to 100 s [9]. It is known that at a temperature T_c (about 1.2 T_g), the β-relaxations will merge with the α-relaxations [4]. This is another feature of β-relaxations which confirmed the sub-T_g relaxation in the hyper-quenched metallic glass as β-relaxation again.

Although the β-relaxation is commonly considered as reversible processes and the sub-T_g relaxation is irreversible, both thermal measurements [2, 3] and dynamic mechanical analysis [10] have evidenced that the sub-T_g relaxation of rapidly-quenched metallic glasses is mainly processed by the β-relaxation. It is concluded that in the hyper-quenched metallic glass the β-relaxation dominated the enthalpy release and thus the structural changes during the sub-T_g relaxation. Thus the sub-T_g relaxation can be used as a tool to tune the intensities of β-relaxations in metallic glasses.

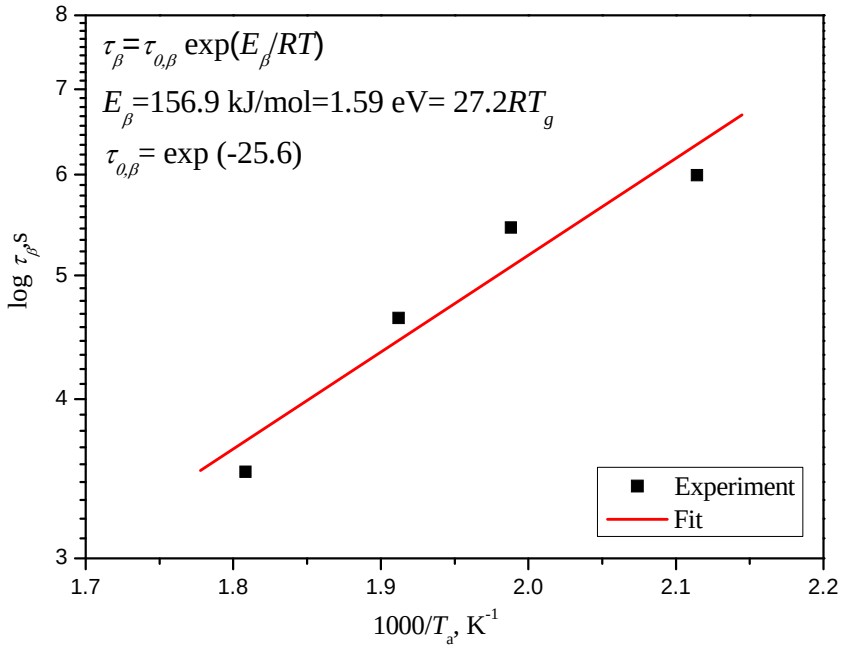

Fig. 3.9. Dependence of the characteristic relaxation time τ_β on the reciprocal annealing temperature ($1/T_a$) surrendering the activation energy of sub-T_g relaxation according to the Arrehnius equation.

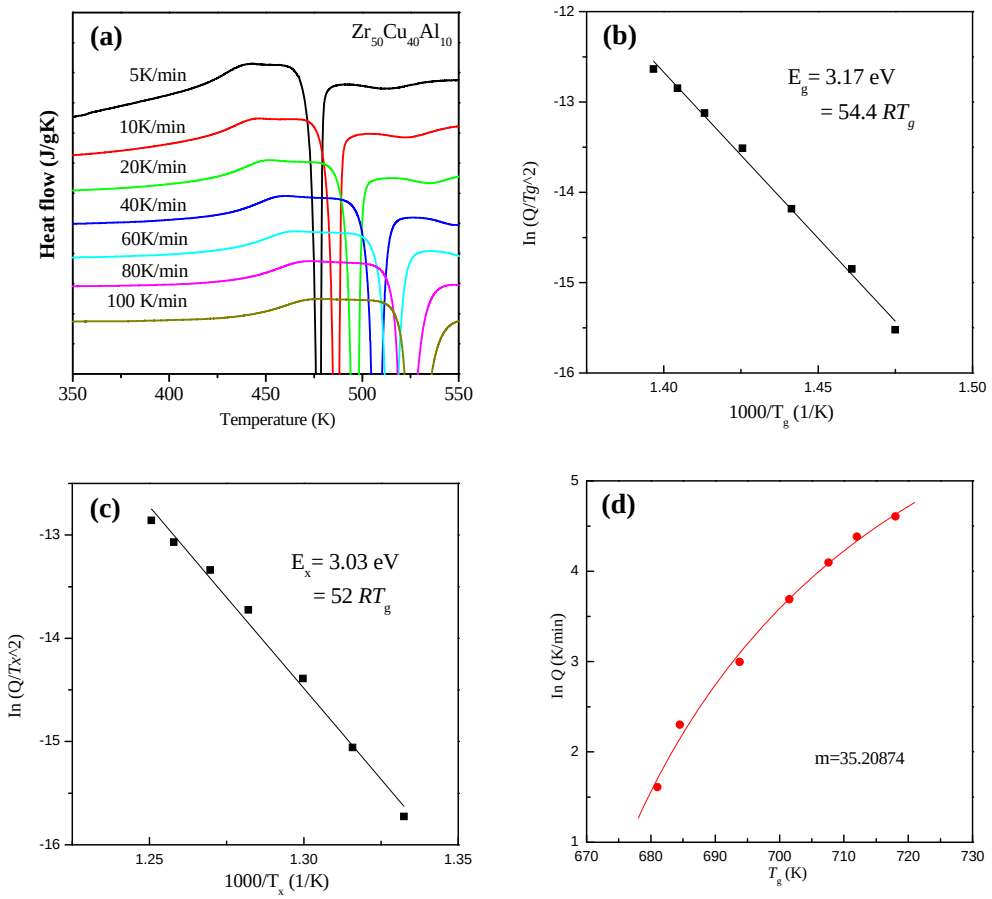

Fig. 3.10. (a) Heat flow traces of the hyper-quenched metallic glasses at different heating rates. Kissinger plots of (b) the glass transition temperatures and (d) crystallization temperatures versus hearing rate. The slope of the plot equals to the activation energy for each process. (d) Dependence of glass transition temperature on heating rate. The solid line is the Vogel-Fulcher-Tamman (VFT) equation fitting where the fragility can be derived.

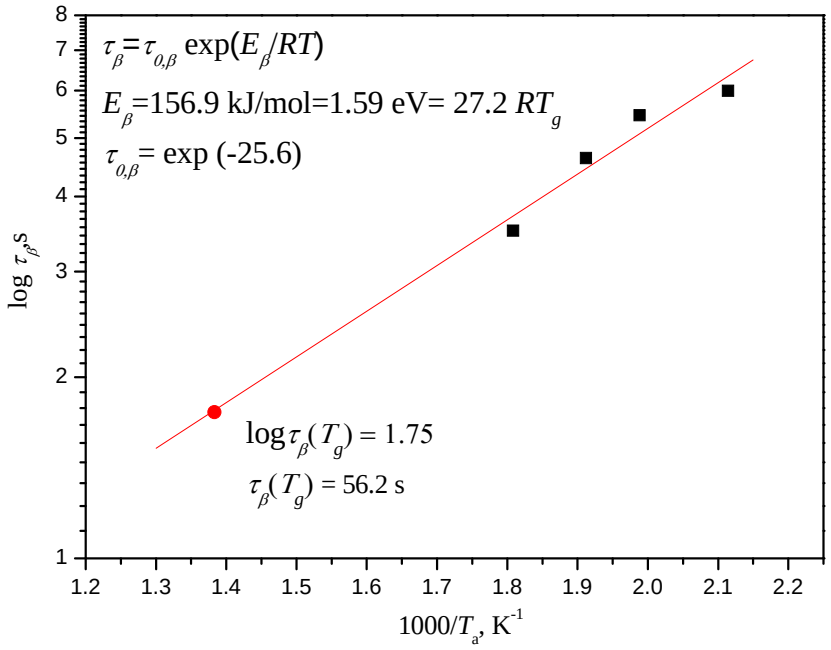

Fig. 3.11. The extrapolation of Arrhenius plot to glass transition temperature. The characteristic relaxation time of sub-T_g relaxation around T_g was evaluated to be 56.2 s according to this extrapolation.

3. 4 Summary

We systematically studied the sub-T_g relaxation of hyper-quenched metallic glasses. The normalized remaining enthalpy of the samples during sub-T_g relaxation can be well expressed by the KWW function. The characteristic relaxation times derived from the KWW fittings became shorter at higher T_a. According to the Arrhenius equation the activation energy of the sub-T_g relaxation was calculated to be $27.2RT_g$, which is close to the empirical value for β-relaxation. The extrapolation of the characteristic relaxation time with T_a to T_g gave a value close to that of α-relaxation, showing another feature of β-relaxations. In general, the sub-T_g relaxation in the hyper-quenched metallic glass is determined to be an identical process of β-relaxation.

References

[1] H. S. Chen, Appl. Phys. Lett. 28, 245 (1976).

[2] L. Hu, and Y. Z. Yue, J. Phys. Chem. C 113, 15001 (2009).

[3] Y. H. Liu, T. Fujita, D. P. B. Aji, M. Matsuura and M. W. Chen, Nature Commun. 5, 3328 (2014).

[4] P. G. Debenedetti, and F. H. Stillinger, Nature 410, 259 (2001).

[5] K. L. Ngai, and S. Capaccioli, Phys. Rev. E 69, 031501 (2004).

[6] A. Kudlik, C. Tschirwitz, S. Benkhof, T. Blochowicz, and E. Rössler, Europhys. Lett. 40, 649 (1997).

[7] A. Kudlik, C. Tschirwitz, T. Blochowicz, S. Benkhof, and E. Rössler, J. Non-Cryst. Solids 235–237, 406 (1998).

[8] A. Kudlik, S. Benkhof, T. Blochowicz, C. Tschirwitz, and E. Rössler, J. Mol. Struct. 479, 210 (1999).

[9] L. Hu, and Y. Z. Yue, J Phys. Chem. B 112, 9053 (2008).

[10] J. Hachenberg, D. Bedorf, K. Samwer, R. Richert, A. Kahl, M. D. Demetriou, and W. L. Johnson, Appl. Phys. Lett. 92, 131911 (2008).

Chapter 4

Spatial Heterogeneity Evolution

4.1 Introduction

When cooled to the moderately supercooled regime, the single relaxation process in the glass-forming liquids splits into α and β-relaxations, of which α-processes are related to the glass transition and vanish at T_g [1-5]. The β-relaxation or Johari-Goldstein (JG) relaxation is commonly believed to be a precursor of α-relaxation and plays as the principal source of dynamics in glasses below T_g [6]. Recent studies show that the β-relaxation also plays important roles in physical aging [7], accelerated partial devitrification [8] and the deformation of metallic glasses [9, 10], indicating both scientific and practical significances of β-relaxation. However, the micro-mechanism for the origin of β-relaxation is not fully understood and the proposed modes still remain evolving [2-6, 11-16].

G. P. Johari [11] has pointed out that the β-relaxation in mechanically rigid glasses, especially in metallic glasses, should be processed by the translational motion of atoms localized in loosely packed regions. This scheme certainly assumes the existence of spatially heterogeneous structures in glasses which still needs more experimental supports [17]. The latest synchrotron X-ray investigations demonstrated that the process of β-relaxation in metallic glass was involved with short-range collective rearrangement of large solvent atoms by local cooperative bonding switch,

implying the local motions of atoms associated with spatial heterogeneity [16]. More recently, the stress relaxation spectra were used to evaluate the spatial heterogeneity in metallic glass based on the distribution coefficients and correlated the relaxation modes with the structural evolution [18]. However, the direct characterization of spatial heterogeneity correlated with β-relaxation in metallic glass is still missing.

The atomic force microscopy (AFM) has been performed to investigate the spatial heterogeneity in metallic glasses [19-22]. The spatial heterogeneity with a correlation length of ~2.5 nm was reported in a Zr-base metallic glass using the amplitude-modulation dynamic atomic force microscopy (AM-AFM) [19]. By measuring the normalized energy dissipation curve, the observed spatial heterogeneity was determined to mainly originate from the viscoelastic behavior of metallic glass. The AM-AFM provides a well-defined characterization tool on the spatial heterogeneities in amorphous materials.

In this study, we performed the AM-AFM on hyper-quenched metallic glasses with controlled changing structures by the sub-T_g relaxation. The correlation lengths of spatial heterogeneity sequentially decreased from ~6 nm to ~2.5 nm with the annealing time, behaving as a non-exponential relaxation process well expressed by the Kohlrausch-Williams-Watts (KWW) function. The evolution of spatial heterogeneity gave characteristic relaxation time and activation energy close to those of β-relaxation measured by hyperquenching-annealing-calorimetric scan (HAC) approach. The above result provides direct evidence on the correlation between β-relation and spatial heterogeneity in metallic glasses.

4.2 Experimental

Sample preparation. The hyper-quenched metallic glass with a composition of $Zr_{53}Cu_{36}Al_{11}$ (at. %) was prepared by RF magnetron sputtering at room temperature.

Sub-T_g relaxation. In order to get metallic glasses with successively changing structures, the hyper-quenched samples were relaxed below its glass transition temperature (T_g = 695 K). The sub-T_g relaxation can probe the β-relaxation with a higher frequency from the relaxation involved in the α frequency range, and make sure the structural changes characterized by our testing is correlated with the β-relaxation [7]. The samples were annealed at T_a = 473 K ($0.68T_g$), 523 K ($0.75T_g$) and 553 K ($0.8T_g$) for different durations from t_a = 5 min to 720 min. The sample marked with t_a = 0 min indicates the hyper-quenched metallic glass without annealing.

Amplitude-modulation dynamic AFM. The hyper-quenched and relaxed metallic glasses were directly used for the AM-AFM testing without any polishing to avoid possible scratch or contamination to the sub-nano-scale smooth surfaces. The scanning probe microscopy was set at tapping mode equipped with a pyramidal silicon tip of ~1 nm **(Fig. 4.1**) [19]. The amplitude ratio was set to be around 0.85 during the scanning. At least three different locations were scanned for each sample to get the mean value.

During the scanning, the tip is driven by the head with sine-like signal. The interaction between the tip and sample will damp the amplitude of vibrating tip. By adjusting the height of tip to recover the amplitude, the height images can be recorded related to the topography and composition of samples. Meanwhile, the interaction will cause the phase-lag of the vibrating tip relative to the input signal due to the dissipation

energy from which we can get the phase shift images. The phase shift image is only related to the phase and composition of the samples.

Commonly, there are three mechanisms accounting for the energy dissipation during the scanning: surface attraction, energy hysterisis and viscoelasticity [19]. Surface attraction comes from the attraction due to the atomic force. Energy hysterisis can be induced by the permanent plastic deformation of the materials. And the viscoelasticity is related to the viscoelastic deformation of materials under the tip. It is meaningful to determine which mechanism accounts for the phase shift observed in metallic glasses. In **Fig. 4.2**, the contact pressure during the scanning can be evaluated. We can see that even the contact radius is as small as the average atomic radius; the contact pressure is still around 0.5 GPa which is much lower than the yielding stress for Zr-base metallic glass. Thus the plastic deformation can be excluded. The ramp mode was performed by approaching the tip to the surface of metallic glass (**Fig. 4.3**). We can see a peak in the middle range of A/A_0 in **Fig. 4.3c** and an inflection at the end of the A/A_0 range in **Fig. 4.4d**, both of them are the features of viscoelastic behavior, demonstrating that the phase shift observed in metallic glasses comes from the viscoelastic deformation [19, 20].

Height-height correlation function. The correlation function $P(r) = 2\sigma^2 [1-\exp(-(r/\xi)^{2\alpha})]$ was applied to quantitatively evaluate the size of spatial heterogeneity (**Fig. 4.4**), where the σ is the standard deviation of phase shift values, α is the exponent and ξ is the lateral correlation length [20]. ξ defines the characteristic lengths between two correlated points in the images.

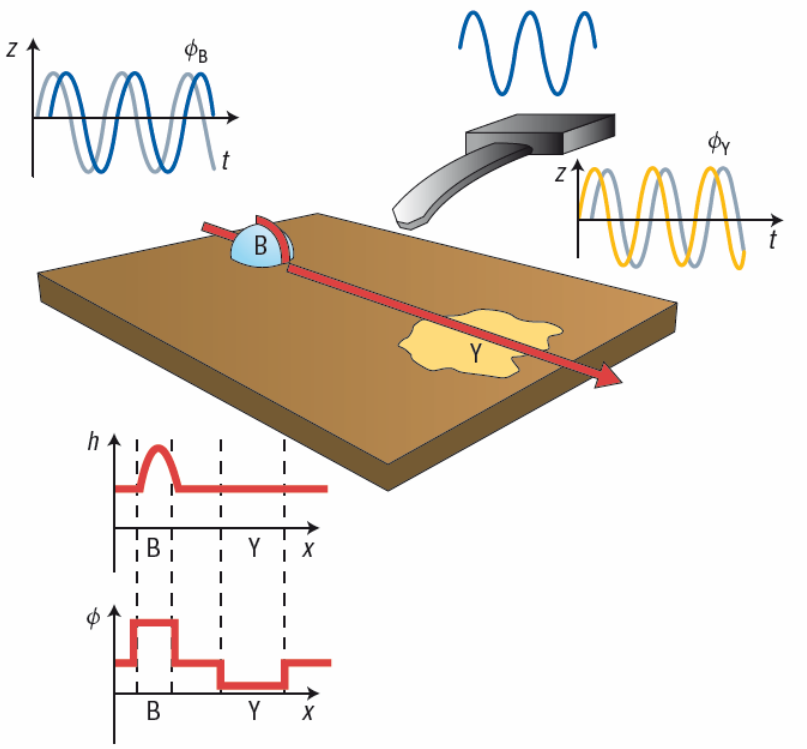

Fig. 4.1. The schematic illustration of AM-AFM. (Adapted from ref. 19.)

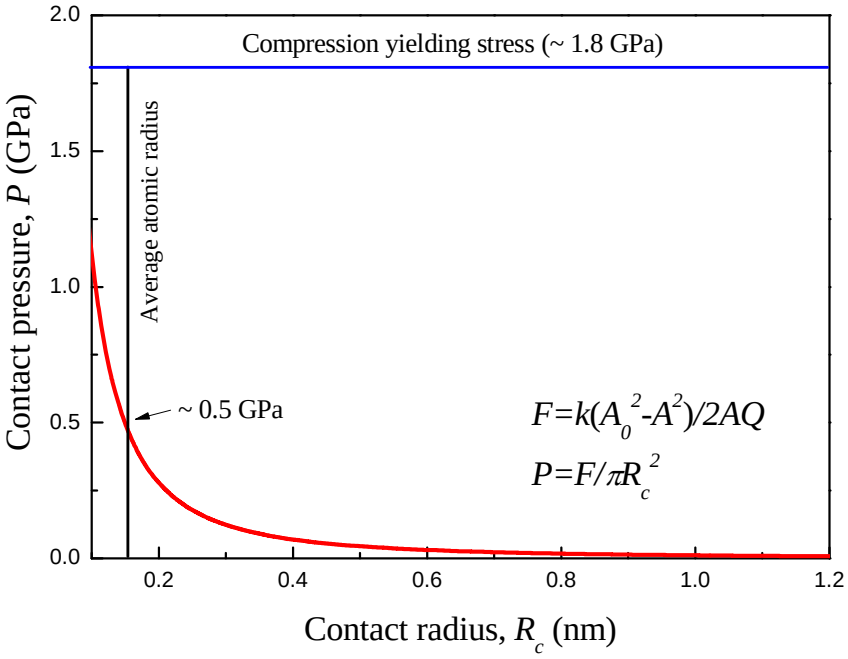

Fig. 4.2. Evaluation of contact pressure P as a function of contact radius R_c. In the equation F is the contact force, k is the spring constant of cantilever, A_0 is the free amplitude, A is the actual amplitude during scanning and Q is the quantity factor. In our case, k = 3.56N/m; A_0 = 18.7 nm; A = 15.8 nm; Q = 324.

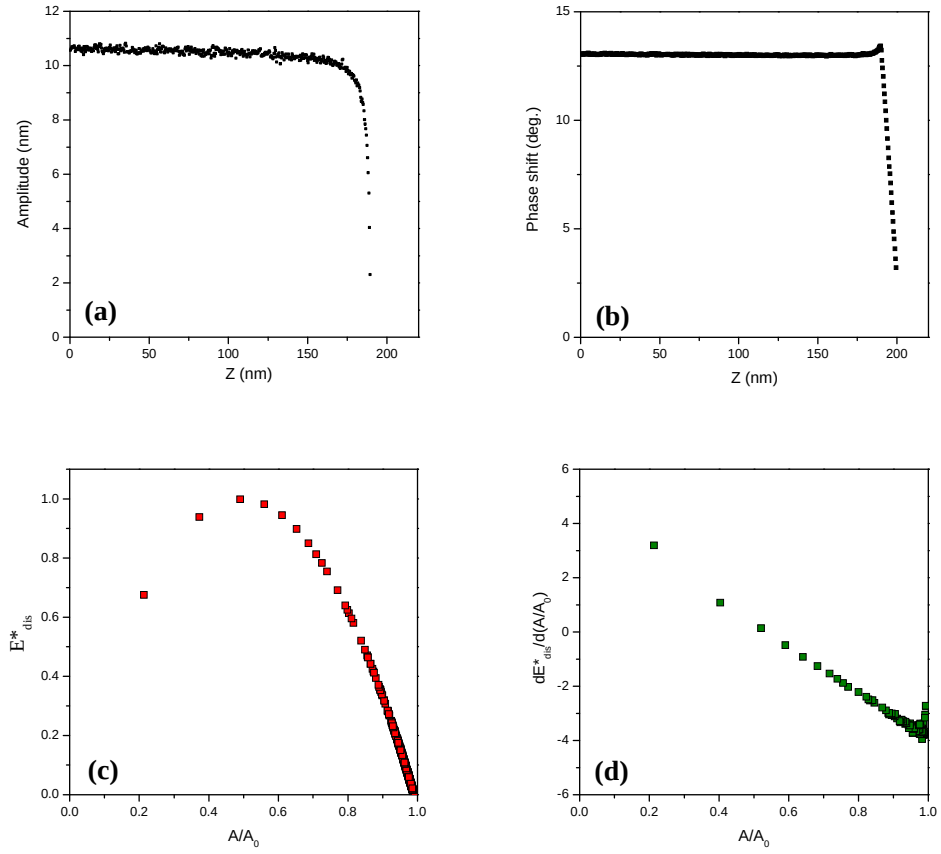

Fig. 4.3. The evolution of (a) amplitude and (b) phase shift as the AM-AFM tip approached to the surface of metallic glass. The (c) normalized dissipation energy and (d) its derivative can be calculated according to their amplitude and phase shift [19].

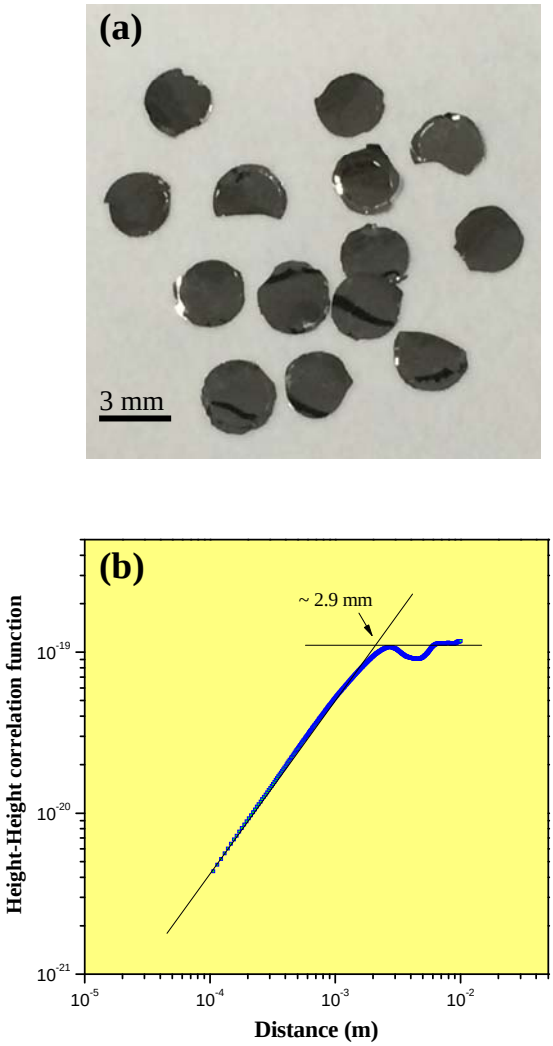

Fig. 4.4. Height-height correlation function. (a) Photo of round samples with a diameter around 3 mm and (b) its corresponding correlation function curve. The correlation function can quantitatively evaluate the mean size of round samples.

4.3 Results and discussion

4.3.1 Phase shift images

Fig. 4.5 present the AM-AFM height and phase shift images of the hyper-quenched metallic glass. The direct observation of the two images indicated no strong correlation between them. The profiles taken from the same area in the two images proved that the spatial heterogeneity in the hyper-quenched metallic glass (**Fig. 4.5b**) was not induced by the surface roughness (**Fig. 4.5a**). The correlation lengths for the height and phase shift images were calculated to be around 10.88 nm and 6.13 nm, respectively (**Fig. 4.6**). As the correlation length for the height image is larger than for the phase shift image, the useful information about phase shift can be obtained.

The phase shift images of the samples after sub-T_g relaxation at 553 K for 5 min, 30 min, 180 min and 720 min are shown **Fig. 4.7**. After sub-T_g relaxation at T_a = 553 K for 5 min, the sizes of spatial heterogeneity became smaller associated with a more dispersed distribution in the matrix (**Fig. 4.7a**). For the longer annealing duration, the spatial heterogeneity sequentially shrank to as small as ~2.59 nm (**Fig. 4.8**). The sample annealed at lower T_a = 473 K and 523 K showed slower processes (**Fig. 4.9**).

The correlation length ξ of the spatial heterogeneity in hyper-quenched metallic glass is calculated to be ~6.13 nm (**Fig. 4. 8**). After annealing for 5min, 30 min, 180 min and 720 min at T_a = 553 K, the correlation length sequentially decreased to around 5.05 nm, 4.28 nm, 3.67 and 2.59 nm. For the same t_a = 180 min, the correlation length decreased to ~5.55 nm at T_a = 473 K and ~4.68 nm at T_a = 553 K (**Fig. 4.10**).

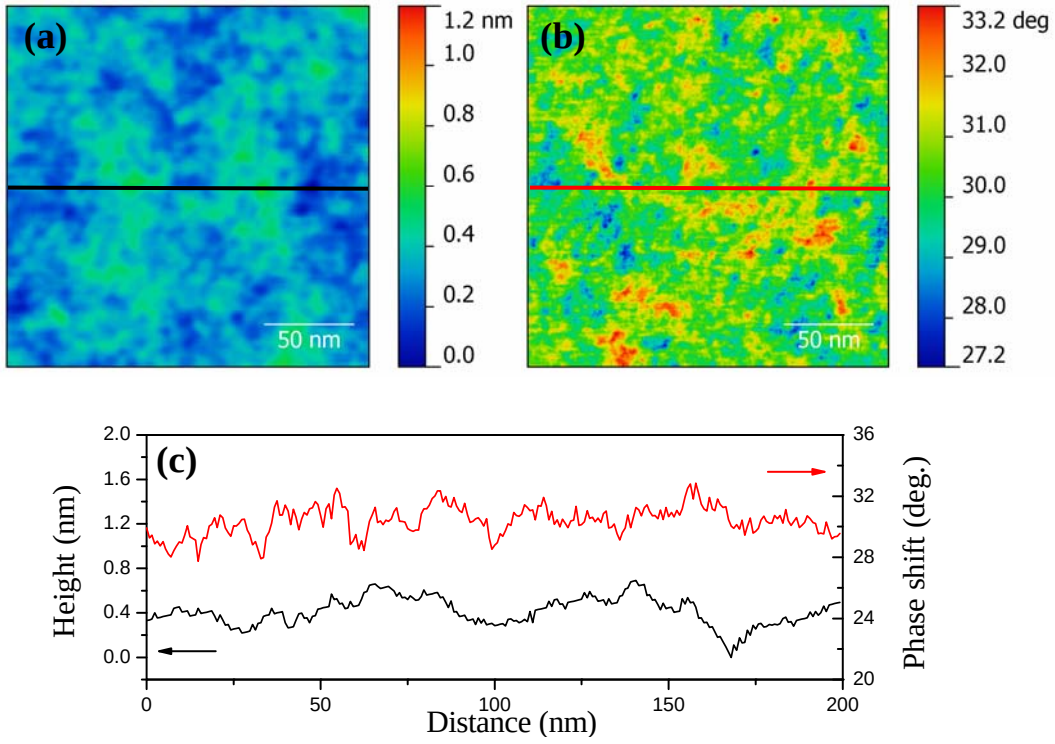

Fig. 4.5. AM-AFM images of the hyper-quenched metallic glass. (a) Height image. (b) Phase shift image. (c) The profiles taken from the same area as marked by the solid line in both images, showing no direct correlation between them.

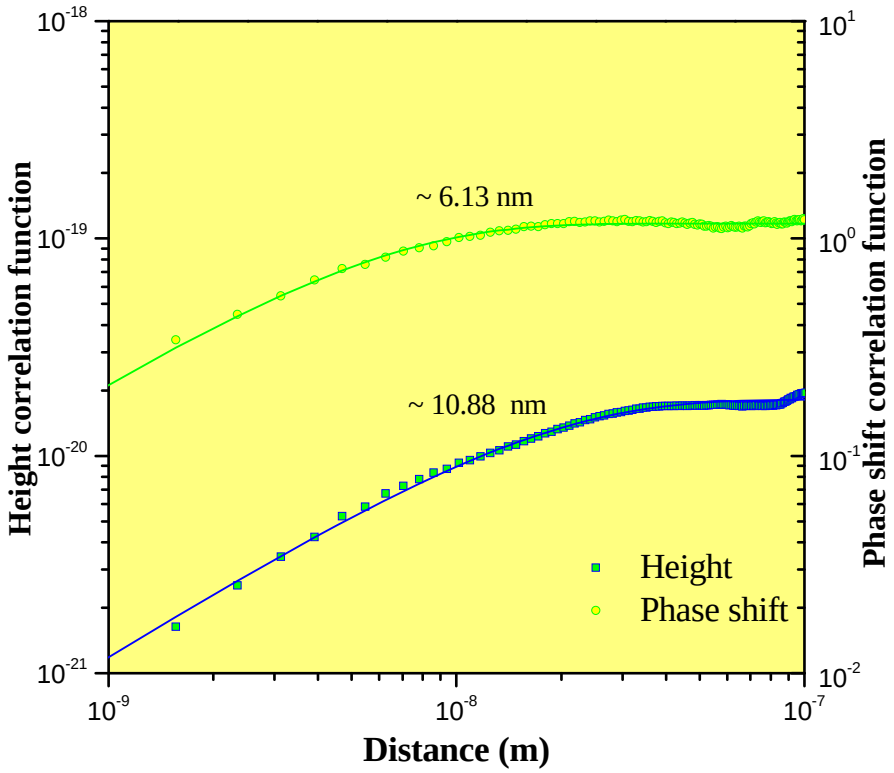

Fig. 4.6. The correlation function curves for the height and phase shift images of hyper-quenched metallic glass.

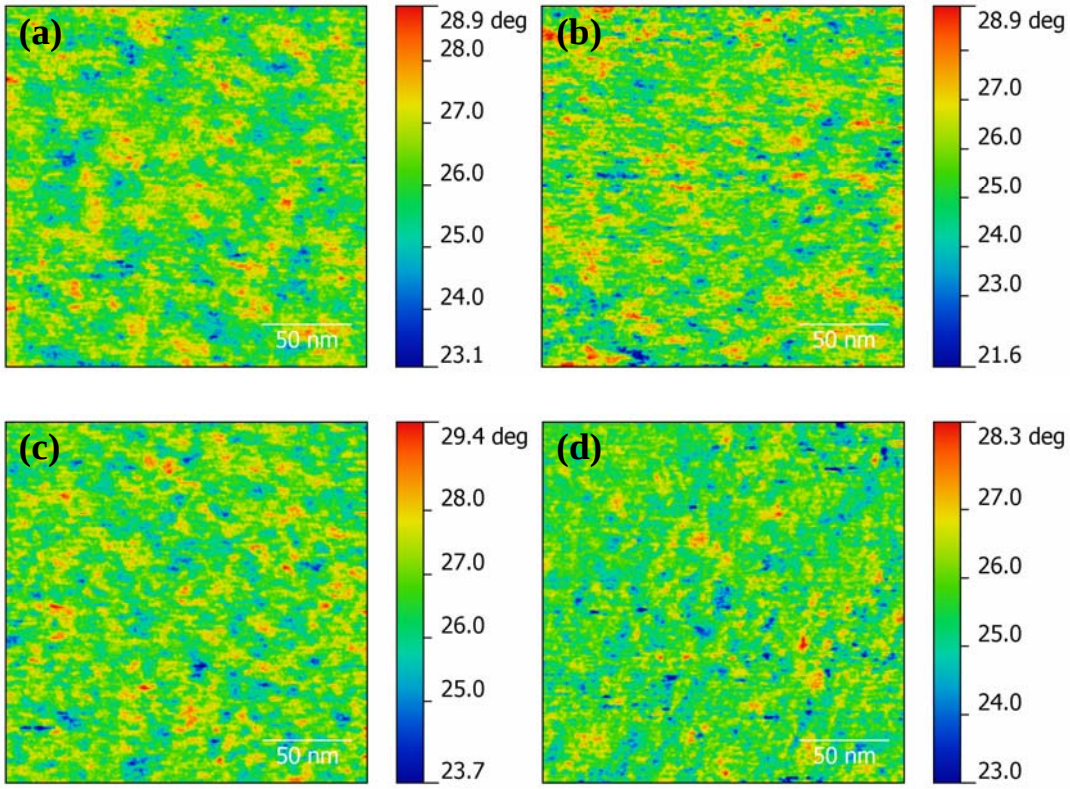

Fig. 4.7. Evolution of spatial heterogeneity during sub-T_g relaxation at T_a = 553 K. Phase shift images of the samples after annealing at 553 K for **(a)** 5 min, **(b)** 30 min, **(c)** 180 min and (**d)** 720 min.

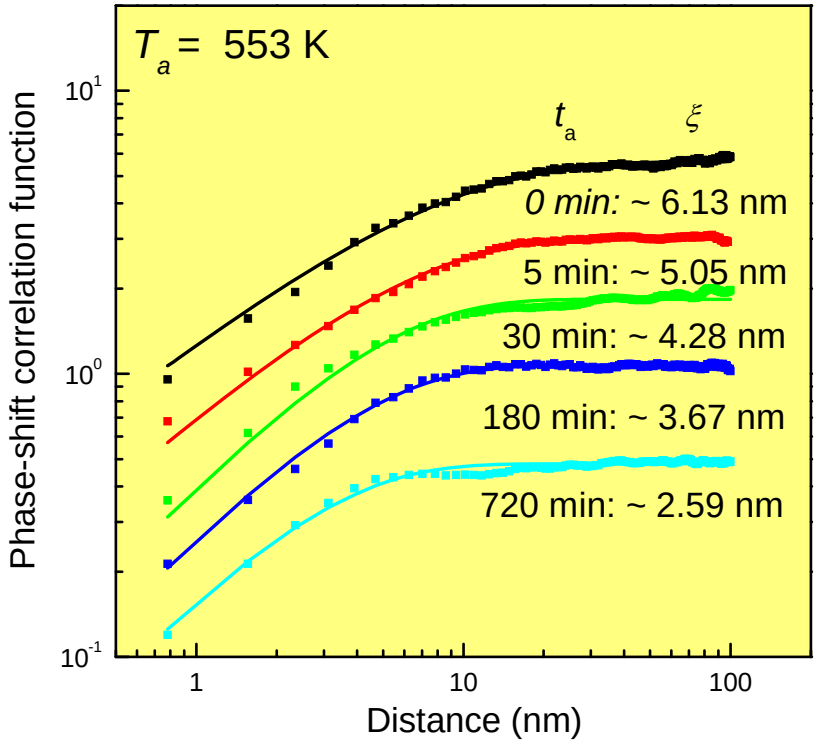

Fig. 4.8. The correlation function curves of samples relaxed at 553 K for different durations. Note that the curves were shifted vertically for clear identification.

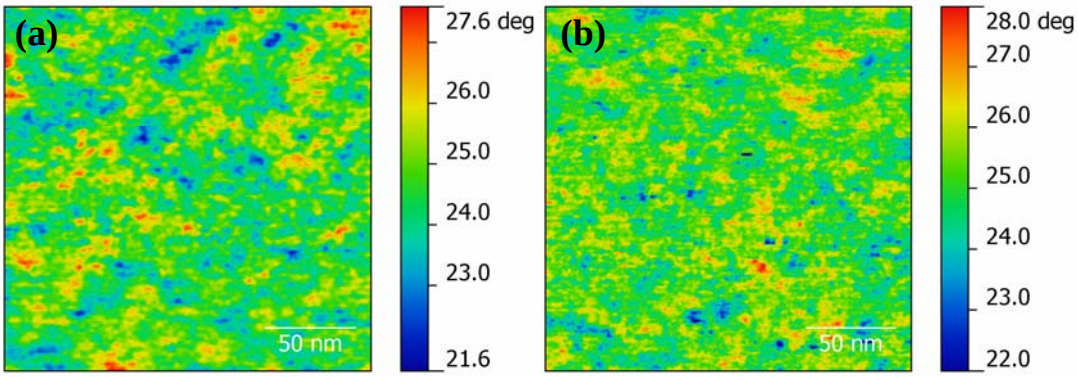

Fig. 4.9. Evolution of nanoscale spatial heterogeneity in samples after sub-T_g relaxation for t_a = 180 min. Phase shift images of samples annealed at **(a)** T_a = 473 K and **(b)** T_a = 523 K.

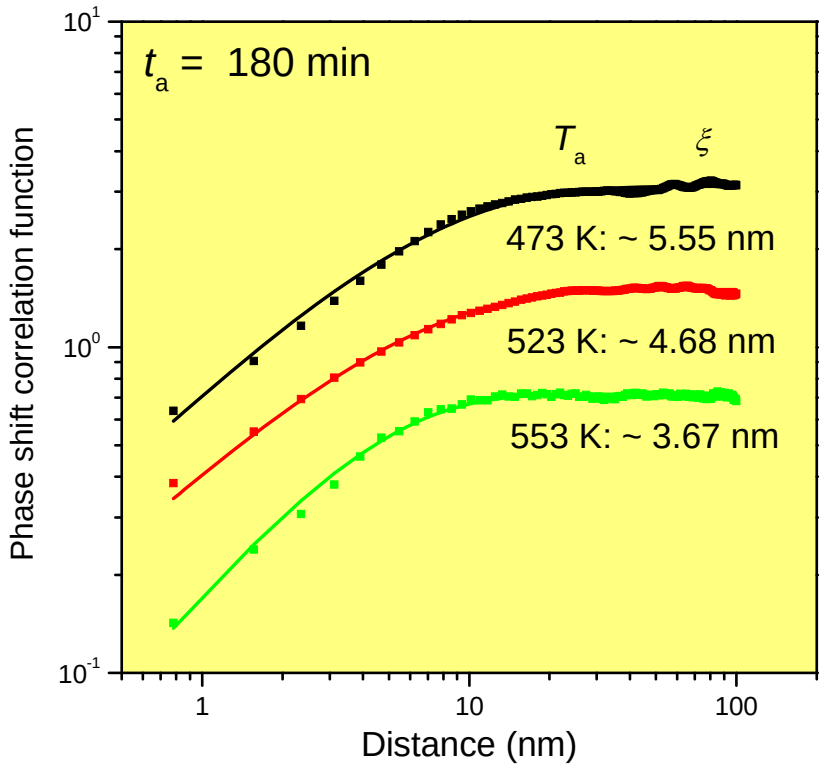

Fig. 4.10. The correlation functions for samples after structural relaxation for t_a = 180 min showing a slower shrinkage of spatial heterogeneity at lower T_a. Note that the curves were shifted vertically for clear identification.

4.3.2 Dynamics of spatial heterogeneity

We analyzed the evolution of spatial heterogeneity during the sub-T_g relaxation at 473 K, 523 K and 553 K. The mean values of correlation lengths were plotted with t_a for all samples, showing T_a dependent relaxation behaviors of the spatial heterogeneity **(Fig. 4.11)**. We used the KWW function $F(t_a) = \exp\left[1-(t_a / \tau_\xi)^{\beta_{KWW}}\right]$ to describe the relaxation behavior of the spatial heterogeneity. The τ_ξ was the characteristic relaxation time for the evolution of spatial heterogeneity. The KWW function is often used to describe the temporal behavior of disordered systems in response to external stimulus, such as applied electric field, stress, and imposed deformation [2]. Since the spatial heterogeneity evolves in a real three-dimensional space, the volume of correlation length is more physically meaningful (**Fig.4.12**). The $F(t_a)$ here was defined as $(\xi/\xi_0)^3$, where ξ_0 was the correlation length of the hyper-quenched metallic glass. The well fittings by the KWW function in **Fig. 4.13** implied that the evolution of spatial heterogeneity was related to the slow-down of dynamics in metallic glasses [1, 18].

It was found that the relaxation time τ_ξ become shorter at higher T_a. We compared τ_ξ with the characteristic relaxation time τ_β derived from the heat release of sub-T_g relaxation in **Fig. 4.14** and found the equivalences between them for all three T_a. According to the Arrhenius equation the activation energy E_ξ of the structural evolution is calculated to be 145 kJ/mol or $25.1RT_g$ (**Fig. 4.15**). Its value is close to the activation energy $E_\beta = 27.2RT_g$ measured by hyperquenching-annealing-calorimetric scan (HAC) approach and in accord with the empirical value $E_\beta = 26.1RT_g$ for the activation energy of β-relaxations [7, 23].

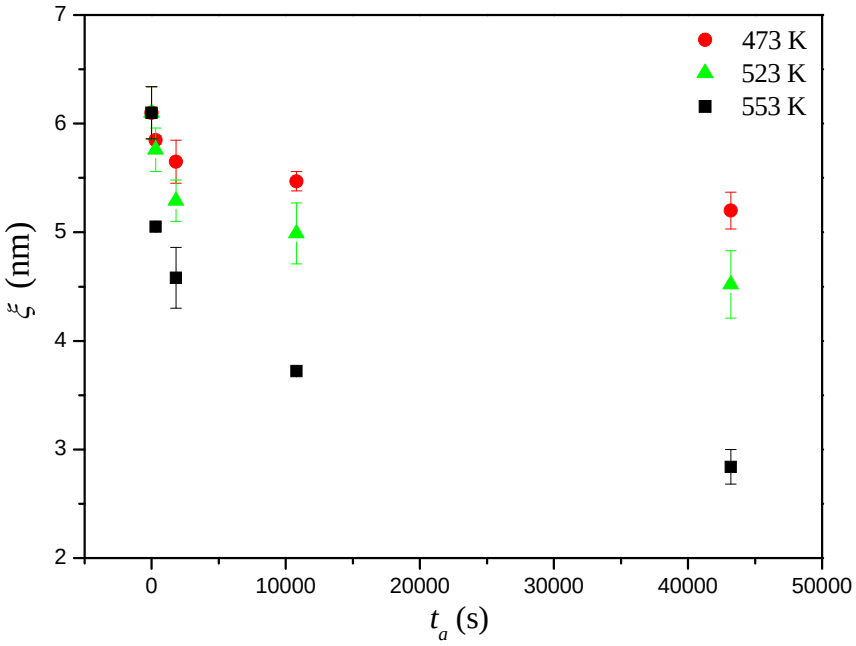

Fig. 4.11. The mean correlation lengths ξ of the hyper-quenched sample and the samples relaxed at 473 K, 523 K and 553 K for different durations.

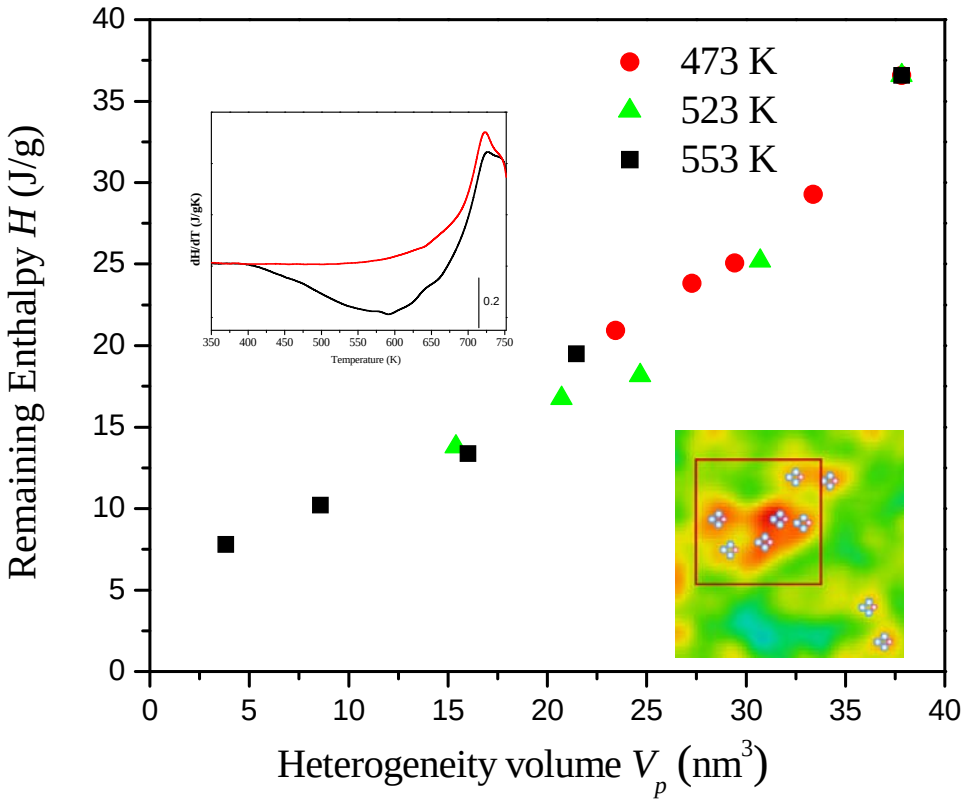

Fig. 4.12. The plot of the remaining enthalpy as a function of the spatial heterogeneity volume showing a linear relation between them.

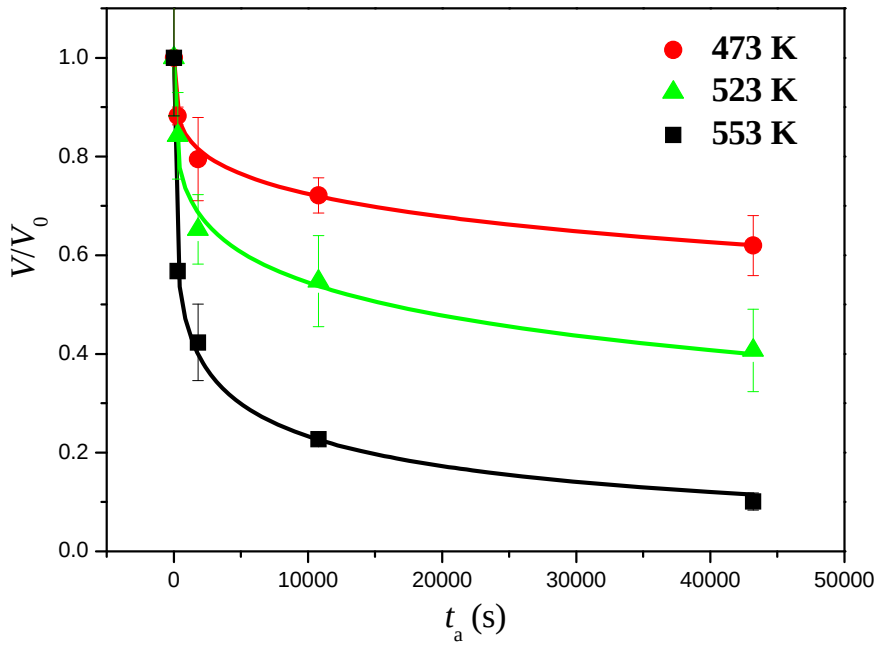

Fig. 4.13. Annealing duration t_a dependences of the normalized spatial heterogeneity volumes $F(t_a)$ and the KWW fittings from which the characteristic relaxation time τ_ξ can be derived.

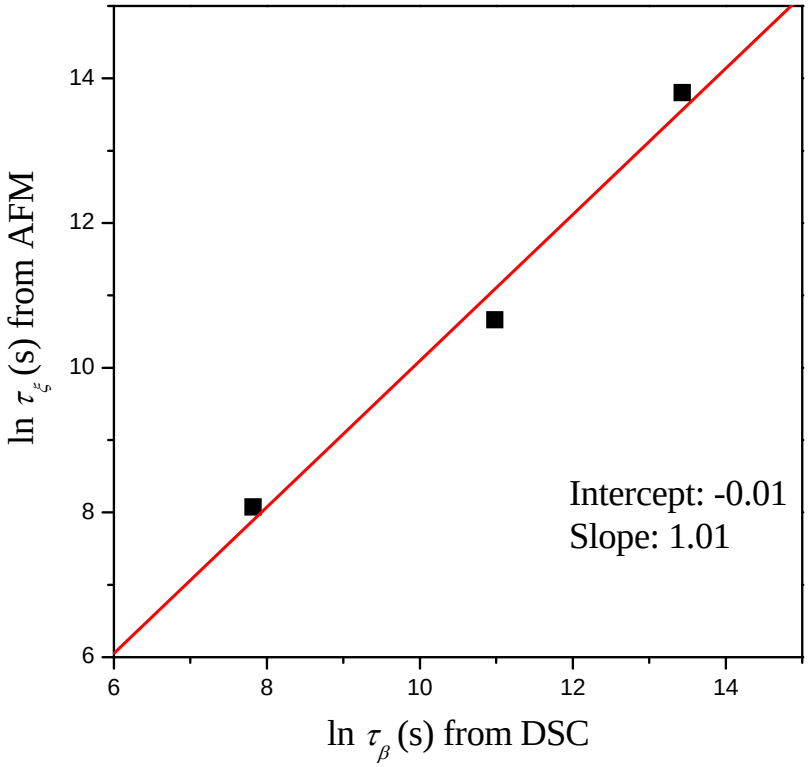

Fig. 4.14. A comparison between the characteristic relaxation times τ_β and τ_ξ derived from the sub-T_g enthalpy relaxation and the evolution of spatial heterogeneity, respectively.

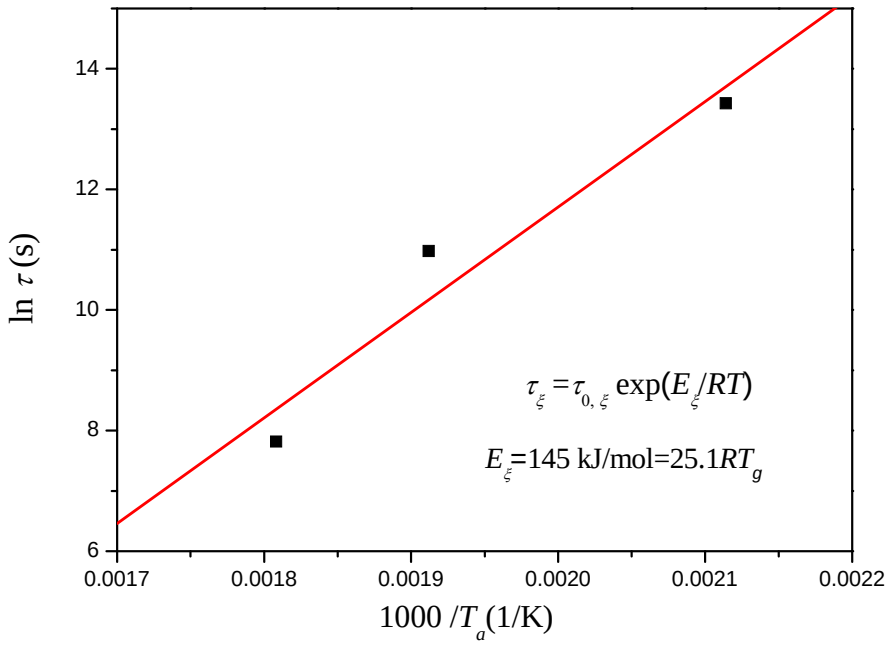

Fig. 4.15. The activation energy of the evolution of spatial heterogeneity can be derived from the dependence of characteristic relaxation time τ_ξ of the spatial heterogeneity volumes on the reciprocal annealing temperature ($1/T_a$).

4.3.3 Dissipation energy

The dissipation energy $E_{dis.}$ for the tip-surface interaction can be calculated from the phase shift and actual amplitude according to the below equation:

$$E_{dis} = \left(\sin\phi - \frac{\omega}{\omega_0}\frac{A}{A_0} \right) \frac{\pi k A A_0}{Q} \quad (1)$$

where ϕ is the phase shift, ω is drive frequency, ω_0 is the resonant frequency of cantilever, A is the actual amplitude, A_0 is the free amplitude, k is the spring constant and Q is the quantity factor [19].

The distribution of dissipation energy for the hyper-quenched metallic glass was presented in **Fig.4.16**. The distribution can well be fitted by the Gaussian function, demonstrating that the distribution was random and no artifacts were introduced during the measurement [20]. The distributions for the hyper-quenched metallic glasses after sub-T_g relaxation at 553 K for 0 min, 5 min and 720 min were shown in **Fig. 4.17**. After sub-T_g relaxation, the distribution of dissipation energy gradually shifted to lower values, indicating that less energy was dissipated for the samples after sub-T_g relaxation (**Fig .4.17a**). The mean value of the dissipation energy decreased from around 4.8 eV for the hyper-quenched metallic glass to less than 4.3 eV for the most relaxed sample as shown in **Fig .4.17b**. Meanwhile, the distributions were narrower and sharper for the samples after sub-T_g relaxation compared with the hyper-quenched metallic glass (**Fig .4.17c, d**). The lower dissipation energy and the sharper distribution implied that the volumes of spatial heterogeneity in the metallic glass decreased and their distributions became more uniform after sub-T_g relaxation.

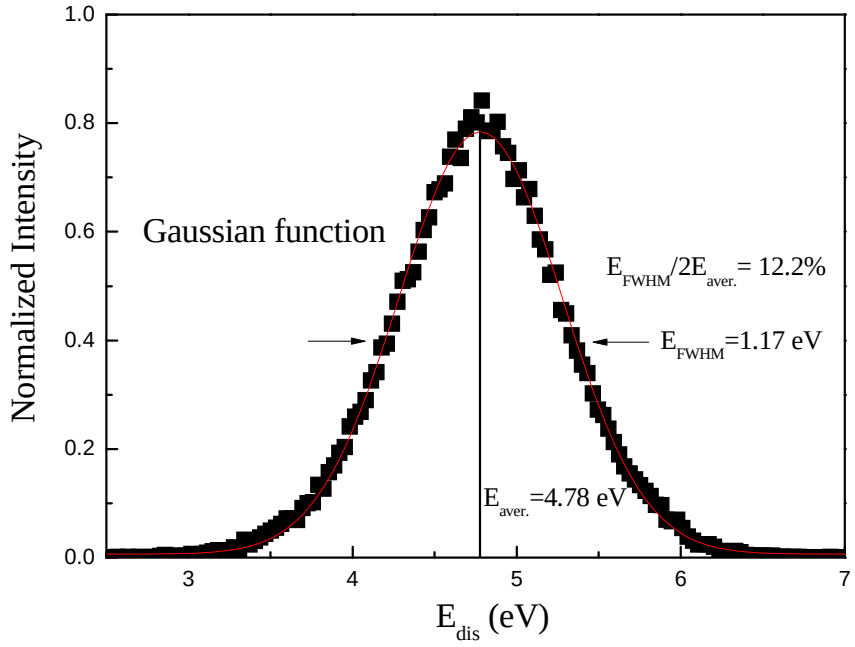

Fig. 4.16. The distribution of dissipation energy for the hyper-quenched metallic glass fitted by the Gaussian function. From the fittings we can get the mean value, the full width at half magnitude (FWHM), and the height for the distribution.

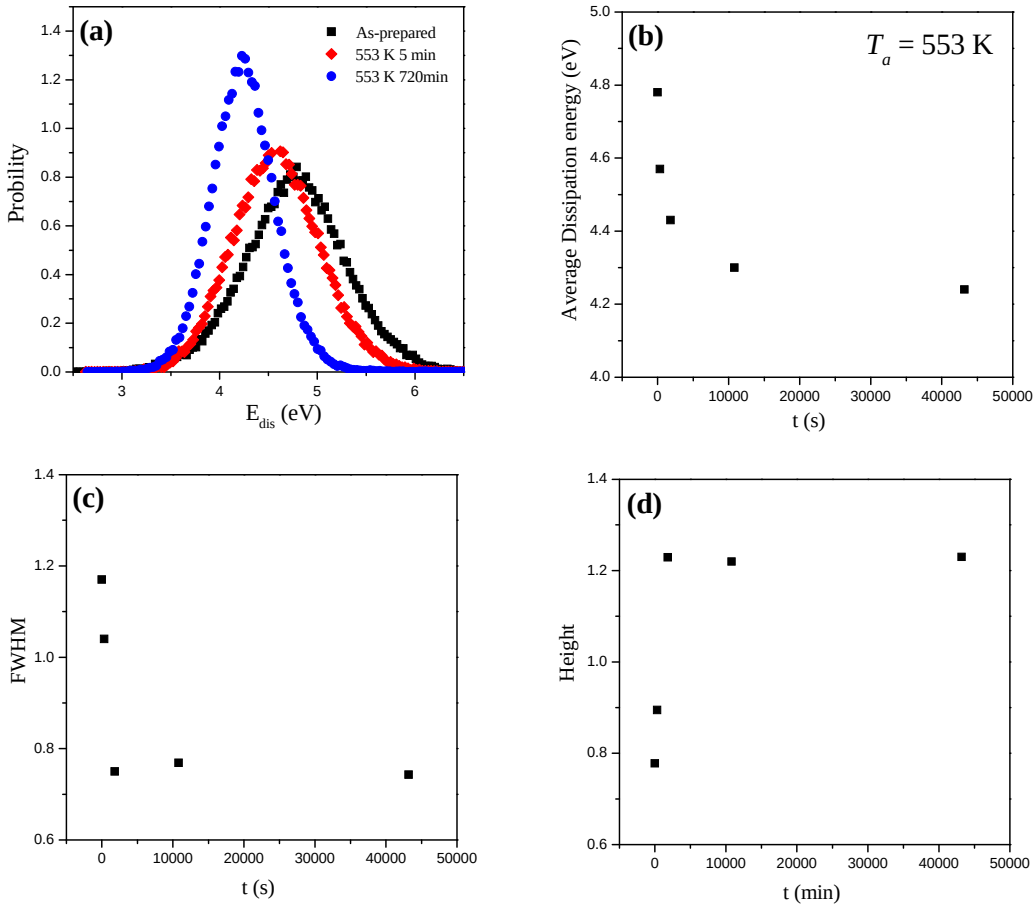

Fig. 4.17. (a) The distribution of dissipation energy for the hyper-quenched metallic glass after sub-T_g relaxation at 553 K. (b) The mean value of dissipation energy plotted with the annealing time. (c) The full width at half magnitude for the distribution. (d) The height for the distribution.

4.3.4 Correlations with β-relaxation

We have shown the correlation of spatial heterogeneity with β-relaxation in the hyper-quenched metallic glass by demonstrating the equivalences of their relaxation times and activation energies. The dynamic-structure correlation can account for some unique features of β-relaxations [11]. In the mechanically rigid glasses, the β-relaxation can not be contributed by the reorientation of spheres about their axis alone, thus the translational motions of small molecules or atoms should take place. However, if all molecules or atoms were involved with such process an external stress will lead to a permanent macroscopic deformation at β-relaxation time scale which has never been observed. On the other hand, if the translational motions were confined to the spatial heterogeneity as we observed here, the above contradiction can be eliminated. In addition, the densification of glasses was expected to increase the strength of β-relaxation peaks which has been realized when the densification was induced by subjecting the glass to a hydrostatic pressure [25, 26]. However, the structural relaxation which also increased the density of a glass led to a decrease in the strength of β-relaxation [3, 11]. The evolution of spatial heterogeneity we observed can account for the different effects of densification that the loosely packed regions facilitating the process of β-relaxation shrunk during the structural relaxation, while the average density of glass increased.

The shrinkage of the spatial heterogeneity correlated with β-relaxation might be processed by the diffusion of small constituting atoms with high mobility whose activation energies were found to be almost the same with those of β-relaxations [14].

Combined with the results of the synchrotron X-ray measurement [16], the full scenario of structure changes for β-relaxations were determined to originate from the diffusion of small constituting atoms leading to short-range collective rearrangements of large solvent atoms confined to the spatial heterogeneity with loose packing. Additionally, the spatial heterogeneity also shares some features with shear transformation zones (STZs) where it assumes the pre-existence of loosely packed clusters facilitating the initiation of deformation beyond the densely packed matrix. This might explain why β-relaxation was found to be correlated with the mechanical properties of some metallic glasses [9, 10].

The origin of the existence of spatial heterogeneity in metallic glass is not completely understood [17]. The spatial heterogeneity was either viewed as a result of slow dynamics, such as density fluctuations [11, 27], or otherwise viewed as a reason for the slow down of dynamics, such as frustration-limited domains [28] and structural basis for fragility [29]. Based on our observations in the metallic glass, it is concluded that the spatial heterogeneity at least gave rise to the slow dynamics of β-relaxation rather than the adverse case. Recently A. Hirata *et al.* [30] reported the geometric frustration of local icosahedra order in metallic glasses by means of angstrom-beam electron diffraction. The detected icosahedra were distorted with partially face-centered cubic symmetry. This experimental observation is in accord with the theory proposed by Kivelson *et al.* [31] that the free-energy preferred molecular or atomic packing can not fill space efficiently and fail to extend indefinitely which give birth to the frustration-limited domains or the spatial heterogeneity in glasses.

4.4 Summary

We investigated the evolution of spatial heterogeneity in a hyper-quenched metallic glass during the sub-T_g structural relaxation. The characteristic relaxation time and activation energy of the dynamics of spatial heterogeneity exhibited the characteristics of β-relaxation. The correlations between spatial heterogeneity and β-relaxation can help us better understand the relaxation processes in metallic glasses and has important implications on producing novel metallic glasses with better properties.

References

[1] P. G. Debenedetti, and F. H. Stillinger, Nature 410, 259 (2001).

[2] G. P. Johari, J. Chem. Phys. 58, 1766 (1973).

[3] G. P. Johari, and M. Goldstein, J. Chem. Phys. 53, 2372 (1970).

[4] K. L. Ngai, Relaxation and Diffusion in Complex Systems, Springer, New York, USA (2011).

[5] C. A. Angell, K. L. Ngai, G. B. McKenna, P. F. McMillan and S. W. Martin, J. Appl. Phys. 88, 3113 (2000).

[6] H. B. Yu, W. H. Wang, H. Y. Bai, and K. Samwer, *Natl. Sci. Rev.* 1, 429-461 (2014).

[7] L. Hu, and Y. Z. Yue, J. Phys. Chem. C 113, 15001 (2009).

[8] T. Ichitsubo, E.Matsubara, T. Yamamoto, H. S. Chen, N. Nishiyama, J. Saida, and K. Anazawa, Phys. Rev. Lett. 95, 245501 (2005).

[9] W. H. Wang, J. Appl. Phys. 110, 053521 (2011).

[10] H. B. Yu, X. Shen, Z. Wang, L. Gu, and W. H. Wang, Phys. Rev. Lett. 108, 015504 (2012).

[11] G. P. Johari, J. Non-crystal. Solids. 307, 317 (2002).

[12] M. S. Thayyil, S. Capaccioli, D. Prevosto, and K. L. Ngai, Philos. Mag. 88, 4007 (2008).

[13] J. D. Stevenson, and P. G. Wolynes, Nature Phys. 6, 63 (2010).

[14] H. B. Yu, K. Samwer, Y. Wu, and W. H. Wang, Phys. Rev. Lett. 109, 095508 (2012).

[15] H. B. Yu, K. Samwer, W. H. Wang and H. Y. Bai, Nature Commun. 4, 2204 (2013).

[16] Y. H. Liu, T. Fujita, D. P. B. Aji, M. Matsuura and M. W. Chen, Nature Commun. 5, 3328 (2014).

[17] M. D. Ediger, Annu. Rev. Phys. Chem. 51, 99 (2000).

[18] Z. Wang, B. A. Sun, H. Y. Bai and W. H. Wang, Nature Commun. 5, 5823 (2014).

[19] R. García, R. Magerle, and R.Perez, Nature Mater. 6, 405 (2007).

[20] Y. H. Liu, D. Wang, K. Nakajima, W. Zhang, A. Hirata, T. Nishi, A. Inoue and M. W. Chen, Phys. Rev. Lett. 106, 125504 (2011).

[21] H. Wagner, D. Bedorf, S. Küchemann, M. Schwabe, B. Zhang, W. Arnold, and K. Samwer, Nature Mater. 10, 439 (2011).

[22] Y. Yang, J. F. Zeng, A. Volland, J. J. Blandin, S. Gravier, and C. T. Liu, Acta Mater. 60, 5260 (2012).

[23] K. L. Ngai, and S. Capaccioli, Phys. Rev. E 69, 031501 (2004).

[24] J. Hachenberg, D. Bedorf, K. Samwer, R. Richert, A. Kahl, M. D. Demetriou, and W. L. Johnson, Appl. Phys. Lett. 92, 131911 (2008).

[25] J. Köplinger, G. Kasper, and S. Hunklinger, J. Chem. Phys. 113, 4701 (2000).

[26] K. L. Ngai, and M. Paluch, J. Chem. Phys. 120, 857 (2004).

[27] M. D. Ediger, J. Non-Cryst. Solids 235, 10 (1998).

[28] D. Kivelson, S. A. Kivelson, X. Zhao, Z. Nussinov, and G. A. Tarjus, Phys. A 219, 27 (1995).

[29] N. A. Mauro, M. Blodgett, M. L. Johnson, A. J. Vogt, and K. F. Kelton, Nature Commun. 5, 4616 (2014).

[30] A. Hirata, L. J. Kang, T. Fujita, B. Klumov, K. Matsue, A. R. Yavari and M. W. Chen, Science 341, 376 (2013).

[31] D. Kivelson, S. A. Kivelson, X. L. Zhao, Z. Nussinov, anfd G. Tarjus, Phys. A 219, 27 (1995).

Chapter 5

Mechanical Behaviors

5.1 Introduction

One merit of metallic glasses is the high strength well in excess of their crystalline counterparts due to the non-periodic microstructure and the absence of dislocation-based flow [1-6]. And for the same reasons, they always yield and fracture in localized shear banding without any plasticity at room temperature [7-11]. The poor understanding of the atomic structure of disordered metallic glasses [12] make a definite correlation between the mechanical behavior and atomic structures for metallic glasses still missing. Also, the localized shearing deformation mode limits the thorough investigations via conventional mechanical measurements [3, 11]. Nanoindentation, which can detect the tremendously tiny change in displacement of a deformed sample at a nanometer scale, is a powerful and sensitive tool for characterizing the microscopic mechanisms of metallic glass deformation [3, 13]. The anelastic deformation and creep behavior far below T_g (glass transition temperature) in metallic glasses have been extensively investigated by the constant-load nanoindentation [14-17]. Although several theoretical models, such as liquid-like regions, heat release, free volumes, etc. have been proposed to explain the low-temperature and time-related deformation in metallic glasses, the underlying mechanisms remain debating for years.

The micromechanism of deformation in metallic glass is commonly attributed to

the cooperative shear motion of atomic clusters termed shear transformation zones (STZs) [8]. The cooperative shearing model (CSM) [9, 18] assumed the pre-existence of STZs where the initiation of plastic deformation is easier to be driven. These models certainly demand for the inhomogeneous microstructure in metallic glasses that some local areas have weaker atomic bonding than the surroundings. A simulation [19] has identified soft spots defined from the vibrational modes in a 3D model mimicking realistic $Cu_{64}Zr_{36}$ metallic glass, and found them to be strongly correlated with shear transformation. However, the direct observation of the spatial heterogeneity is limited for the conventional characterization methods due to the disorder structure of metallic glasses, and the experimental result on the correlations between spatial heterogeneity and mechanical behaviors is still missing. The spatial heterogeneity with a correlation length of ~2.5 nm has been reported in a Zr-base metallic glass using the amplitude-modulation dynamic atomic force microscopy (AM-AFM) [20]. The spatial heterogeneity might account for the mechanical behaviors of metallic glasses.

Different from crystals, rigid glasses have an intrinsic relaxation mode below a critical temperature T_c (around $1.2T_g$,) [21, 22], which shows similar pressure and temperature dependences with the primary α relaxation near T_g [23]. Such kind of low-temperature secondary relaxation is termed β-relaxation and has been observed in metallic glasses as pronounced peaks or excess wings in differential scanning calorimeter (DSC) profiles and dynamic mechanical analyzer spectra [24]. While the α relaxations exhibit non-Arrhenius temperature dependence and vanish at temperatures below T_g, the β-relaxations remain to room temperature [25, 26]. The β-relaxations

might play an important role in the low-temperature dynamics and rheology of metallic glasses, particularly at low deformation rates.

In this work, we investigated the effects of β-relaxation correlated sub-T_g relaxation on mechanical properties and deformation behaviors of the hyper-quenched metallic glass using instrumented nanoindentation. After the sub-T_g relaxation, the metallic glass became harder, less deformable and its rheology was slower. The spatial heterogeneity was found to have strong correlations with hardness and creep of the metallic glasses. The origin was discussed based on the equilibrium of activation energy for the creep and β-relaxation in the metallic glass.

5.2 Experimental

Sample preparation. The hyper-quenched metallic glass with a composition of $Zr_{53}Cu_{36}Al_{11}$ (at. %) was prepared by RF magnetron sputtering at room temperature.

Sub-T_g relaxation. The hyper-quenched samples were annealed at T_a = 473 K ($0.68T_g$), 523 K ($0.75T_g$) and 553 K ($0.8T_g$) for t_a = 5 min, 30 min, 180 min and 720 min. The sample marked with t_a = 0 min indicates the hyper-quenched metallic glass.

Instrumented indentation. The mechanical properties were measured by Nanoindenter equipped with a Berkovich indenter tip. The force was applied to 50 mN at 0.1 mN/s, then held for 5s, and unloaded at 0.1 mN/s. 25 points with spacing of 50 um were indented for each sample to get the mean value of hardness and modulus. The creep testing was set to automatically start when the thermal drift was less than 0.02 nm/s.

5.3 Results and Discussion

5.3.1 Mechanical properties

The mechanical properties of the hyper-quenched and relaxed metallic glasses were measured using the instrumented nanoindentation. The force-depth curves for the samples before and after sub-T_g relaxation at 473 K, 523 K and 553 K for different durations were shown in **Fig. 5.1**. At the peak loading of 50 mN, the depth of the hyper-quenched metallic glass was measured to be ~ 605 nm. The depth became shorter for longer duration during the sub-T_g relaxation. After annealing at T_a = 553 for 720 min, the depth gradually decreased to ~ 572 nm, indicating that the metallic glass became harder for longer annealing time. The samples annealed at low T_a = 473 K and 523 K showed less decrease in depth compared with those at T_a = 553 K, implying that the effect of sub-T_g relaxation on mechanical properties was temperature dependent and it was more active at higher T_a.

According to the Olive-Pharr method [27] the hardness and modulus for all the samples were derived from the corresponding force-depth curves as shown in **Fig. 5.2**. Obviously, the hardness and modulus of the hyper-quenched metallic glass showed the lowest values of ~6.452 ± 0.196 GPa and 124.356 ± 2.612 GPa, respectively. During the sub-T_g relaxation, the hardness and modulus increased with the annealing time, and increased more progressively at higher T_a. The hardness and modulus can reach as high as 6.924 ± 0.204 GPa and 137.694 ± 7.808 GPa, respecitively for the samples annealed at 553 K for 720 min.

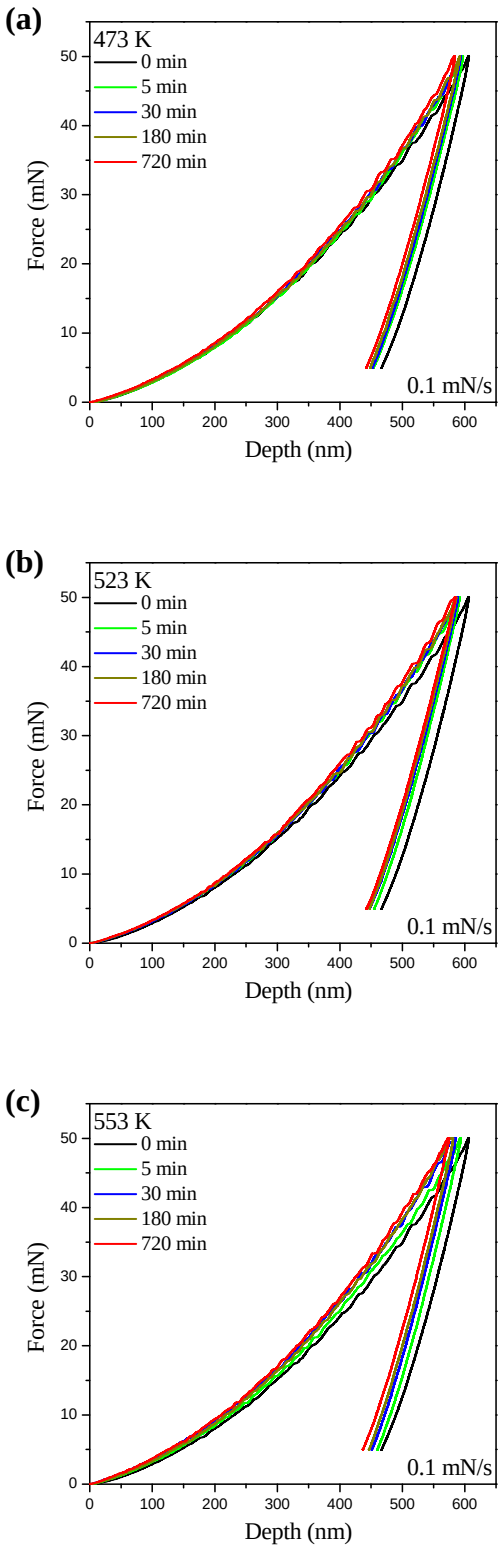

Fig. 5.1. Force-depth curves for samples relaxed at (a) 473 K, (b) 523 K and (c) 553 K for different durations

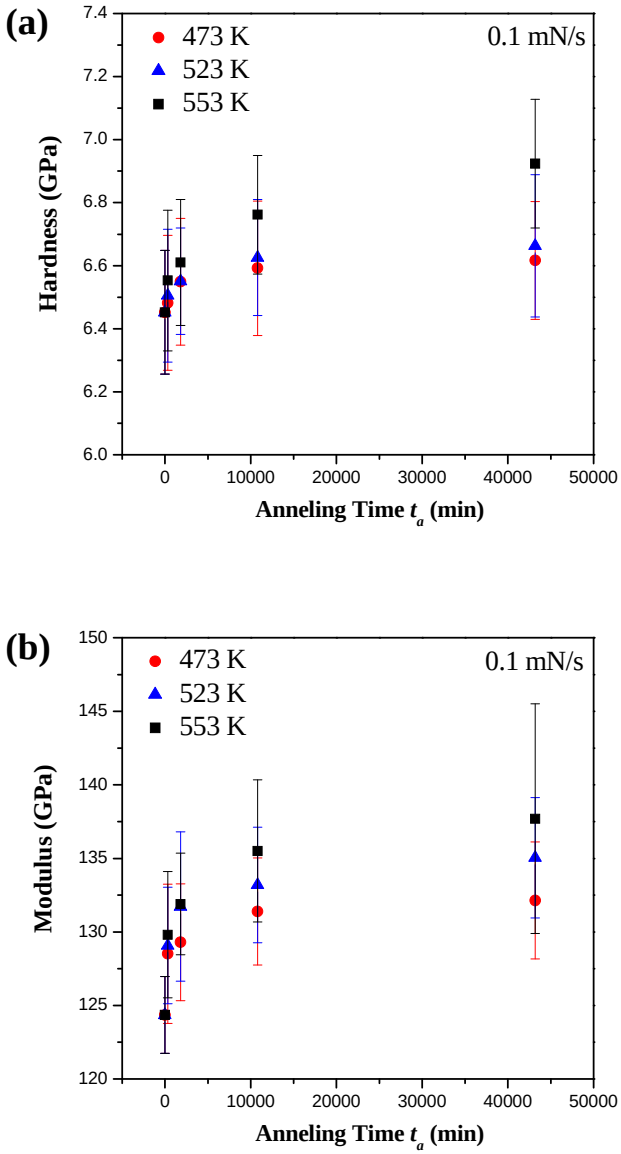

Fig. 5.2. Nanoindentation (a) hardness and (b) modulus plotted with the annealing time for different T_a.

5.3.2 Creep behaviors

The creep can reveal more tiny deformation details in metallic glasses [14-17]. **Fig. 5.3** illustrated the loading procedure for the nanoindentation creep measurements. The loading P was applied to 50 mN in one second, held for 50 seconds, and then unloaded in one second. The displacement into sample h during the holding segment was picked up for the analysis. We analyzed the time dependence of the penetration depth under an applied stress by a KWW-type equation with a form of $h = h_0\left[1-\exp(-(t_h/\tau_h)^{\beta_h})\right]$, where h_0 was the amplitude of the displacement, τ_h and β_h were the characteristic time and the fitting parameter for the nanoindentation strain relaxation **(Fig. 5.4)**. This KWW-type equation has been applied for the stress relaxation of metallic glasses, and the fitting parameter β_h was utilized as an index of the extent of spatial heterogeneity in metallic glasses [28].The creep measurements were performed on the hyper-quenched sample and the samples after sub-T_g relaxation at 553 K for 5 min, 30 min, 180 min and 720 min. The evolution of displacement with holding time t_h for each sample was presented in **Fig. 5.5a**. The hyper-prepared sample showed the most pronounced penetration as deep as 8 nm at the maximum holding time of 50 seconds. With the increase in the annealing time, the penetration depth became smaller and smaller to less than 4 nm for the sample annealed for 720 min. The time-depth curves in Fig. 5 were fitted by the KWW-type equation and presented in **Fig. 5.5b**. The fitting details are summarized in **Table 5.1**.

To explore the intrinsic correlation between the creep and β-relaxation, we plotted h_0, τ_h and β_h as functions of the annealing time t_a for the samples annealed at 553 K

(**Fig. 5.6**). Apparently, the creep displacement is closely associated with the inherent structure of metallic glasses. The displacement amplitudes sequentially decreased from 13.1 nm to 7.2 nm while the relaxation time increased from 59.2 s to 95.3 s ((**Fig. 5.6a**). The decrease in h_0 with longer t_a indicated that the excess enthalpy released by β-relaxation would lead to an inferior deformability in metallic glass and enhance the resistance against low-temperature uniform deformation. This is in agreement with the embrittlement and the loss in impact toughness found in a Zr-base metallic glass after the sub-T_g relaxation [29, 30]. The increase in τ_h with longer t_a suggested a slower response of the rheology of metallic glasses to the applied stress (**Fig. 5.6a**). The parameter β_h in the KWW function was an indicator of the dynamic heterogeneity in disorder systems [28]. For the case in creep measurement, the smaller value of β_h indicated a more heterogeneous time-dependent deformation in the metallic glasses after sub-T_g relaxation (**Fig. 5.6b**).

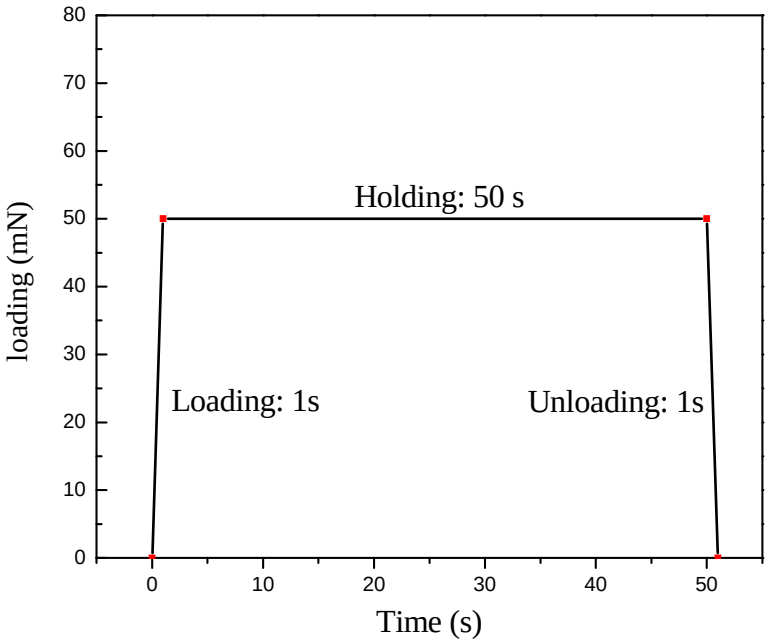

Fig. 5.3. The schematic of loading procedure of creep measurement. The loading *P* was applied to 50 mN in one second, held for 50 seconds, and then unloaded in one second.

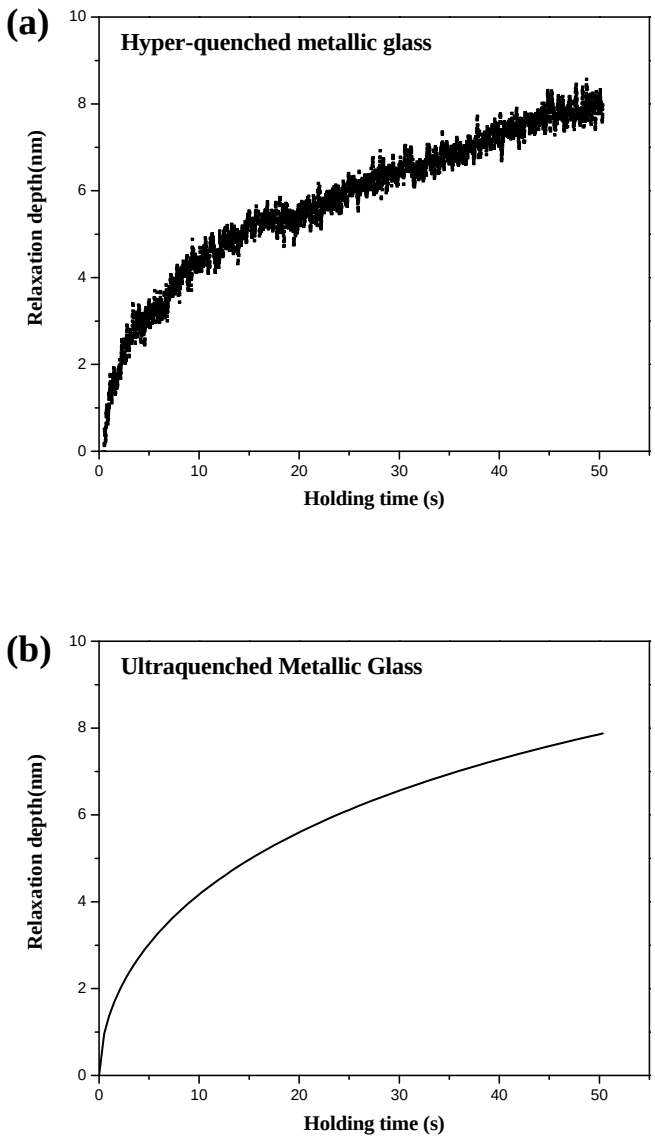

Fig. 5.4. Creep result and its fitting. (a) Indenter displacement with holding time for the hyper-quenched metallic glass and (b) its corresponding KWW fitting.

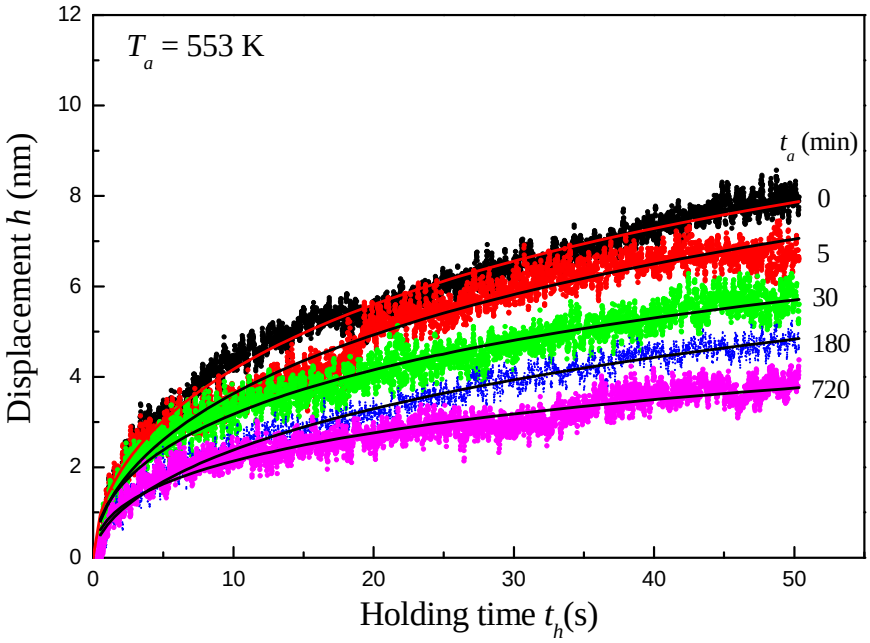

Fig. 5.5. The holding time (t_h) dependence of the indenter displacement (h) of the samples annealed at 553K for different durations under a constant loading of 50mN. The continuous lines are fitting curves for the raw data.

Table 5.1. The creep amplitude h_0, characteristic relaxation time τ_h for the creep and the stretching parameters β_h extracted from the fitting curves of the nanoindentation creep for the sample annealed at 553 K.

t_a (min)	h_0 (nm)	τ_h (s)	β_h
0	13.1	59.2	0.54
5	12.4	69.4	0.52
30	10.2	75.2	0.49
180	9.2	85.0	0.47
720	7.2	95.3	0.46

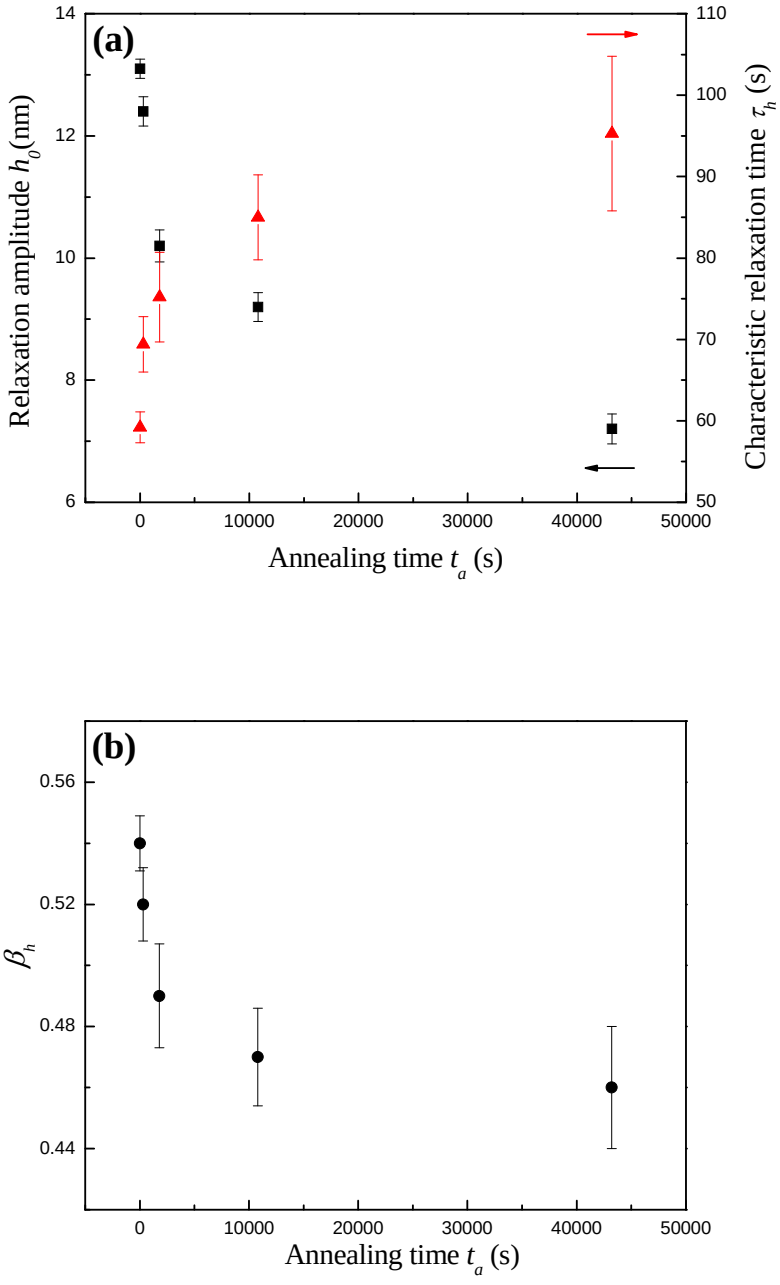

Fig. 5.6. The annealing time (t_a) dependences of (a) the relaxation amplitude (h_0) and the characteristic relaxation time (τ_h); (b) the stretching parameter (β_h).

5.3.3 Activation energy

The shear strain rate $\dot{\gamma}$ and the shear stress τ can be derived from the creep time-displacement curve [31] using the below two equations

$$\tau = \frac{\sigma}{\sqrt{3}} = \frac{P}{3\sqrt{3}A(h)} \tag{1}$$

$$\dot{\gamma} = 0.16\frac{1}{h}\frac{dh}{dt} \tag{2}$$

where σ is the normal stress equivalent to one third of hardness, and $A(h)$ is the indented contact area. The activation energy of the creep can be evaluated by the Cooperative Shear Model (CSM) [9] following an equation:

$$\dot{\gamma} = \dot{\gamma}_0 \exp\left[-\frac{W_{\mathrm{CSM}}}{kT}\left(1-\frac{\tau}{\tau_c}\right)^n\right] \tag{3}$$

where $\dot{\gamma}_0$ is a proportional constant around $10^{10}\mathrm{s}^{-1}$; W_{CSM} is the activation energy for the deformation when the shear stress is zero; τ_c is a critical stress for the cooperative shear; and n is a power constant and chosen to be 1. The activation energy W_{CSM} can be evaluated by fitting the curve in **Fig. 5.7** using CSM. The derived W_{CSM} of the low-rate deformation was around $24.3RT_g$ or 1.45 eV for the hyper-prepared metallic glass which was very close to the value of $27.2RT_g$ for the β-relaxation. After sub-T_g relaxation, the activation energy slightly increased to 1.46 eV and 1.52eV for the sample annealed at 553 K for 5min and 30 min, respectively (**Fig. 5.8)**. However, for the sample annealed longer than 180 min at 553 K, the activation energy increased dramatically and showed a huge deviation from 1.45 eV or $24.3RT_g$ which can be attributed to the exhaustion of β-relaxation due to the sub-T_g relaxation.

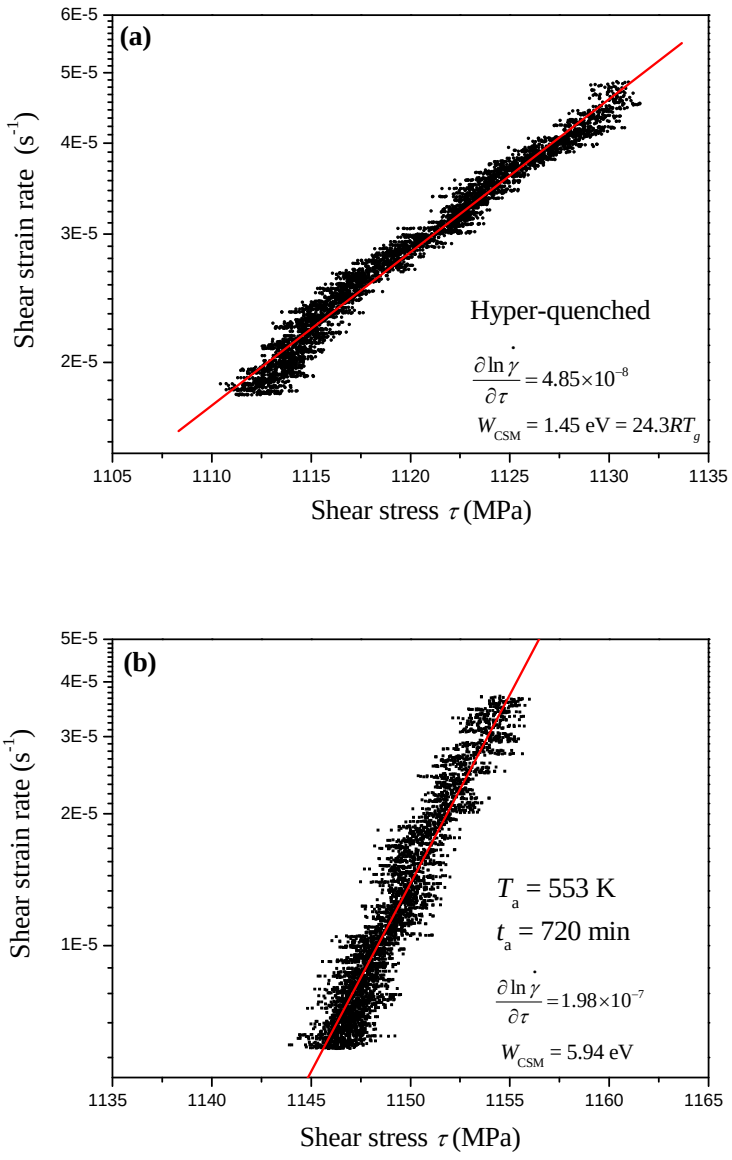

Fig. 5.7. Logarithmic shear strain rate as a function of shear stress τ derived from the nanoindentation creep for (a) the hyper-quenched metallic glass and (b) the samples relaxed at 553 K for 720 min.

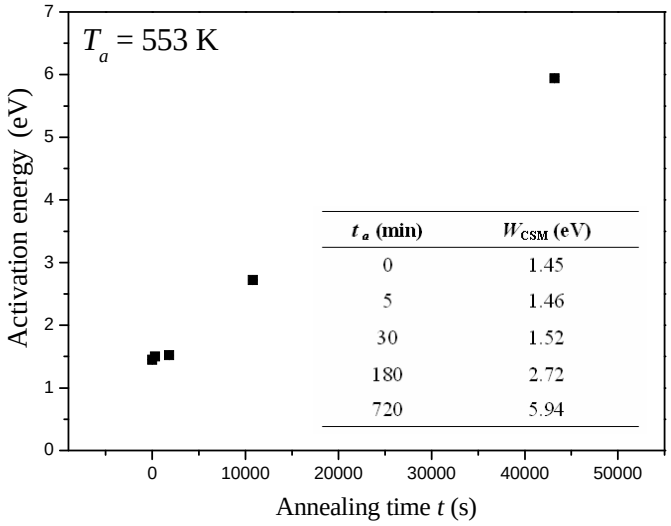

Fig. 5.8. The activation energies for the hyper-quenched metallic glass and samples relaxed at 553 K derived according to the Cooperative Shear Model (CSM). Inset is the summary of the activation energy with annealing time t_a.

5.3.4 Structure-property correlations

As we showed in the last chapter, the spatial heterogeneity in metallic glass shared the same origin with β-relaxation, and it is interesting to see if such spatial heterogeneity plays some roles in the mechanical behaviors of metallic glasses. We plotted the correlation lengths of spatial heterogeneity with their corresponding hardness as shown in **Fig. 5.9**. A clear linear relationship with a negative slop can be seen. The hyper-quenched sample which had the largest correlation length of ~6.13 nm showed the lowest hardness around 6.452 GPa among the samples. After sub-T_g relaxation, the correlation length decreased, while the hardness sequentially increased to as high as ~6.924 GPa for the most relaxed sample whose correlation length was smallest around 2.59 nm. Although these samples were annealed at different temperatures for different durations, in this plot their measured properties could be unified: the sample with larger spatial heterogeneity was softer, and vice versa.

We plotted h_0 and τ_h as functions of the corresponding correlation lengths of structural heterogeneity (**Fig. 5.10**). Apparently, the creep was closely associated with the microstructure of metallic glasses. The displacement amplitudes showed the same trend with the correlation lengths, increasing from 7.2 nm to 13.1 nm as the correlation length increased from ~2.59 nm to ~6.13 nm (**Fig. 5.10a**). The increase in h_0 indicates that the larger structural heterogeneity corresponds to a better deformability in metallic glass. The characteristic relaxation time of the creep became shorter from 95.3 s to 59.2 s when the correlation lengths were larger (**Fig. 5.10b**). It means the rheology in the metallic glass with larger structural heterogeneity is more rapid.

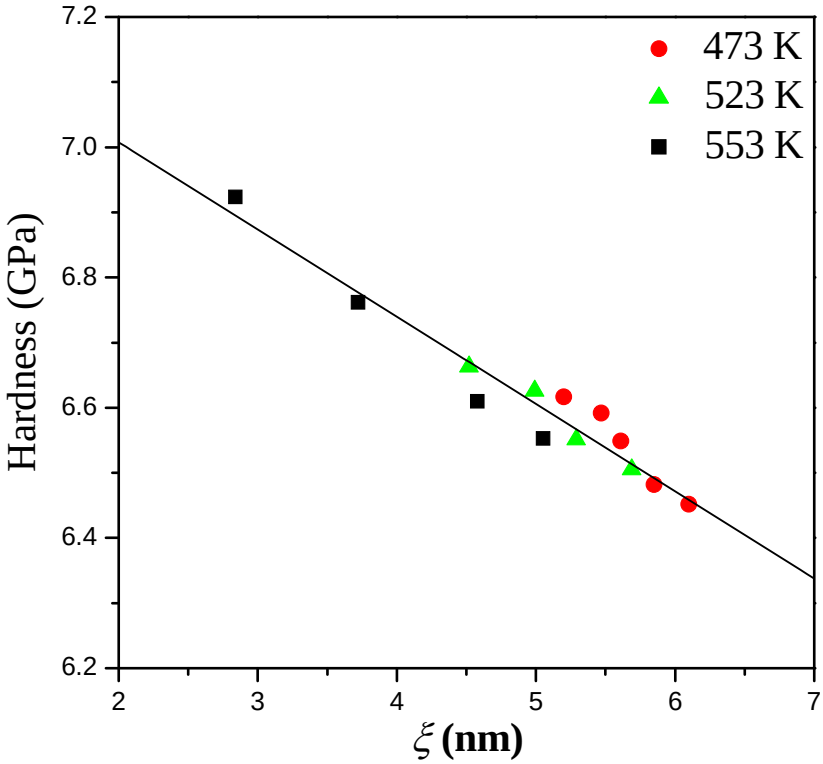

Fig. 5.9. Nanondentation hardness as a function of correlation lengths of spatial heterogeneity for samples relaxed at 473 K, 523 K and 553 K for different durations.

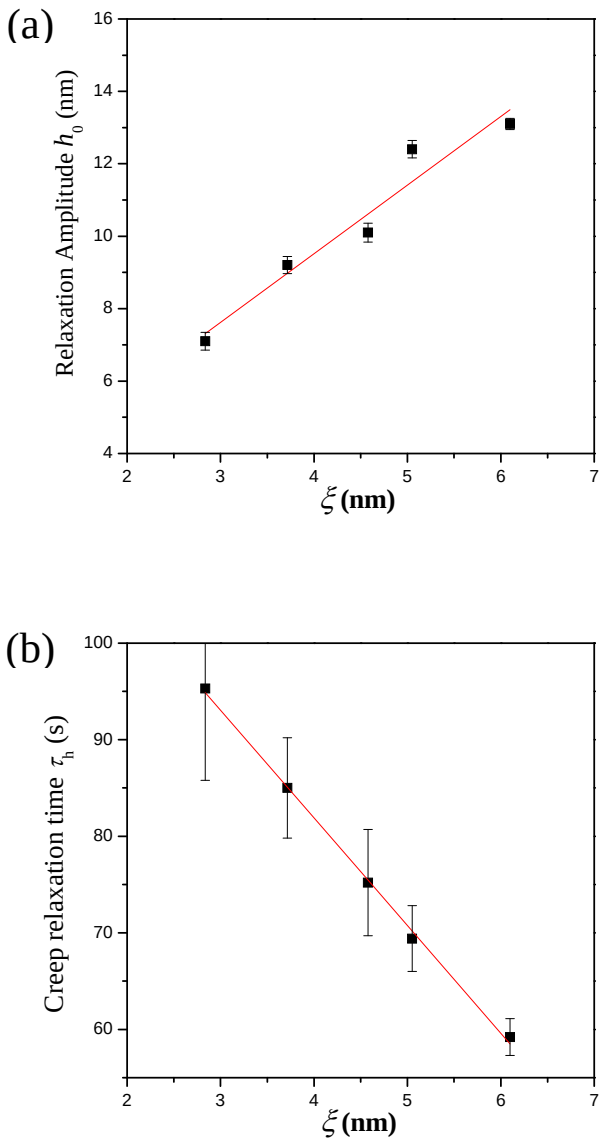

Fig. 5.10. (a) The creep relaxation amplitude (h_0) and (b) characteristic relaxation time (τ_c) versus the correlation lengths of spatial heterogeneity.

5.3.5 Correlations with β-relations and spatial heterogeneity

We have shown the strong correlations between the spatial heterogeneity and mechanical behaviors in the metallic glasses. The spatial heterogeneity might act as the grain size in polycrystalline metals for metallic glasses, but what was its “dislocation”? For the last ten years, more and more experimental results have supported JG relaxation as the origin of deformation in metallic glasses [32-34]. The stress-strain response in a metallic glass-forming liquid attributed the reversible anelastic deformation to the configurational hopping by β-relaxation [33]. Moreover, a La-based metallic glass possessing strong JG relaxation was reported to show a pronounced macroscopic tensile plasticity [34]. The most convincing evidence comes from the systematic analysis on the potential-energy barriers of STZs and the activation energy of JG relaxation, unveiling equivalence between them over various kinds of metallic glasses [35]. On the other hand, a relationship between the structure evolution and β-relaxation in metallic glass has been unveiled by the stress relaxation spectra showing changes of distribution coefficient at different temperatures [28]. In chapter 3 we also evidenced that the enthalpy relaxation of the metallic glass below 553 K was mainly processed by the β-relaxation. Thus the correlations of structure-property in the metallic glass were supposed to be originated from the β-relaxation.

For the β-relaxation itself, G. P. Johari has envisaged some local regions with loose atomic packing in order to explain the existence of JG relaxation process in the mechanically rigid glasses, especially for metallic glasses [36]. In the scheme, β-relaxation is the short-range translational motions of atoms confined to isolated local

regions with loose packing. The theory of STZs assumed the pre-existence of some loosely packed clusters easy for the initiation of deformation embedded in the densely packed matrix. The scheme for β-relaxation shares some common features with the STZs. This might explain why β-relaxation could account for the mechanical behaviors of metallic glasses. And as the β-relaxation is a precursor to the primary α-relaxation, it can also explain why the yield strength is T_g-dependent in metallic glasses [37]. Interestingly, the STZs and local regions of JG relaxation have been evaluated to be several nanometers which are comparable to the nanoscale spatail heterogeneity [20, 38]. Obviously, the viscous region with a larger size can more easily facilitate the flow in metallic glass to an external stress as manifested by the as-deposited sample. After sub-T_g enthalpy relaxation, these viscous regions shrink into smaller sizes which deteriorate the deformability and rheology of the metallic glass, and the metallic glasses become harder and stronger. The structure-property correlations are established for the metallic glasses based on the spatially heterogeneous dynamics of atomic motions.

5.4 Summary

In summary, the effects of β-relaxation on mechanical properties and creep behaviours of metallic glass were investigated. After sub-T_g relaxation, the metallic glass became harder, less deformable and its rheology was slower. The activation energy for the creep had a value close to the β-relaxation, indicating that the β-relaxation might act as a dynamic origin for the the rheology in metallic glass far below T_g. Also, we found strong correlations of hardness and creep with the nanoscale spatial heterogeneity in the

metallic glass. Our experimental results and conclusions reveal an underlying dynamic origin for the mechanical properties of metallic glasses and provide fingerprints for them which can help establish the structure-property in metallic glasses.

References

[1] A. L. Greer, Science 267, 1947 (1995).

[2] W. L. Johnson, MRS bull. 24, 42 (1999).

[3] C. A. Schuh, T. C. Hufnagel, and U. Ramamurty, Acta Mater. 55, 4067 (2007).

[4] M. W. Chen, Annu. Rev. Mater. Res. 38, 445 (2008).

[5] Y. Q. Cheng, and E. Ma, Prog. Mater. Sci. 56, 379 (2011).

[6] W. H. Wang, Prog. Mater. Sci. 57, 487 (2012).

[7] F. Spaepen, Acta Metall. 25, 407 (1977).

[8] A. S. Argon, Acta Metall. 27, 47 (1979).

[9] W. L. Johnson, and K. Samwer, Phys. Rev. Lett. 95, 195501 (2005).

[10] M. W. Chen, A. Inoue, W. Zhang, and T. Sakurai, Phys. Rev. Lett. 96, 245502 (2006).

[11] A. L. Greer, Y. Q. Cheng, and E. Ma, Mater. Sci. Eng. R-Rep. 74, 71 (2013).

[12] A. Hirata, L. J. Kang, T. Fujita, B. Klumov, K. Matsue, M. Kotani, A. R. Yavari and M. W. Chen, Science 341, 376 (2013)

[13] S. X. Song. J. S. C. Jang and T. G. Nieh, Intermetallics 16, 676 (2008).

[14] A. Concustell, J. Sort, A. L. Greer and M. D. Baro, Appl. Phys. Lett. 88, 171911 (2006).

[15] A. Castellero, B. Moser, D. I. Uhlenhaut, F. H. Dalla Torre and J. F. Loffler, Acta Mater. 56, 3777 (2008).

[16] Y. Yang, J. F. Zeng, J. C. Ye and J Lu, Appl. Phys. Lett. 97, 261905 (2010).

[17] Y. H. Chen, J. C. Huang, L. Wang and T. G. Nieh, Intermetallics 41, 58 (2013).

[18] D. Pan, A. Inoue, T. Sakurai, and M. W. Chen, Proc. Natl. Acad. Sci. U.S.A. 105, 14769 (2008).

[19] J. Ding, S. Patinet, M. L. Falk, Y. Cheng, and E. Ma, Proc. Natl. Acad. Sci. U.S.A. 111, 14052 (2014).

[20] Y. H. Liu, D. Wang, K. Nakajima, W. Zhang, A. Hirata, T. Nishi, A. Inoue and M. W. Chen, Phys. Rev. Lett. 106, 125504 (2011).

[21] P. G. Debenedetti, and F. H. Stillinger, Nature 410, 259 (2001).

[22] G. P. Johari, and M. Goldstein, J. Chem. Phys. 53, 2372 (1970).

[23] K. L. Ngai, M. Paluch, J. Chem. Phys. 120, 857 (2004).

[24] H. B. Yu, K. Samwer, W. H. Wang and H. Y. Bai, Nature Commun. 4, 2204 (2013).

[25] H. B. Yu, W. H. Wang, K. Samwer, Mater. Today 16, 183 (2013).

[26] H. B. Yu, W. H. Wang, H. Y. Bai, and K. Samwer, *Natl. Sci. Rev.* 1, 429-461 (2014).

[27] W. C. Oliver, and G. M. Pharr, J. Mater. Res. 7, 1564 (1992).

[28] Z. Wang, B. A. Sun, H. Y. Bai and W. H. Wang, Nature Commun. 5, 5823 (2014).

[29] P. Murali, and U. Ramamurty, Acta Mater. 53, 1467 (2005).

[30] H. S. Chou, J. C. Huang, L. W. Chang and T. G. Nieh, Appl. Phys. Lett. 93, 191901 (2008).

[31] W. H. Poisl, W.C. Oliver, and B. D. Fabes , J. Mater. Res. 10, 2024 (1995).

[32] W. H. Wang, J. Appl. Phys. 110, 053521 (2011).

[33] J. S. Harmon, M. D. Demetriou, W. L. Johnson, and K. Samwer, Phys. Rev. Lett. 99, 135502 (2007)

[34] H. B. Yu, X. Shen, Z. Wang, L. Gu, and W. H. Wang, Phys. Rev. Lett. 108, 015504 (2012).

[35] H. B. Yu, W. H. Wang, H. Y. Bai, Y. Wu and M. W. Chen, Phys. Rev. B 81, 220201 (2010).

[36] G. P. Johari, J. Non-crystal. Solids. 307, 317 (2002).

[37] Y. H. Liu, C. T. Liu, W. H. Wang, A. Inoue, T. Sakurai, and M. W. Chen, Phys. Rev. Lett. 103, 065504 (2009).

[38] M. D. Ediger, Annu. Rev. Phys. Chem. 51, 99 (2000).

Chapter 6

TEM Observations of Spatial Heterogeneity

6.1 Introduction

The spatial heterogeneity has long been proposed to explain the slowing down of dynamics around T_g in glass-formers [1, 2], the secondary relaxations or β-relaxations in glasses [3, 4] and the shear transformation zones (STZs) for the deformation of metallic glasses [5-8]. This scheme can definitely provide a useful structure model to predict various properties of metallic glasses [9-12]. However, to directly observe and quantitatively evaluate the spatial heterogeneity in metallic glasses are still challenging due to the amorphous structures of glasses and the lack of efficient characterization tools [13-16]. Recently, the atomic force acoustic microscopy (AFAM) [17] and amplitude-modulation dynamic atomic force microscopy (AM-AFM) [18] have been utilized to measure them by distinguishing the elastic or viscoelastic heterogeneity in metallic glass. However, such measurements don't become popular as they need special equipments and are limited to several certain kinds of metallic glasses due to the resolution of AFM around 1 nm.

Among the commonly used structural characterization tools, transmission electron microscopy (TEM) is the most powerful one to determine the atomic structures of metallic glasses [15, 16, 19]. However, it is still in controversy whether the spatial heterogeneity can be directly observed in metallic glasses by TEM or not. B. B. Sun *et*

al. have attributed the features they observed in metallic glasses by STEM to the artifacts induced by the TEM sample preparations, such as the contamination, the crystallization and the oxidation [20]. With the “proper” preparation conditions, the metallic glass became featureless under both TEM and STEM. T. Miyauchi *et al.* also observed some nanoscale particles enriched with solid Ar in a Pd-base metallic glass by STEM [21]. After annealing around T_g, the particles became smaller and the contrast was weaker. They declared that the pre-existing low-density regions or free-volume entities help the precipitation of solid Ar in metallic glasses, that the particles in STEM images were manifestations of the intrinsic heterogeneity of metallic glasses.

In this work, we demonstrate that the spatial heterogeneity in metallic glasses can be observed by high-angle annular dark field scanning transmission electron microscopy (HAADF-STEM) using a Cs-corrected TEM. The effect of sub-T_g relaxation on heterogeneity of the hyper-quenched metallic glass in STEM images was in well accordance with the results measured by AM-AFM which we showed in Chapter 4. The spatial heterogeneities were systematically investigated in several representative systems including Zr-base, Pt-base and La-base metallic glasses. The spatial heterogeneities were found to have close correlations with the fragility and the intensity of β-relaxations of metallic glasses. The ABED was performed to investigate the evolution of atomic packing during the sub-T_g relaxation. This work provided a useful and universal method to characterize the spatial heterogeneities in metallic glasses which can help in reveal the structural origins of fragility, β-relaxations and other properties of metallic glasses.

6.2 Experimental

Sample preparation. The hyper-quenched metallic glass with a composition of $Zr_{53}Cu_{36}Al_{11}$ (at. %) was prepared by RF magnetron sputtering. The ribbon samples including $La_{50}Ni_{20}Al_{30}$, $La_{55}Al_{25}Cu_{10}Ni_5Co_5$, $Pd_{40}Ni_{40}P_{20}$, $Pd_{40}Cu_{30}Ni_{10}P_{20}$, $Zr_{55}Cu_{30}Ni_5Al_{10}$, $Zr_{50}Cu_{40}Al_{10}$, $Zr_{66.7}Al_{23.3}Ni_{10}$ $Cu_{50}Zr_{50}$ and $(Cu_{50}Zr_{50})_{95}Al_5$ (at. %) were prepared by spin casting.

TEM sample preparation. The TEM samples of the hyper-quenched metallic glasses were prepared both by ion milling and by twin-jet electrolyte polishing. The thick as-spun ribbon samples were thinned by the twin-jet electrolyte polishing.

Sub-T_g relaxation. The hyper-quenched metallic glasses were annealed at 553 K for 5 min and 720 min protected by the flowing Ar.

TEM observations. The hyper-quenched sample, the relaxed samples and the as-spun ribbons were checked by TEM, HRTEM, STEM and EDS. The hyper-quenched sample and the sample relaxed at 553 K for 720 min were checked by ABED.

6.3 Results and Discussion

6.3.1 Hyper-quenched metallic glass

Fig. 6.1 showed the TEM images for the hyper-quenched metallic glass prepared by ion milling. In the HRTEM images (**Fig. 6.1a** and **b**), typical maze-like contrast and diffraction halo for the amorphous materials can be observed. However, in the HAADF (**Fig. 6.1c** and **d**) and BF (**Fig. 6.1e** and **f**) images, clear spherical heterogeneities with

sizes around 5-7 nm can be observed. The STEM-EDS mapping (**Fig. 6.2**) indicated that these heterogeneities had no correlation with the chemical distributions of Zr, Cu, Al or O, but strongly correlated with the Ar element. The precipitation of Ar in ion-milled TEM samples has been reported by T. Miyauchi *et al.* [21] and they declared that the Ar precipitation came from the free volumes preexisted in metallic glasses.

In order to check if these heterogeneities were intrinsic or not, we prepared a TEM sample of hyper-quenched metallic glass by twin-jet electro-polishing. The TEM images of the electro-polished sample were shown in **Fig. 6.3**. The HRTEM images (**Fig. 6.3a** and **b**) again confirmed the glassy nature of hyper-quenched metallic glass. Although prepared without the bombardment of Ar ions, the clear heterogeneity can still be observed in both the HAADF (**Fig. 6.3c** and **d**) and BF (**Fig. 6.3e** and **f**) images. The STEM-EDS mapping for the electro-polished sample showed that little Ar can be detected and no correlation between the heterogeneity and special elements can be observed. The electron energy loss spectroscopy (EELS) zero-loss peak was performed to check the heterogeneity in the STEM images (**Fig. 6.4**). Interestingly, the relative thickness or density map derived from the EELS zero-loss map was well in accordance with the contrast in HAADF images, indicating that the observed heterogeneity might came from the density or thickness variations rather than the chemical distribution. As these samples were prepared either by ion-milling or by electro-polishing, the thickness variations induced by artifacts could be excluded. So the density or thickness variations should be intrinsic for the hyper-quenched metallic glasses. Such density fluctuation has been predicted by G. P. Johari to explain the β-relaxation in rigid glasses [3].

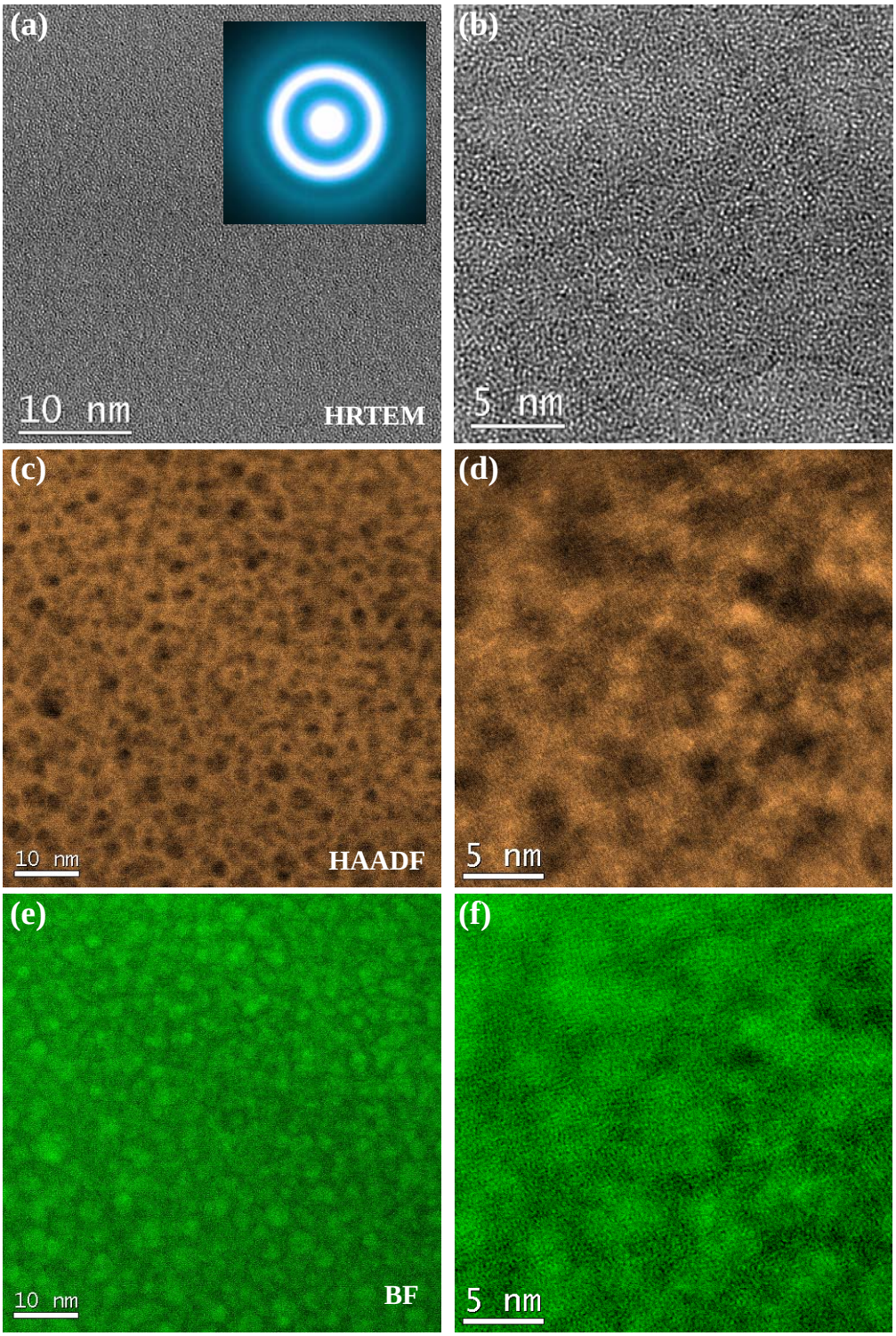

Fig. 6.1. TEM images of hyper-quenched metallic glass thinned by ion-milling. (a), (b) High resolution TEM images. (c), (d) HAADF-STEM images. (e), (f) BF-STEM images. Inset in (a) are the corresponding selected area electron diffraction. Note that images (c) and (e) are taken simultaneously in one area, so are images (d) and (f).

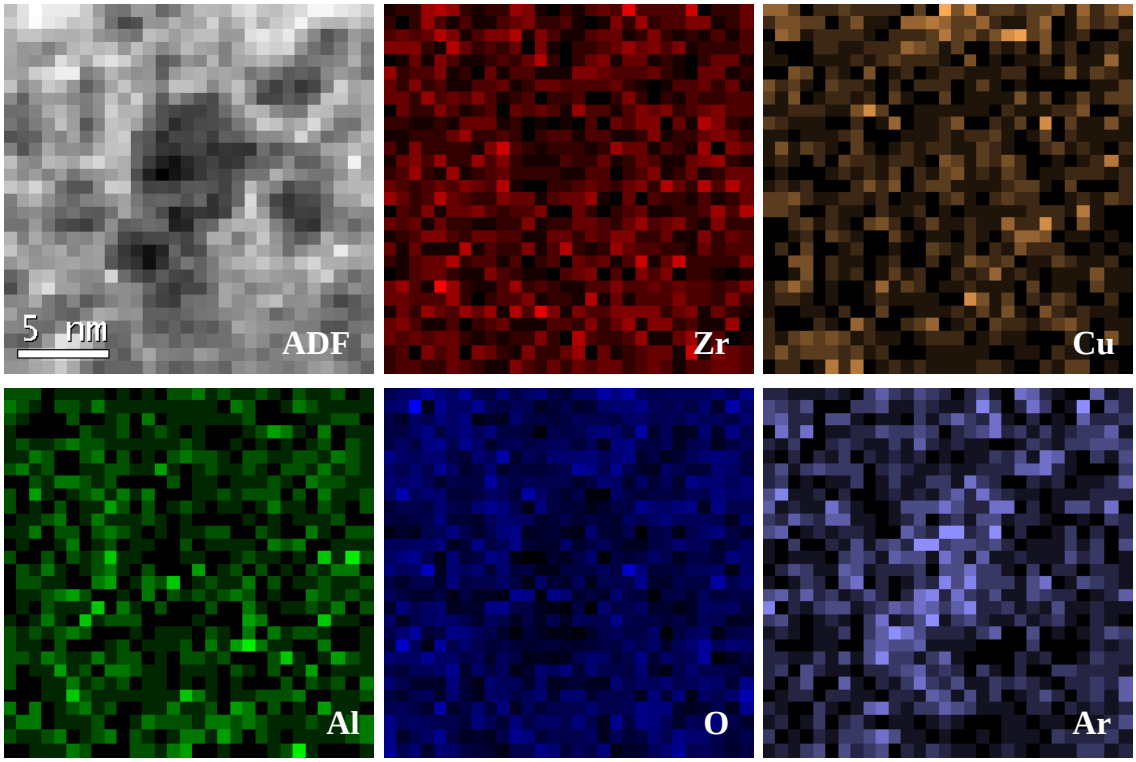

Figure 6.2. STEM-EDS mapping for the hyper-quenched metallic glass thinned by ion milling. We see clear Ar precipitation related to the contrast in ADF images.

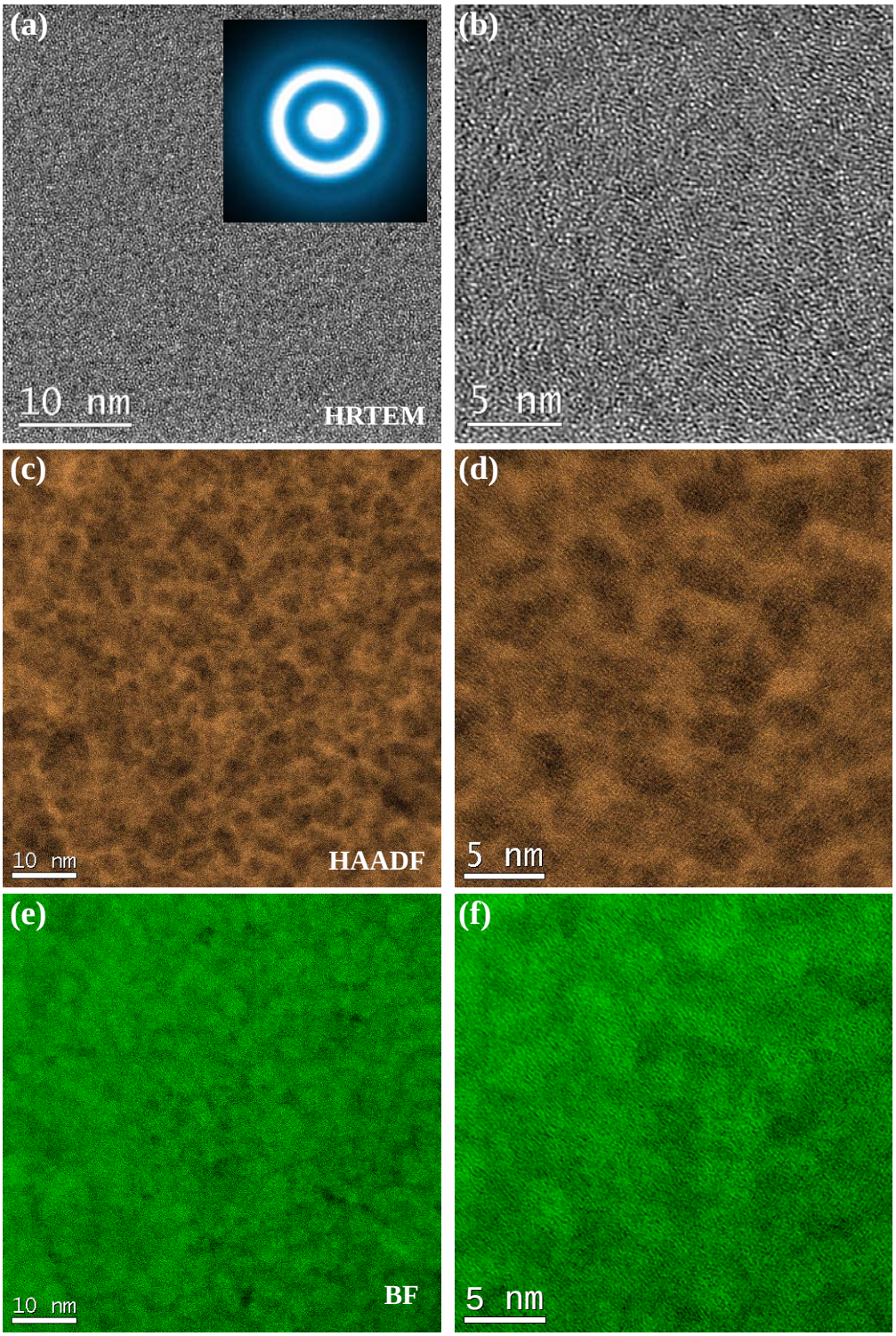

Figure 6.3. TEM images of hyper-quenched metallic glass thinned by twin jet electro-polishing. (a), (b) High resolution TEM images. (c), (d) HAADF-STEM images. (e), (f) BF-STEM images. Inset in (a) are the corresponding selected area electron diffraction. (c) and (e) are taken simultaneously in one area, so are (d) and (f).

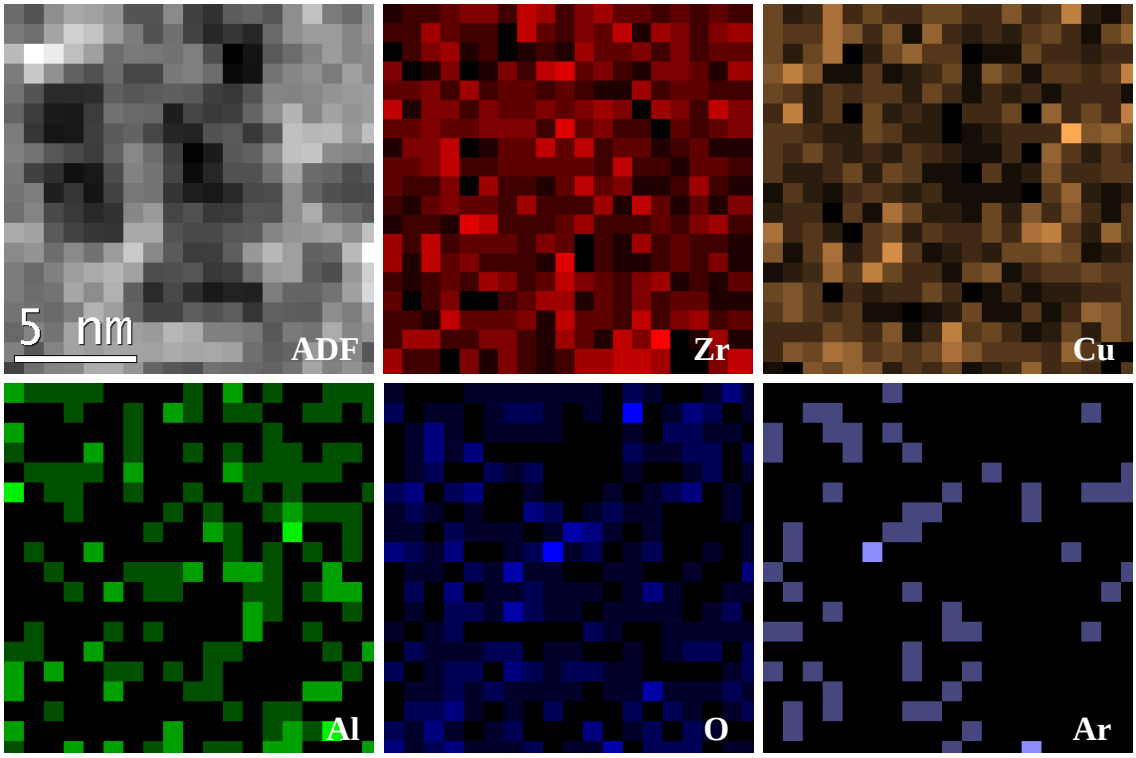

Figure 6.4. STEM-EDS mapping for the hyper-quenched metallic glass thinned by twin jet elecctro-polishing. Little Ar can be detected by the EDS and no correlation with the contrast in ADF image.

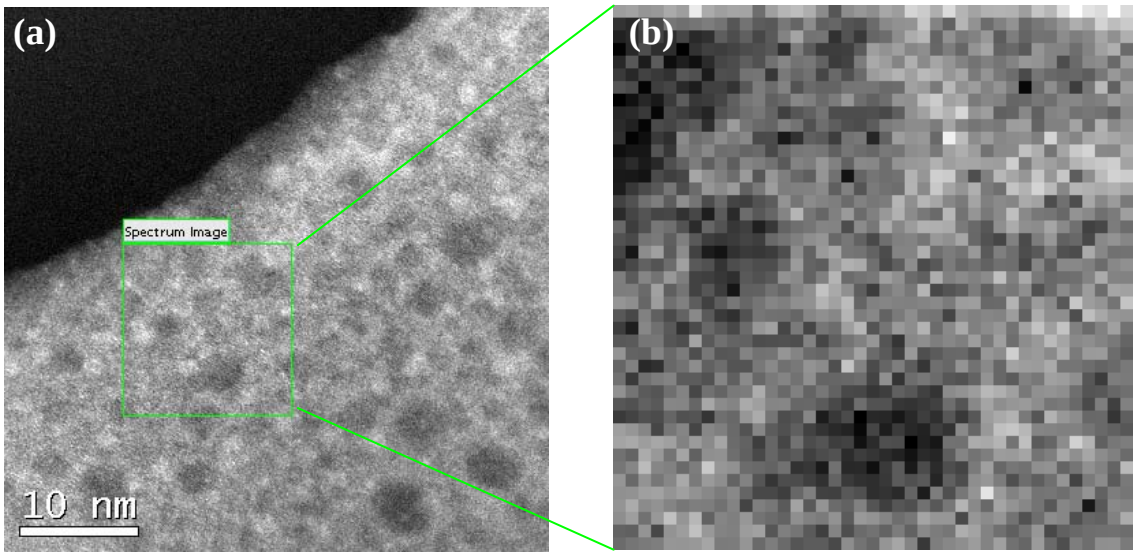

Figure 6.5. (a) STEM-HAADF image. (b) Relative density or thickness map derived from the EELS zero-loss peak map, showing that the contrast in STEM image is related to the density or thickness variations.

6.3.2 Effects of sub-T_g relaxation

If the heterogeneities observed in the STEM images (**Fig. 6.1** and **6.3**) were intrinsic, the size of these heterogeneities should be correlated with the energy state of the metallic glass. The hyper-quenched metallic glasses were relaxed at 553 K for 5 min and 720 min in order to get structures at different energy states. **Fig. 6.6** showed the HAADF and BF images for the hyper-quenched metallic glasses after the sub-T_g relaxation for 5 min. After annealing for 5 min, the heterogeneity decreased to around 4 to 5 nm and the contrast became weaker. With the longer annealing for 720 min, the heterogeneity in the most relaxed sample decreased to less than 3 nm. The sub-T_g relaxation can lead to the shrinkage of the heterogeneities in STEM (**Fig. 6.7**).

We also observed the similar shrinkage of spatial heterogeneity using the AM-AFM in chapter 4. Thus we compared the heterogeneity observed in STEM with those measured by AM-AFM (**Fig. 6.8**). Interestingly, the sizes observed in the HAADF images were in well accord with the values for the heterogeneities measured using the AM-AFM. For the hyper-quenched metallic glass, the size in STEM is from 5 to 7 nm, while the mean value measured by AM-AFM was around 6.1 nm. After the sub-T_g relaxation for 5 min and 720 min, the sizes decreased to 4-5 nm and 2-3 for the STEM, and ~5.05 and ~2.59 nm for the AM-AFM, respectively. We also observed the equivalences between STEM and AFM results for the La-Ni-Al as-spun ribbon before and after annealing (**Fig. 6.9** and **6.10**). The well equivalences between STEM and AFM results indicated that the heterogeneity observed in STEM were the spatial heterogeneity correlated with β-relaxation as demonstrated in chapter 4

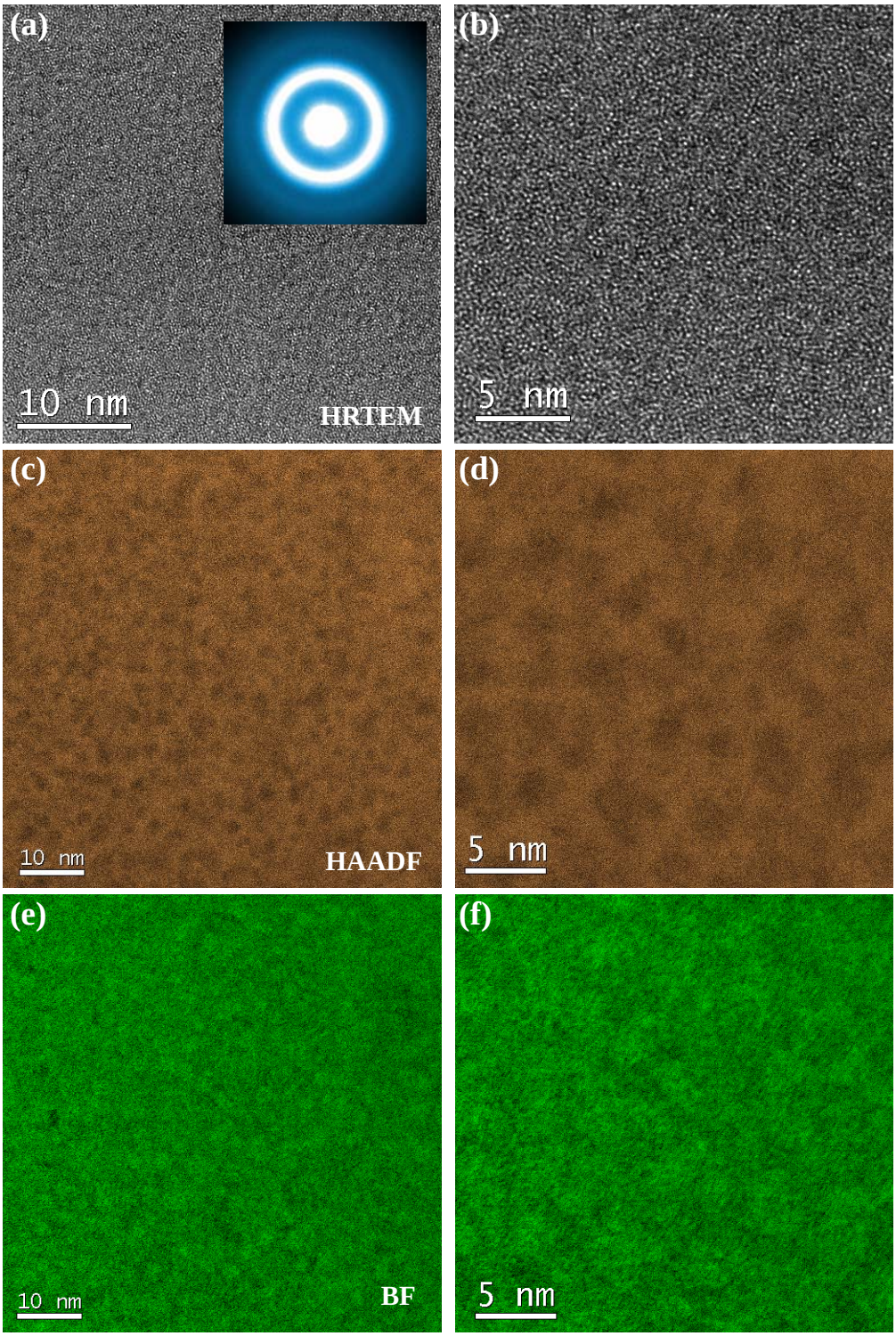

Figure 6.6. TEM images of hyper-quenched metallic glass after annealing at 553 K for 5 min. (a), (b) High resolution TEM images. (c), (d) HAADF-STEM images. (e), (f) BF-STEM images. Inset in (a) are the corresponding selected area electron diffraction. (c) and (e) are taken simultaneously in one area, so are (d) and (f).

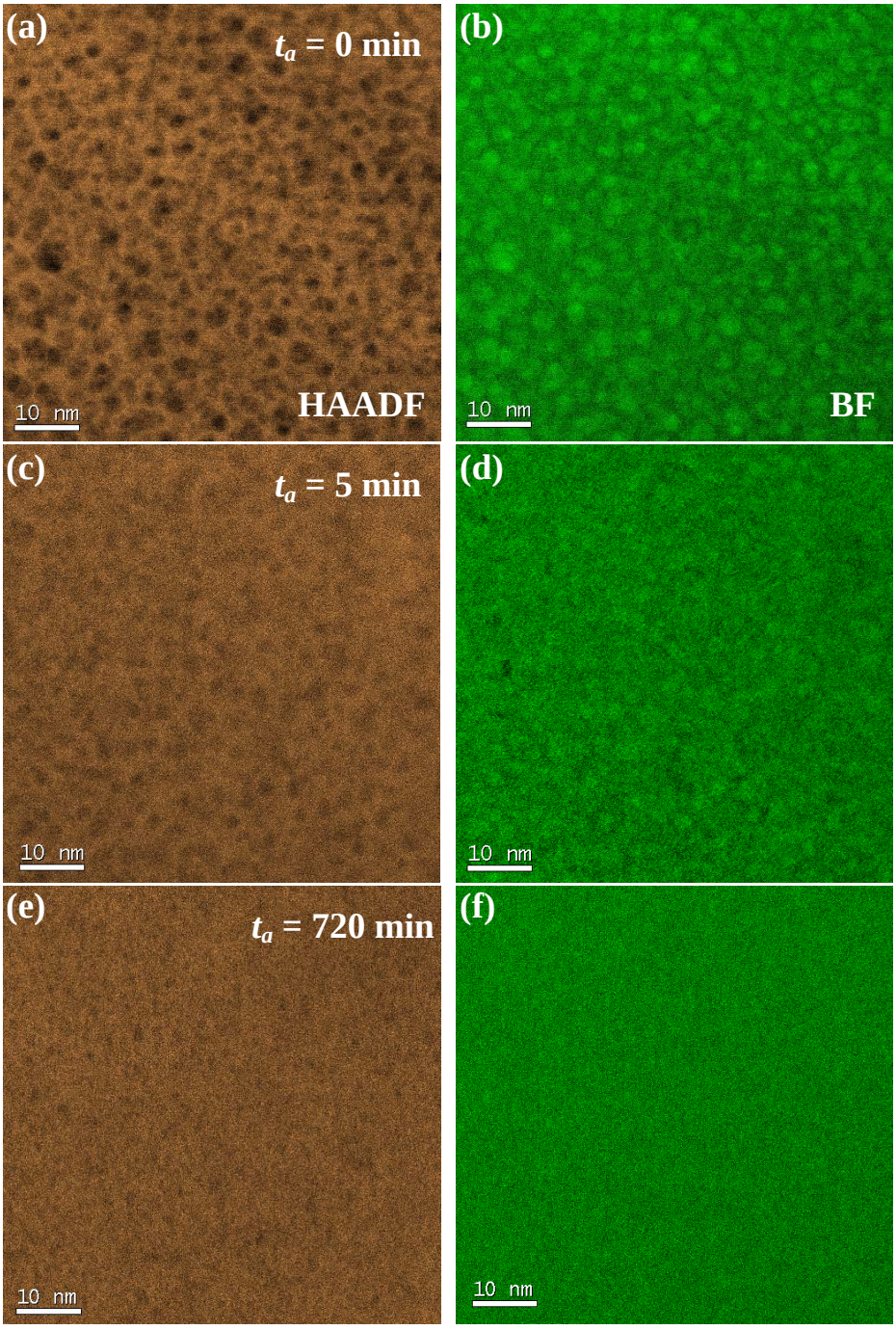

Figure 6.7. Effects of sub-T_g relaxation on the spatial heterogeneity observed in STEM images. (a), (b) HAADF and BF images for the hyper-quenched metallic glass. HAADF and BF images for the hyper-quenched metallic glass after relaxation at 553 K for (c), (d) 5 min and (e), (f) 720 min.

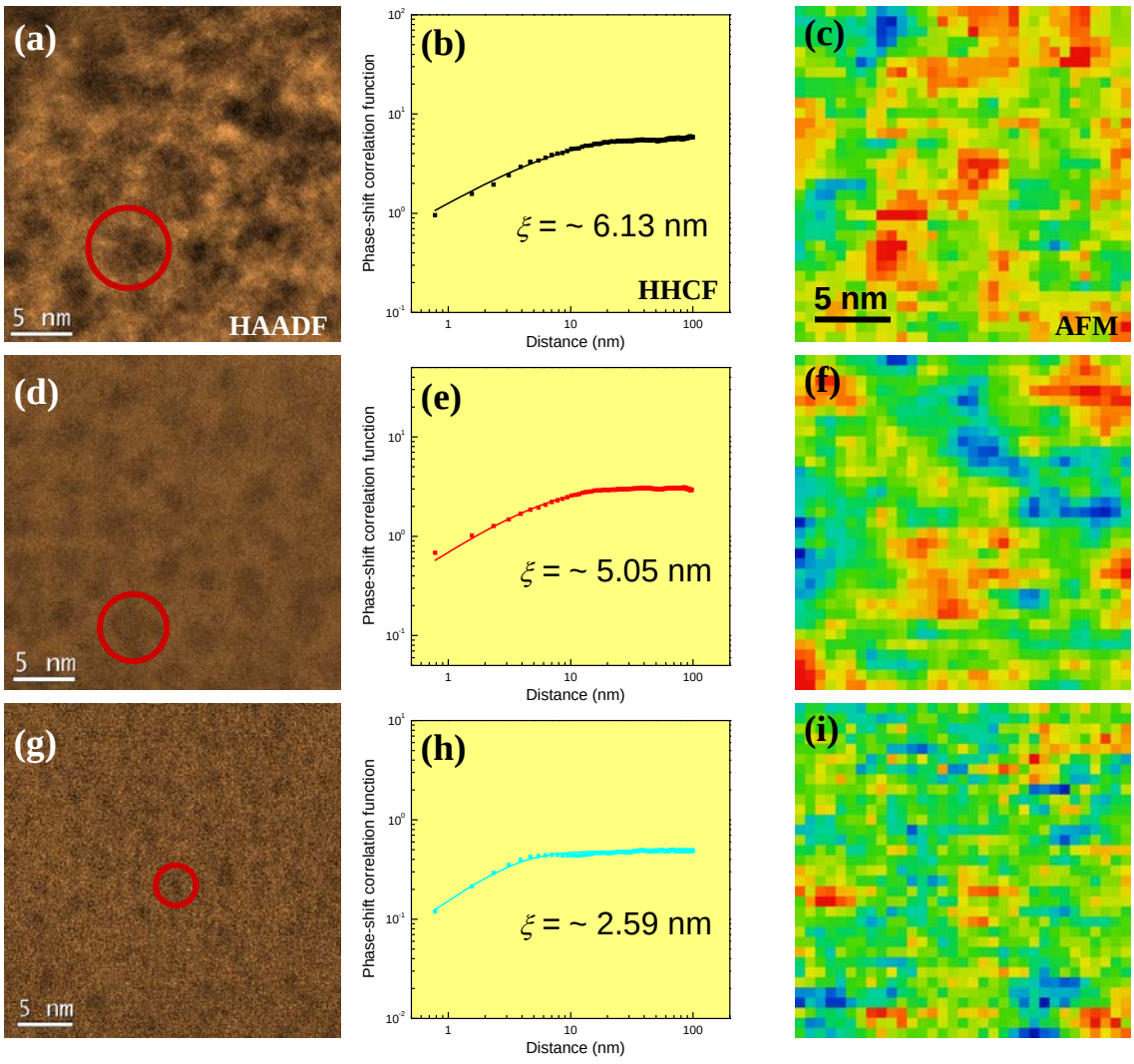

Figure 6.8. Comparison between spatial heterogeneities in STEM-HAADF and AFM images. (a) STEM-HAADF image, (b) HHCF derived from AFM image and (c) AFM image for the hyper-quenched metallic glass. Results for metallic glass after relaxation at 553 K were presented in (d), (e), (f) for t_a = 5 min and (g), (h), (i) for t_a = 720 min.

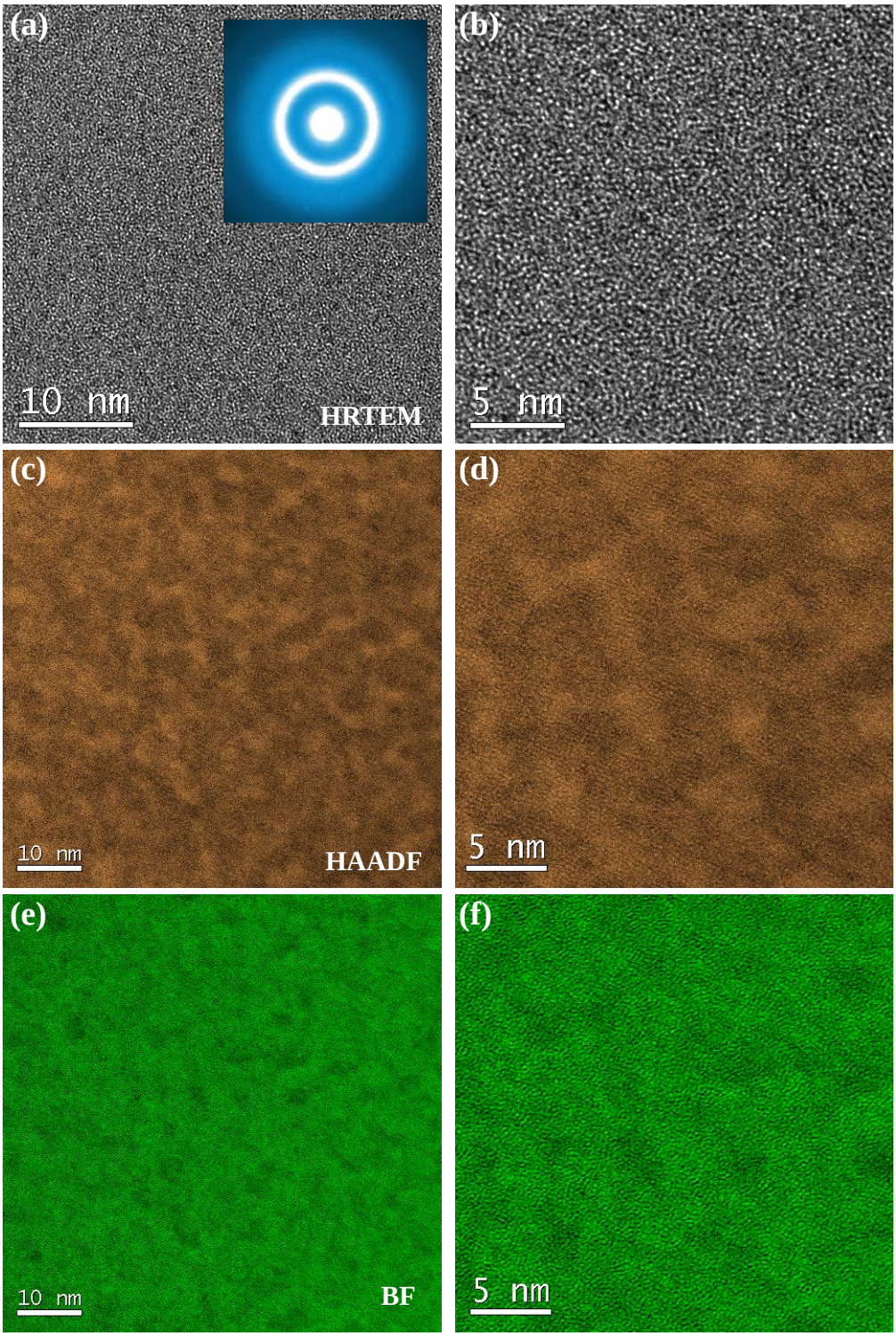

Figure 6.9. TEM images of $La_{50}Ni_{20}Al_{30}$ as-spun ribbon MG. (a), (b) High resolution TEM images. (c), (d) HAADF-STEM images. (e), (f) BF-STEM images. Inset in (a) is the corresponding selected area electron diffraction (SAED). Note that images (c) and (e) are taken simultaneously in one area, so are images (d) and (f).

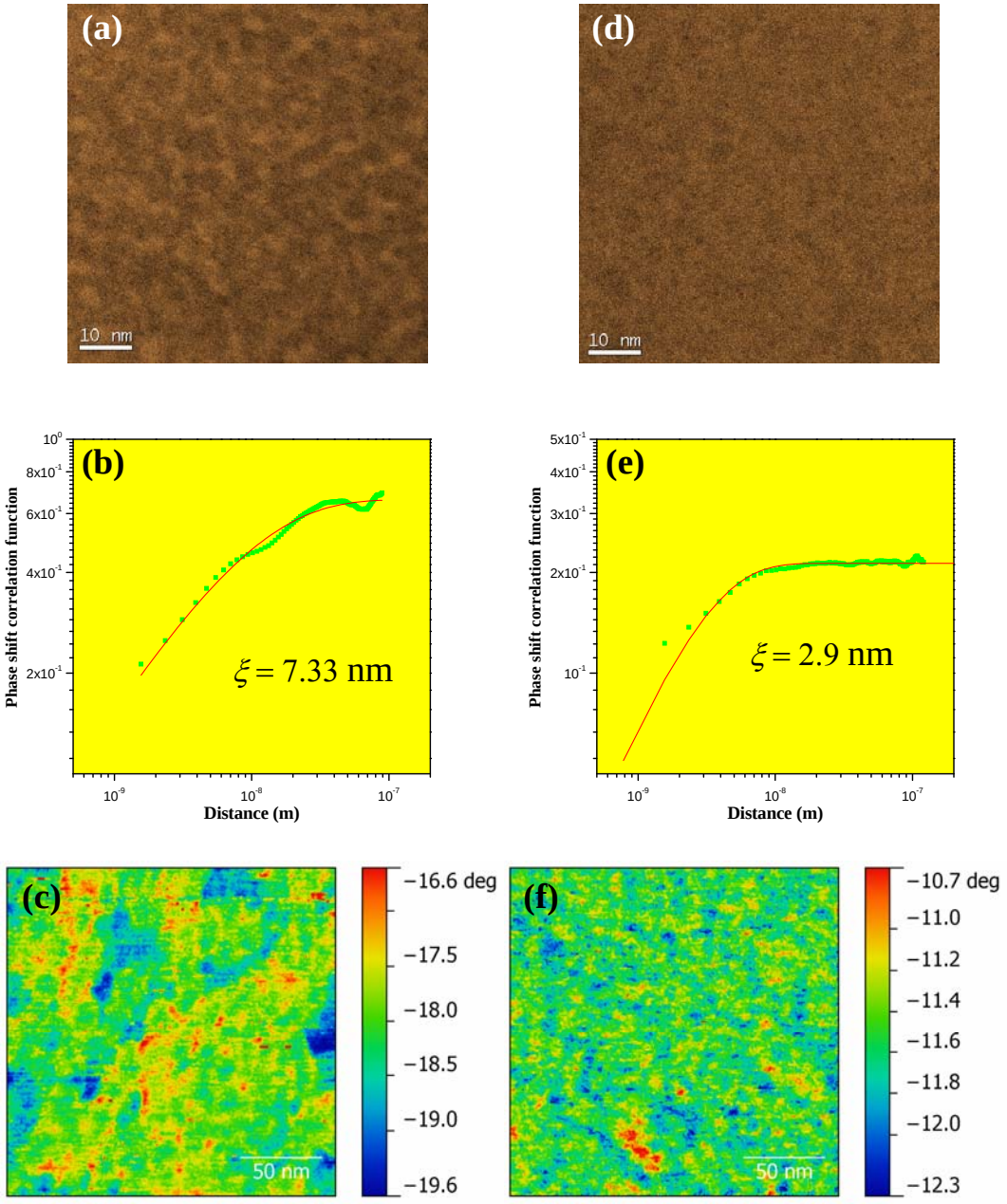

Figure 6.10. Comparison between spatial heterogeneities in STEM-HAADF and AFM images for $La_{50}Ni_{20}Al_{30}$ as-spun metallic glass. (a) STEM-HAADF image, (b) AFM image and (c) HHCF derived from AFM image for as-spun ribbon. (d), (e), (f) Results for the sample after annealing at 533 K.

6.3.3 Correlations with fragility

According to the classification proposed by C. A. Angell [22-24], the Zr-Cu-Al and La-Ni-Al metallic glasses can be classified as intermediate or strong metallic glasses. The fragility values were believed to be related to the intrinsic structures of glass-forming liquids [25]. For the strong glass-forming liquids, their structures are stable as the temperature goes down to T_g. For the fragile glass-forming liquids, their structures are sensitive to the temperature variation and change abruptly approaching T_g. Thus, it is interesting to see the spatial heterogeneity in fragile metallic glasses. The $Pd_{40}Cu_{30}Ni_{10}P_{20}$ and $Cu_{50}Zr_{50}$ metallic glasses are two representative fragile metallic glasses whose thermodynamic fragility values m_t are around 52 and 62, respectively [25]. The TEM images of the $Pd_{40}Cu_{30}Ni_{10}P_{20}$ and $Cu_{50}Zr_{50}$ metallic glass were shown in **Fig. 6.11** and **Fig.6.12**, respectively. For comparison, we also show the TEM images of three strong or intermediate metallic glasses: $La_{55}Al_{25}Cu_{10}Ni_5Co_5$ (m_t = 28) in **Fig. 6.13,** $Zr_{55}Cu_{30}Ni_5Al_{10}$ (m_t = 35) in **Fig. 6.14** and $Pd_{40}Ni_{40}P_{20}$ (m_t = 41) in **Fig. 6.15**. The STEM images of Pd-Cu-Ni-P metallic glass showed a uniform distribution of particle-like heterogeneity with a size around 3-4 nm (**Fig. 6.11c**, **d**, **e** and **f**). However, the structural feature in the fragile metallic glass was much different from what we observed in the strong or intermediate metallic glasses (**Fig. 6.1**, **6.3**, **6.9, 6.13, 6.14** and **6.15**). As we have proven using the EELS zero-loss map, the dark contrast in the HAADF images corresponded to low-density or weak regions. In the strong metallic glass, the weak regions played as spatial heterogeneity embedded in the matrix of strong regions, while in Pd-Cu-Ni-P metallic glass the weak regions became the matrix

that the strong regions were surrounded by the weak regions. The similar feature can also be observed in the fragile $Cu_{50}Zr_{50}$ metallic glass where the strong regions are rod-like and the relative volume of the strong regions to the weak regions became lower compared with that in $Pd_{40}Cu_{30}Ni_{10}P_{20}$.

We presented the HAADF images of five representative metallic glasses from the strongest to the most fragile: 28 for $La_{55}Al_{25}Cu_{10}Ni_5Co_5$, 35 for $Zr_{55}Cu_{30}Ni_5Al_{10}$, 48 for $La_{50}Ni_{20}Al_{30}$, 52 for $Pd_{40}Cu_{30}Ni_{10}P_{20}$ and 62 for $Cu_{50}Zr_{50}$ (**Fig. 6.16**) [26, 27]. The weak regions evolved from the minority in the strongest metallic glass to the majority in the most fragile metallic glass, indicating that the fragility of metallic glass was strongly correlated with the geometry of spatial heterogeneity. Recently, the fragile-to-strong transitions have been observed in La-base [28], Cu-Base [29-31], Zr-base [32, 33] and other metallic glasses or glass-forming liquids. The observation of fragile-to-strong transition in the strong Zr-base metallic glasses implied that the liquid-liquid transition in metallic glass-forming liquids was universal. Thus, we propose a model as shown in **Fig. 6.17** to explain the origin of fragility of metallic glasses. For the fragile glass-forming liquids, the liquid is uniform at a temperature far above T_g. As the temperature goes down, a liquid with denser structure appears and gradually grows up. This process continues for the strong glass-forming liquids that the denser liquid will eventually occupy the most part of the space and become the matrix. The original liquid will vanish as the temperature approaching T_g. During the transition, the structural reorganization occurs in the fragile metallic glasses, and minor variation of structure in the strong metallic glasses which is in accord with Angell's plot [25].

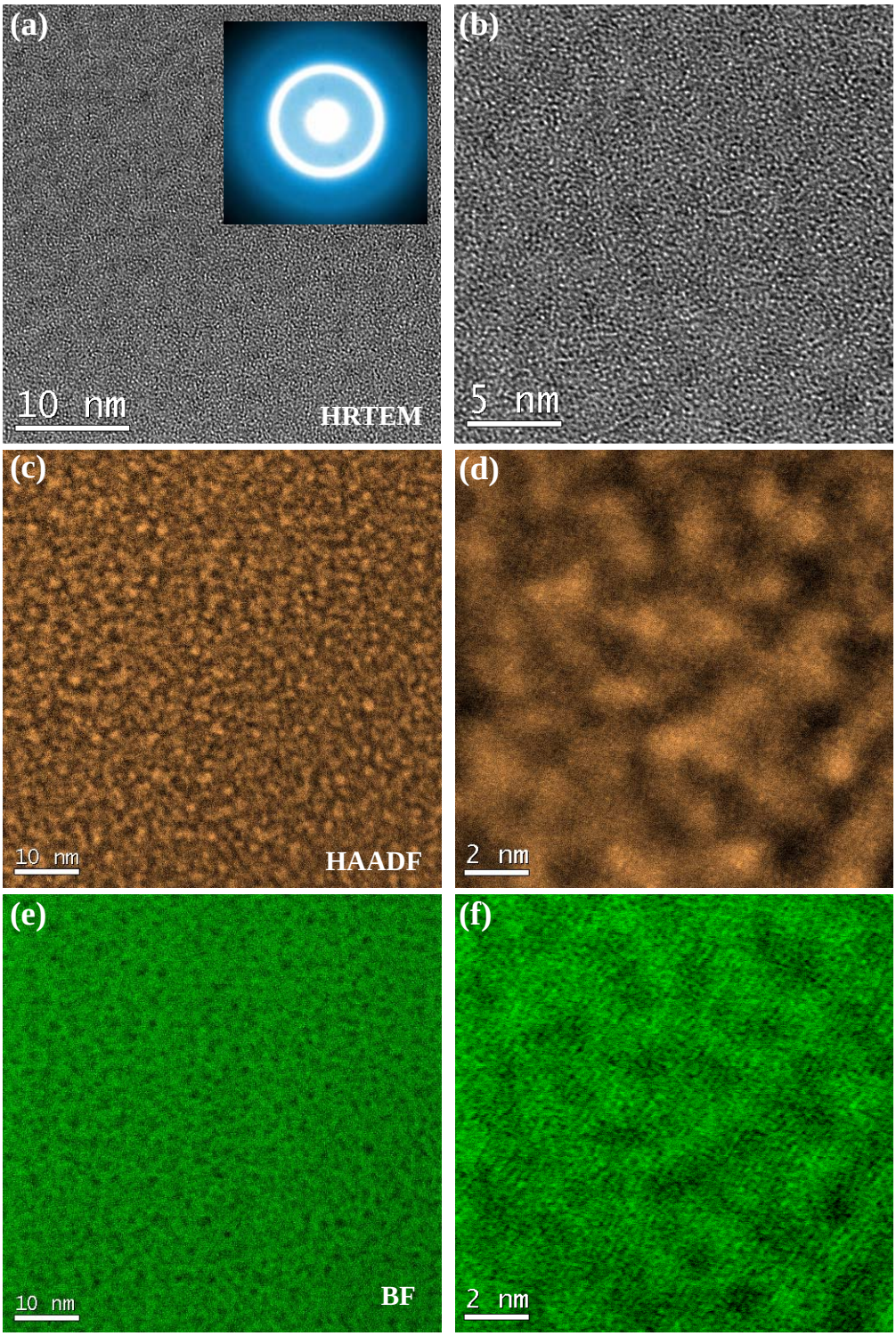

Figure 6.11. TEM images of fragile $Pd_{40}Cu_{30}Ni_{10}P_{20}$ as-spun ribbon MG. (a), (b) High resolution TEM images. (c), (d) HAADF-STEM images. (e), (f) BF-STEM images. Inset in (a) is the corresponding selected area electron diffraction (SAED). Note that images (c) and (e) are taken simultaneously in one area, so are images (d) and (f).

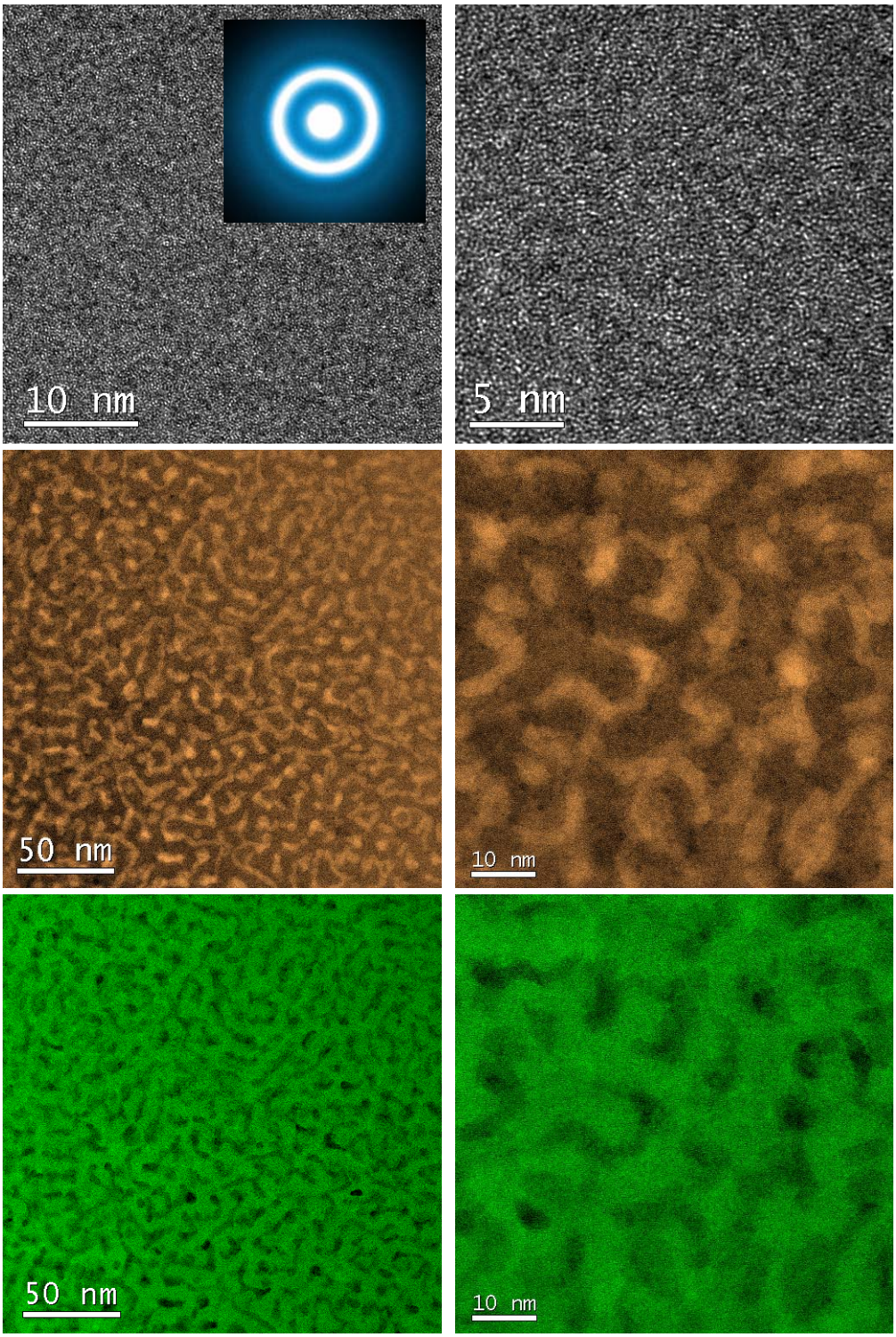

Figure 6.12. TEM images of fragile $Cu_{50}Zr_{50}$ as-spun ribbon MG. (a), (b) High resolution TEM images. (c), (d) HAADF-STEM images. (e), (f) BF-STEM images. Inset in (a) is the corresponding selected area electron diffraction (SAED). Note that images (c) and (e) are taken simultaneously in one area, so are images (d) and (f).

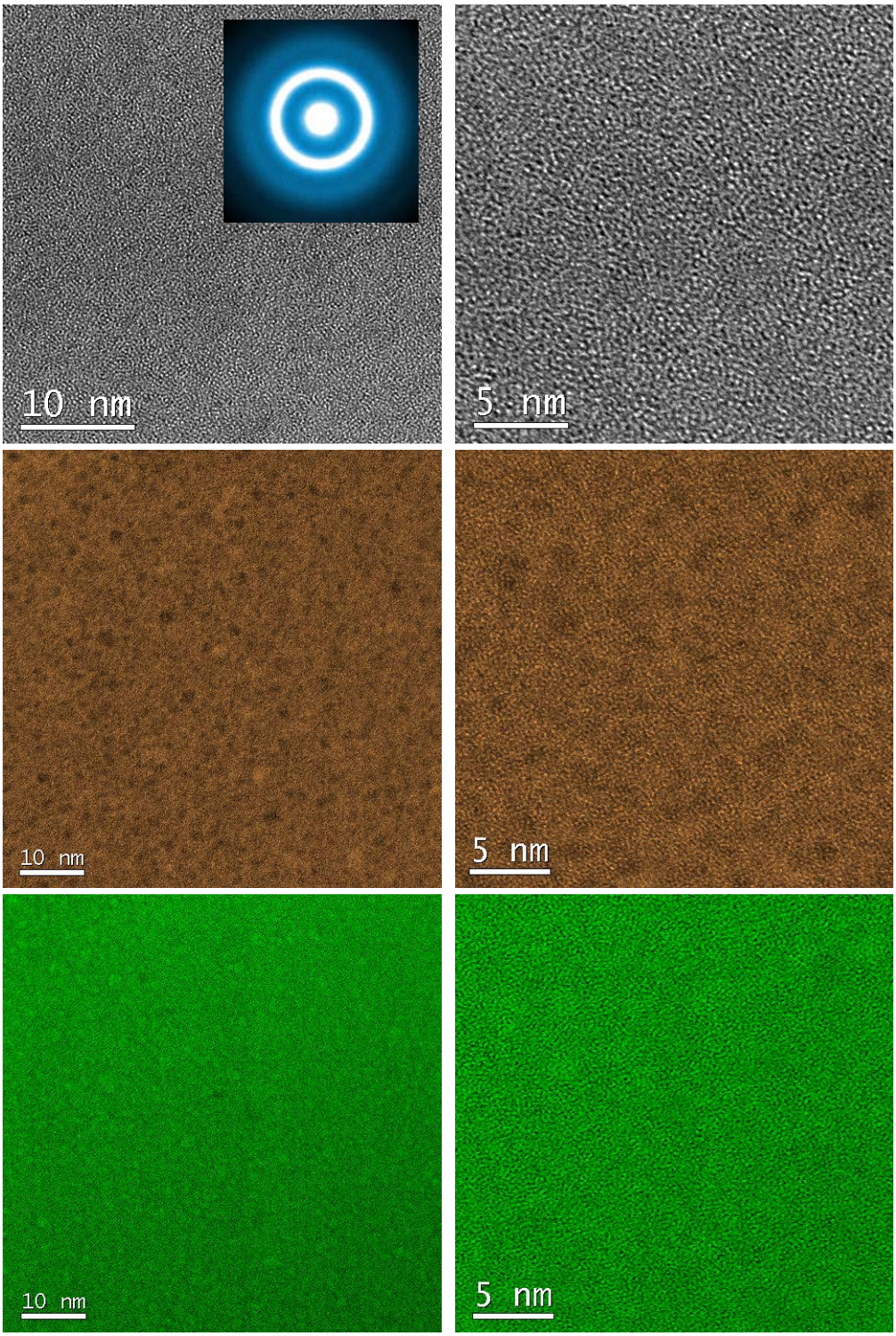

Figure 6.13. TEM images of $La_{55}Al_{25}Cu_{10}Ni_5Co_5$ as-spun ribbon MG. (a), (b) High resolution TEM images. (c), (d) HAADF-STEM images. (e), (f) BF-STEM images. Inset in (a) is the corresponding selected area electron diffraction (SAED). Note that images (c) and (e) are taken simultaneously in one area, so are images (d) and (f).

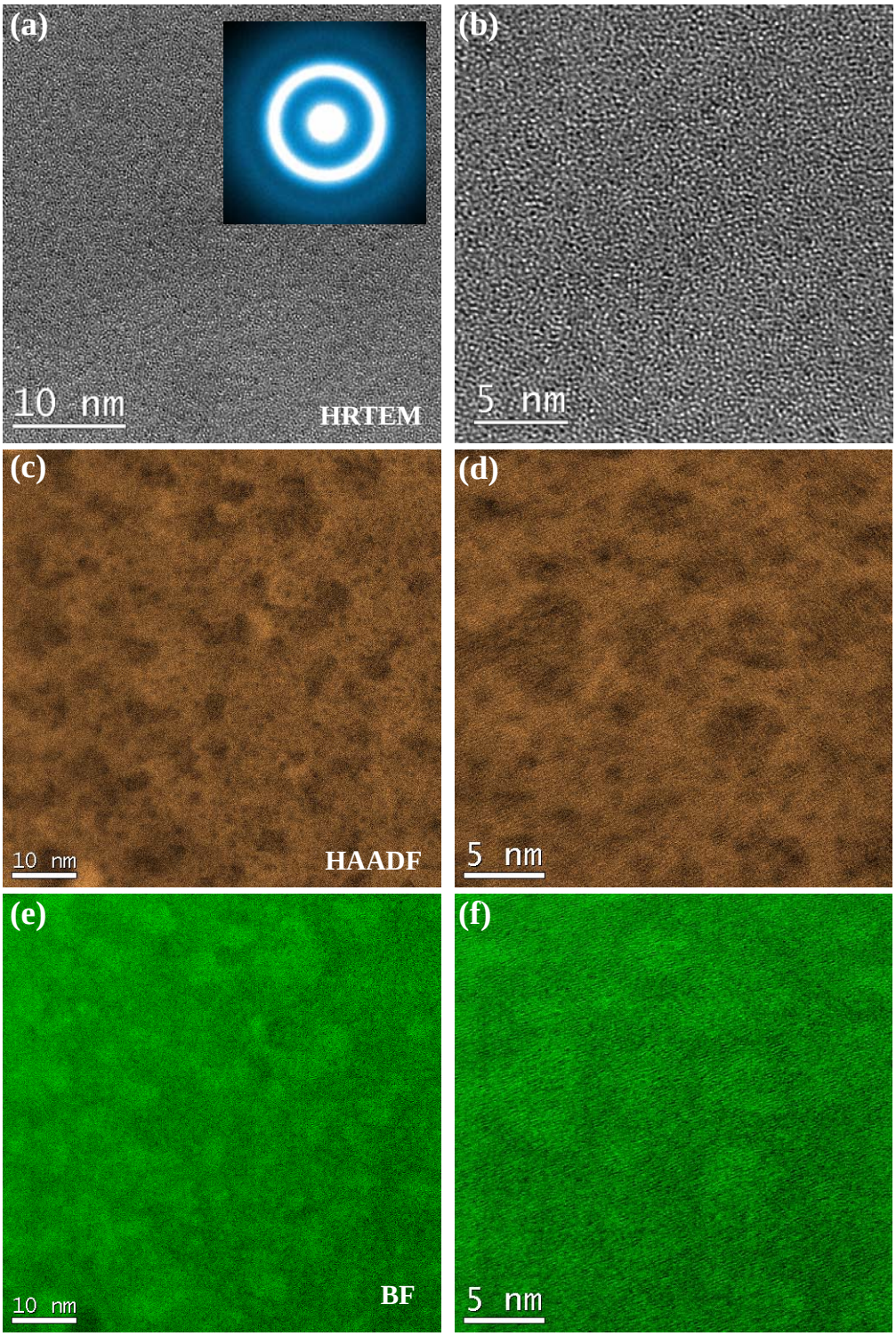

Figure 6.14. TEM images of strong $Zr_{55}Cu_{30}Ni_5Al_{10}$ as-spun ribbon MG. (a), (b) High resolution TEM images. (c), (d) HAADF-STEM images. (e), (f) BF-STEM images. Inset in (a) is the corresponding selected area electron diffraction (SAED). Note that images (c) and (e) are taken simultaneously in one area, so are images (d) and (f).

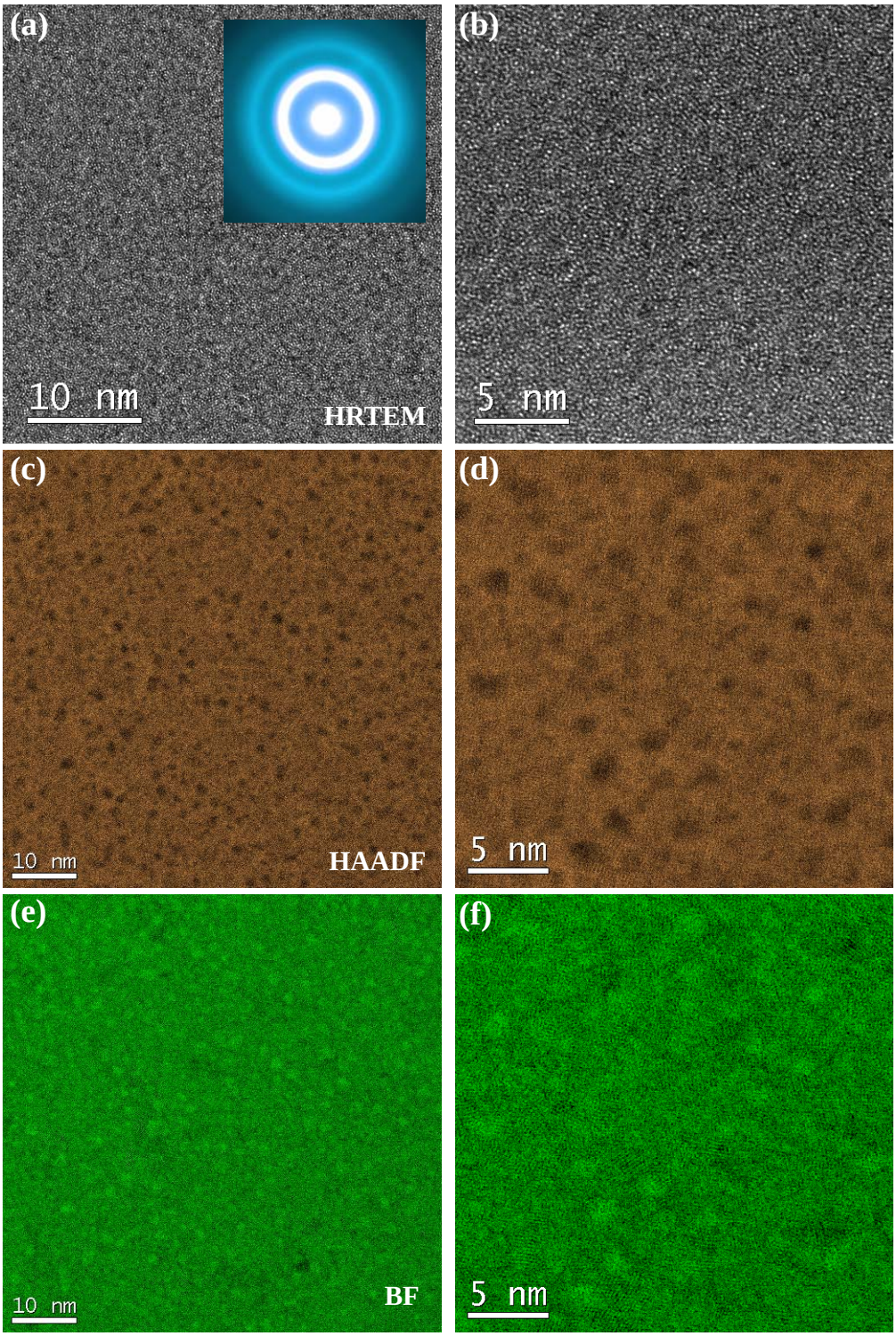

Figure 6.15. TEM images of $Pd_{40}Cu_{40}P_{20}$ as-spun ribbon MG. (a), (b) High resolution TEM images. (c), (d) HAADF-STEM images. (e), (f) BF-STEM images. Inset in (a) is the corresponding selected area electron diffraction (SAED). Note that images (c) and (e) are taken simultaneously in one area, so are images (d) and (f).

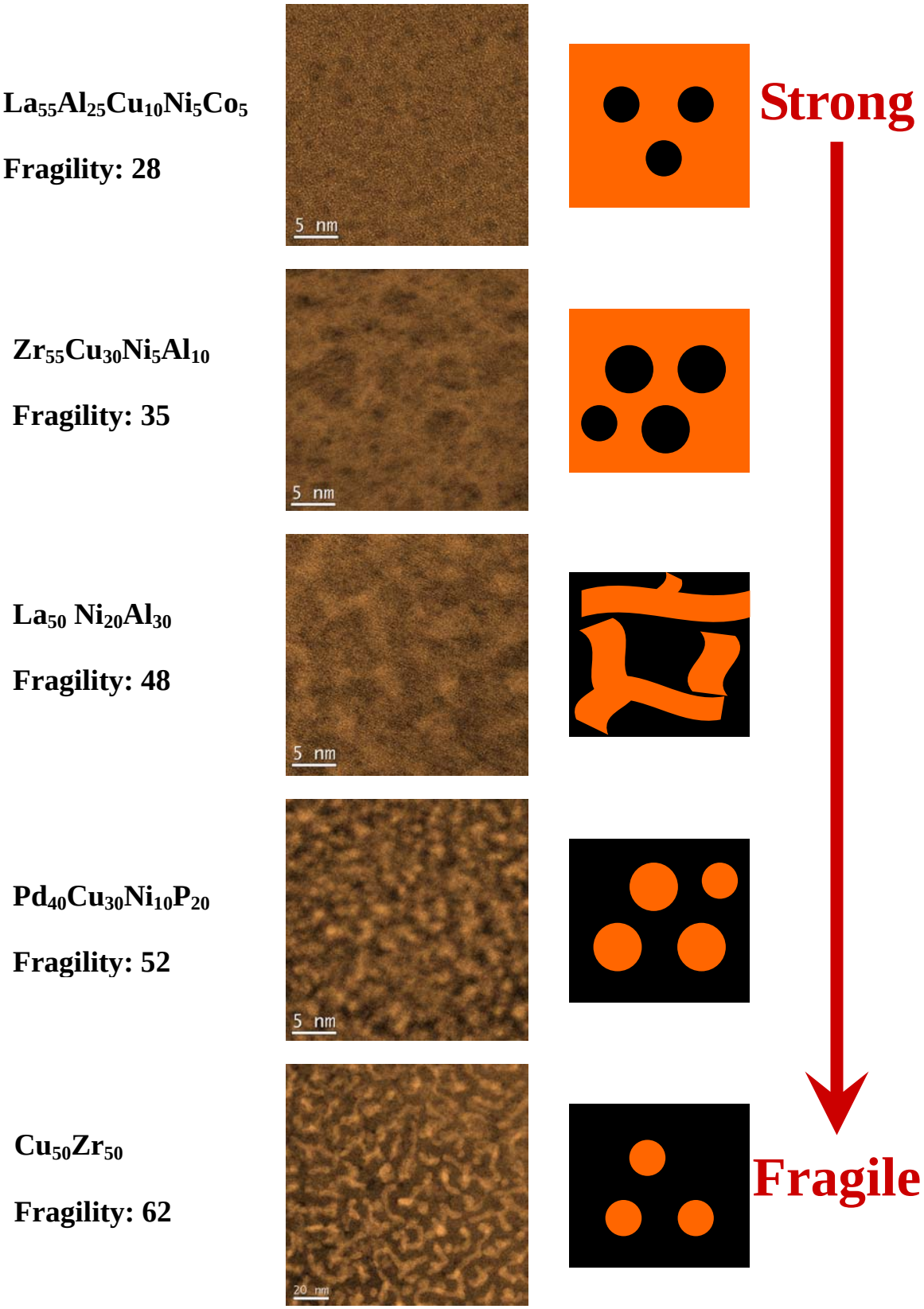

Figure 6.16. STEM images of metallic glasses with different fragility values and their schematics showing the structure features.

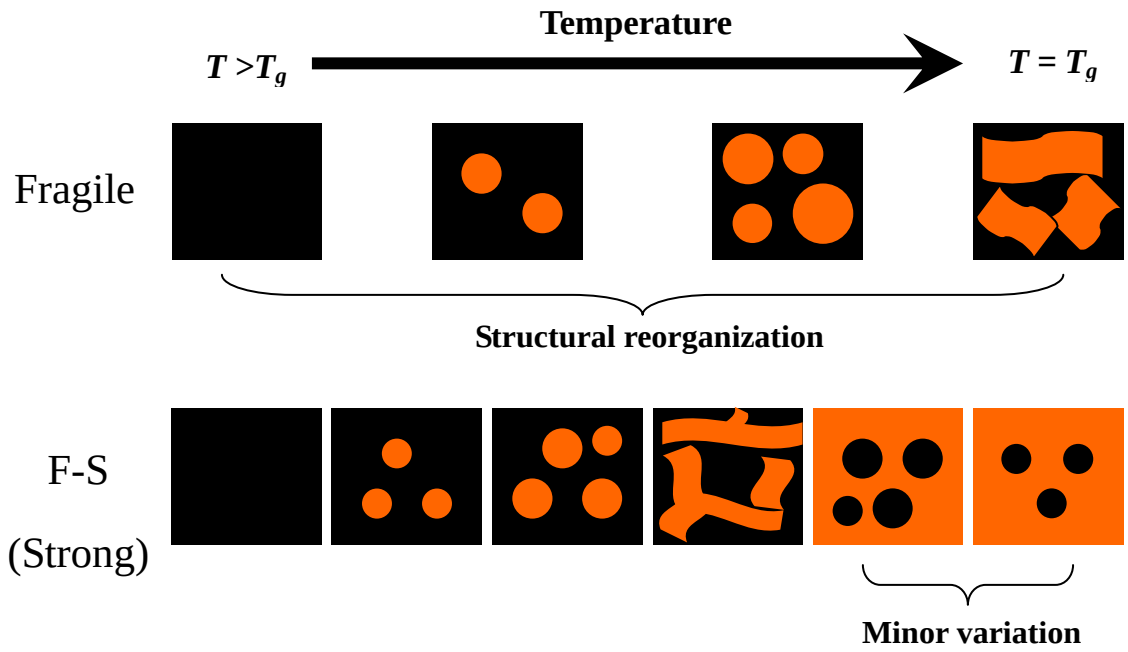

Figure 6.17. Schematic illustrations show the liquid transitions for fragile and strong glass-forming liquids when approached the glass transition temperature from the high temperature. Note that the strong glass-forming liquids were believed to have fragile-strong transition at intermediate temperature.

6.3.4 Correlations with β-relaxation

The β-relaxations detected by dynamic mechanical analysis behave quite differently in various kinds of metallic glasses [10-12]. In the Zr-Cu-Al metallic glasses, only excess wings of β-relaxation can be observed, while in the La-Ni-Al metallic glasses the peaks of β-relaxation appear before the α-relaxation. In chapter 4, we have showed the strong correlations between spatial heterogeneity and β-relaxation. It is still in question how the manifestations of β-relaxation were influenced by the spatial heterogeneity.

The HAADF images for 6 different metallic glasses were exhibited in **Fig. 6.18**. The manifestations of β-relaxations of these MGs measured by DMA were presented in **Table 6.1**. Among these metallic glasses, the La-Ni-Al metallic glass showed the largest spatial heterogeneity around 8 nm (**Fig. 6.18a**), meanwhile it also exhibited the most prominent β-relaxation over other metallic glasses. The Zr-Cu-Ni-Al metallic glass whose β-relaxation was merged with α-relaxation had the extensive heterogeneity around 1 nm associated with a little larger heterogeneity around 5 nm (**Fig. 6.18b**). With the addition of Cu in the Pd-Ni-P metallic glasses, the β-relaxation was enhanced from shoulders to humps. We can see more spatial heterogeneity in the Pd-Cu-Ni-P metallic glass than in the Pd-Ni-P metallic glass (**Fig. 6.18c** and **d**). The β-relaxation in the Zr-Ni-Al metallic glass was stronger than in the Zr-Cu-Al metallic glass which can be explained by the HAADF images that the spatial heterogeneity in Zr-Ni-Al (**Fig. 6.18e**) was around 3 nm while in the Zr-Cu-Al it was around 1.5 nm (**Fig. 6.18f**). The relative intensities of β-relaxations were strongly correlated with the relative volumes of spatial heterogeneities in metallic glasses (**Fig. 6.19**).

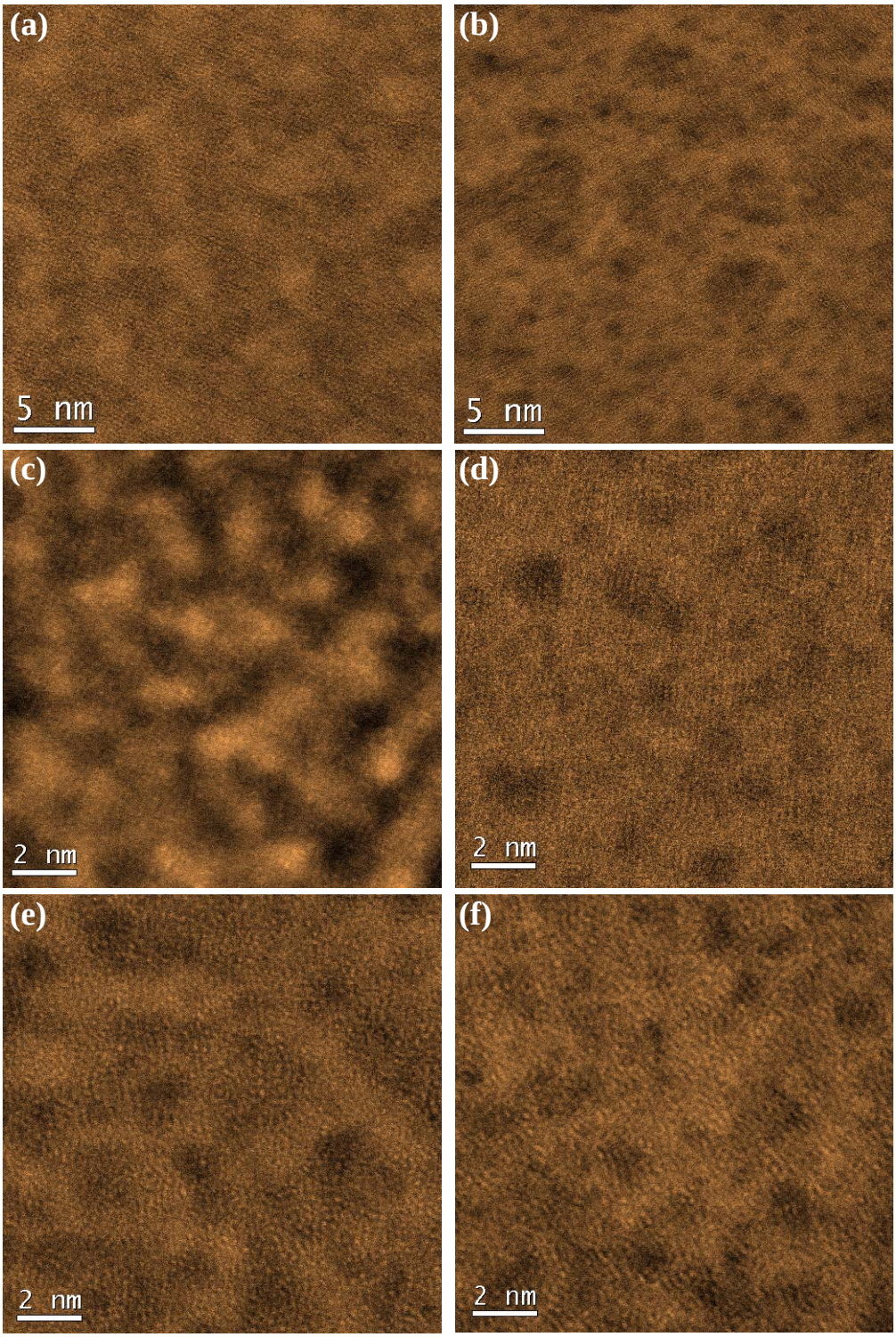

Figure 6.18. HAADF images for (a) La-Ni-Al, (b) Zr-Cu-Ni-Al, (c) Pd-Cu-Ni-P, (d) Pd-Ni-P, (e) Zr-Ni-Al and (f) Zr-Cu-Al as-spun ribbons.

TABLE 6.1. The manifestations of β-relaxations detected by DMA [ref. 10]. The area ratios A_0 and sizes of spatial heterogeneity ξ for six metallic glass systems estimated from the HAADF images in Fig. 6.18. We also defined the D value which is related to the relative intensities of β-relaxation.

	MG systems	β-relaxation	D	A_0 (%)	ξ (nm)
a	La-Ni-Al	Peaks	1	51.7	8
b	Zr-Cu-Ni-Al	Mergence	0	16.6	1
c	Pd-Cu-Ni-P	Humps	0.75	45.8	2
d	Pd-Ni-P	Shoulders	0.5	35.8	2
e	Zr-Ni-Al	Humps	0.75	36.4	3
f	Zr-Cu-Al	Excess wings	0.25	26.9	1.5

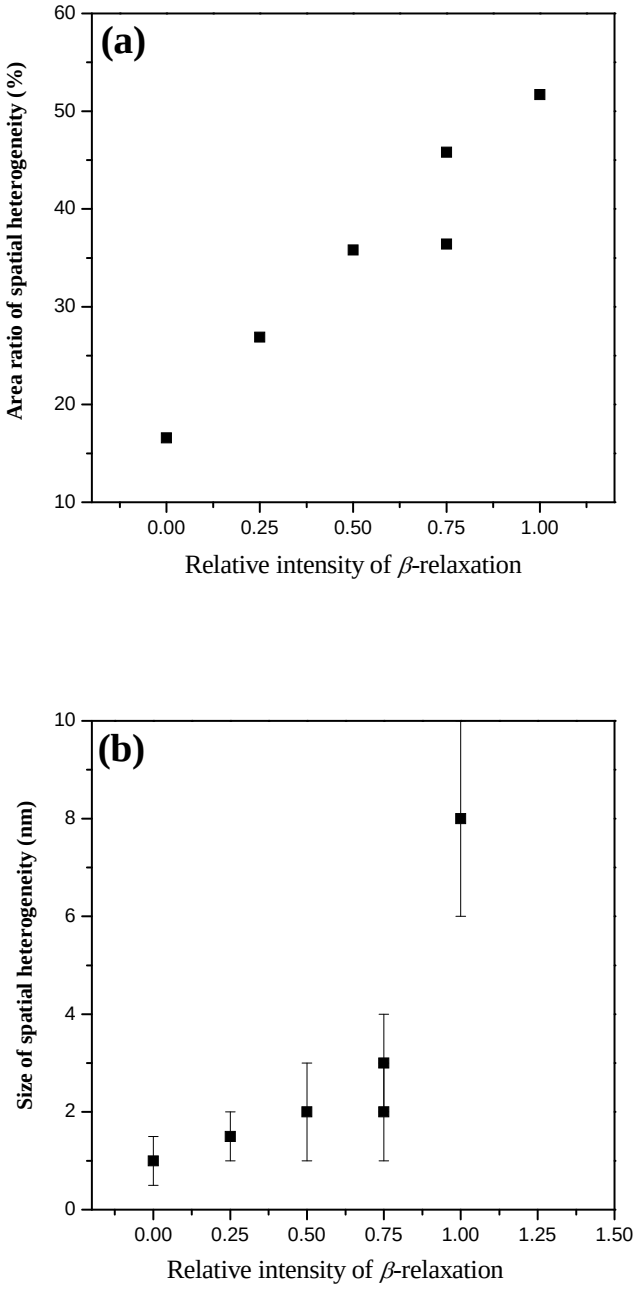

Figure 6.19. Plots of (a) area ratio and (b) size of spatial heterogeneity as a function of the relative intensity of β-relaxation according to Tab 6.1.

6.3.5 Correlations with glass-forming ability

The glass-forming ability is almost the most important issue for the metallic glass community as only the metallic glasses in bulk with large sizes can be used for practical applications [34, 35]. The maximum size of metallic glass has been increased from less than 1 mm to as large as 80 mm for Pt-Cu-Ni-P in 2012 [36-38]. Zr-Cu-Ni-Al is another best glass formers with a critical diameter around 30 mm [39]. Although extensive theories on atomic packing or glass formation have been developed [40-48], however, the search for new compositions of metallic glasses with larger size is still a sequential and time-consuming trial-and-error approach [49].

In **Fig. 6.20** we presented the HAADF images of two best glass formers: (a) Pt-Cu-Ni-P and (b) Zr-Cu-Ni-Al together with two poor glass formers: (c) La-Ni-Al and (d) Cu-Zr. Two features can be derived by the direct comparison between the two groups. First, the volumes of strong regions in the good glass formers were much higher than those in poor glass formers. Also, the strong regions in the good glass formers tend to form particles rather than rods in the poor glass formers. It seems that the high volumes and the isotropic geometry of strong regions can facilitate the formation of metallic glasses. The minor addition of certain elements in some metallic glasses can dramatically enhance their glass-forming ability. For example the addition of 4 at. % Al in $Cu_{50}Zr_{50}$ metallic glass can increase its critical diameter from 2 mm to 5 mm [50]. And the minor addition of Cu and Co can increase the critical diameter of La-Ni-Al metallic glass from around 3 mm to 9 mm [51]. The strong regions in ternary $(Cu_{50}Zr_{50})_{95}Al_5$ evolved from the rods in binary $Cu_{50}Zr_{50}$ (**Fig. 6.20c)** to particles with

the increase in volumes (**Fig. 6.20e)**. Similar trend can be observed in the La-base metallic glasses (**Fig. 6.20d** and **f).** The enhanced glass-forming abilities of Cu-Zr and La-Ni-Al metallic glasses by minor additions confirmed our conclusion that the good glass forms should have high volumes of strong regions with isotropic geometries.

A. Inoue *et al.* [52] has proposed a criterion for the glass-forming ability $\Delta T_{xg} = T_x - T_g$, where T_x is the onset crystallization temperature and T_g the glass transition temperature. The glass former with a larger supercooled liquid range ΔT_{xg} was believed to have a better glass-forming ability [45]. With the acceleration of electricity for 20 hours, the $Pd_{40}Ni_{40}P_{20}$ metallic glass was found to partially crystallize at the location of spatial heterogeneity (**Fig. 6.21**). Thus we suggest that the spatial heterogeneity plays as the initiation of crystallization upon heating near T_x. During the devitrification, the strong regions in the metallic glass need to first transfer to the weak regions and then crystallize. So the span of the supercooled liquid region is proportional to the volumes of strong regions and the difficulties of the transition as expressed by $\Delta T_{xg} = T_x - T_g = \delta(\rho_s - \rho_w)V_s$, where the δ is the dynamic factor, ρ_s is the density of strong regions, ρ_w is the density of weak regions and V_s is the volumes of strong regions. δ is related to the diffusion, viscosity, geometry and other factors that can influence the glass-forming ability. We noticed that the supercooled liquid range criterion could not account for the glass-forming abilities for some metallic glasses [45]. The glass formation is a complicated phenomenon which also involves with the atomic packing and the viscosities of supercooled liquids etc., and more work is needed to clarify the origin of glass formation for metallic glasses.

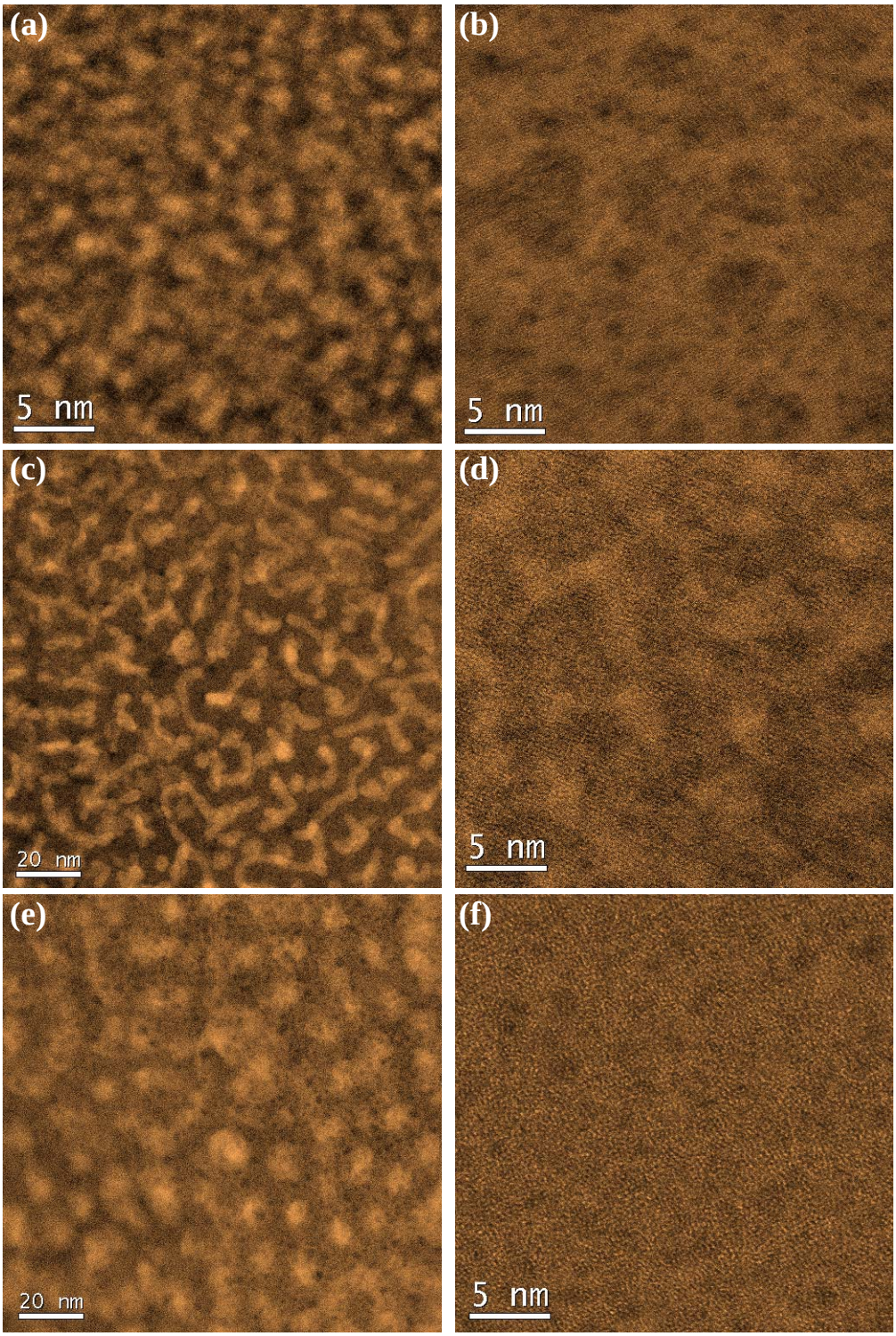

Figure 6.20. HAADF images for (a) Pd-Cu-Ni-P (Z_c = 80 mm), (b) Zr-Cu-Ni-Al (Z_c = 30 mm), (c) Cu-Zr (Z_c = 2 mm), (d) La-Ni-Al (Z_c = 3 mm), (e) Cu-Zr-Al (Z_c = 5 mm) and (f) La-Al-Cu-Ni-Co (Z_c = 9 mm). Z_c is the criticle diameter of metallic glass.

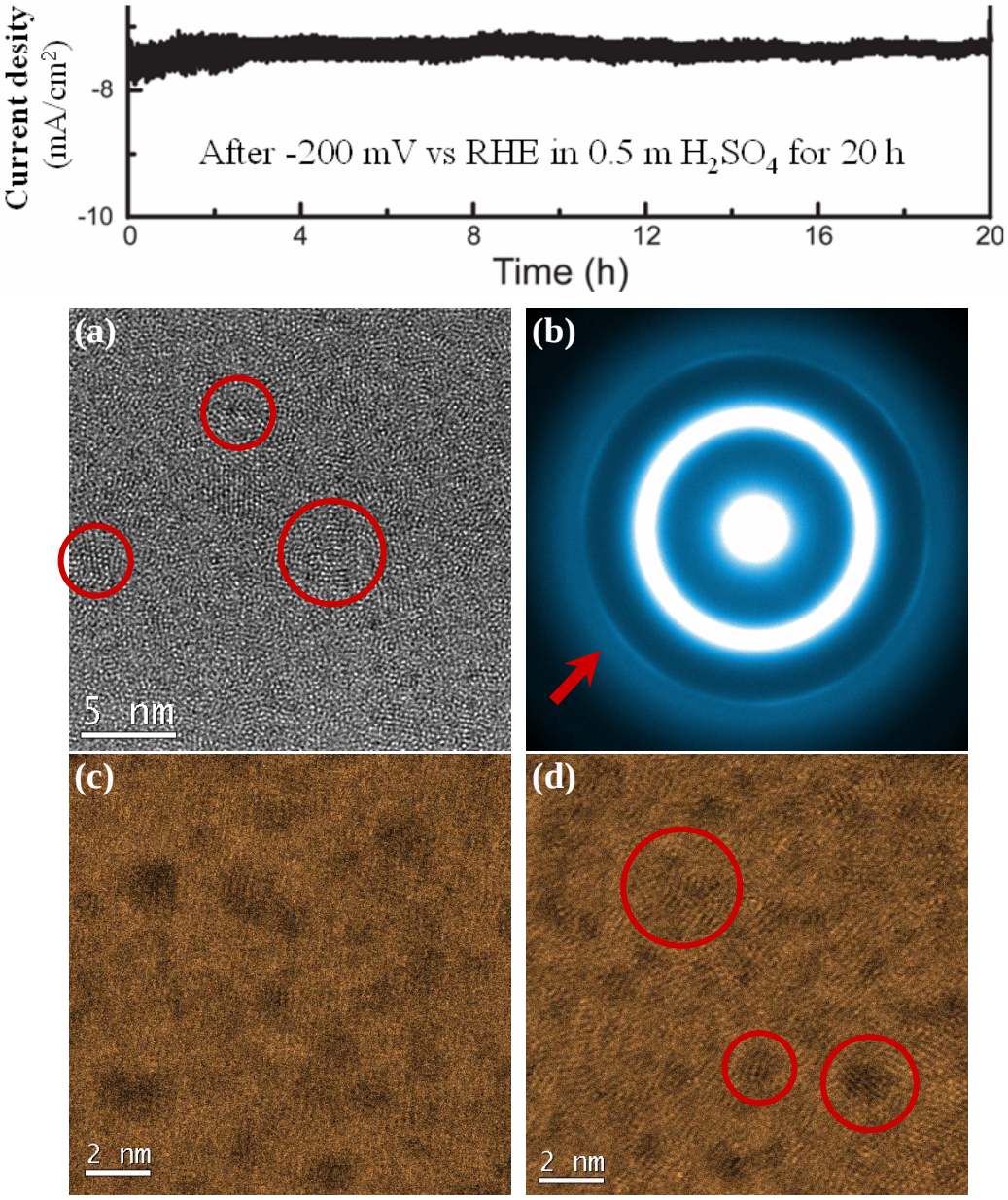

Figure 6.21. The partial crystallization occurred in the $Pd_{40}Ni_{40}P_{20}$ metallic glass after applying electricity for 20 hours. (a) The HRTEM image and the corresponding electron diffraction indicated the traces of partial crystallization. HAADF images (c) before and (d) the partial crystallization implied that the crystallization initiated at the spatial heterogeneities (weak regions).

6.3.6 Local atomic ordering

The ABED mapping (**Fig. 6.22**) was performed to check the atomic ordering of the hyper-quenched metallic glass and the glasses relaxed at 553 K for 720 min [15, 16]. Although we tried the ABED scanning many times on the hyper-quenched metallic glass, little symmetric diffraction patterns can be observed. However, the ABED mapping formed by selecting the different parts of diffraction patterns showed clear difference between them. **Fig. 6. 23a** is the ADF-STEM image of the region for ABED scanning. A spatial heterogeneity can be observed to locate at the center of region. The ABED mapping formed by selecting the first ring of diffraction halos (**Fig. 6.23b**) was relatively uniform and showed little contrast correlated with the spatial heterogeneity. However, the ABED mapping formed by selecting the second ring of diffraction halos (**Fig. 6.23c**) showed less intensity of the diffraction from the spatial heterogeneity. According to the ABED results, the spatial heterogeneity mainly contributed to the structural disordering, while the matrix of strong regions contributed to the short-range ordering in metallic glasses.

After the sub-T_g relaxation at 553 K for 720 min, the diffraction patterns coming from the icosahera clusters can be extensively observed in the sample (**Fig. 6.24**). Thus, we concluded that the atomic packing in the spatial heterogeneity was more disordered than the surroundings, and the enthalpy relaxation will decrease the volumes of the disordered regions and facilitate the growth of icosahedra clusters which has been reported by J. Saida *et al.* [19].

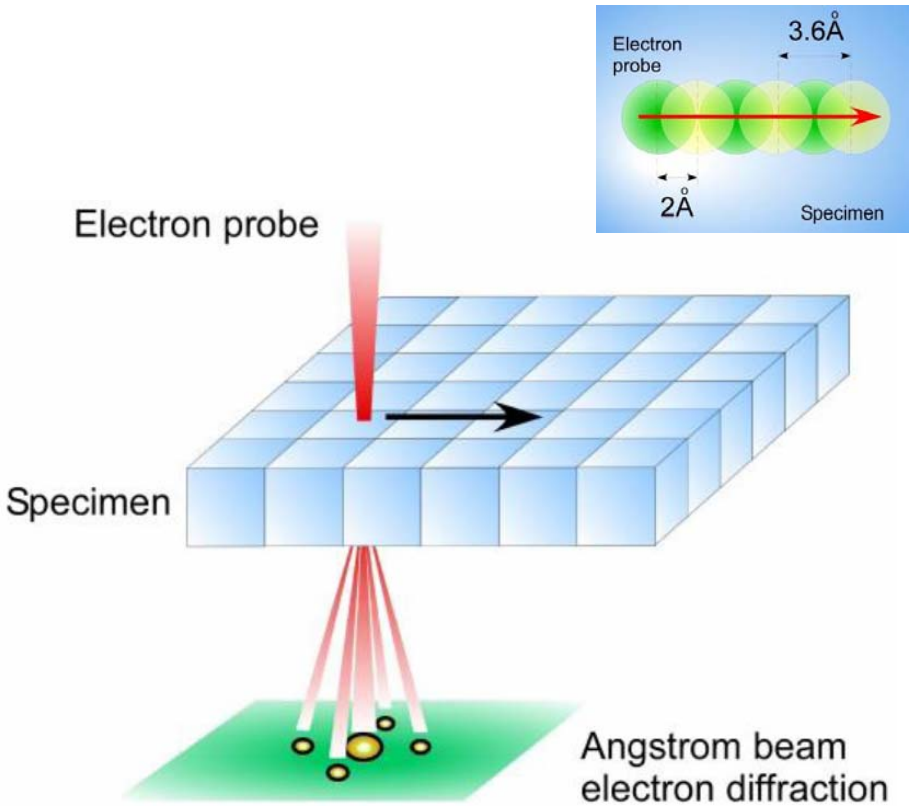

Figure 6.22. Schematic illustration of ABED mapping. A nearly parallel electron beam with a FWHM diameter of 0.36 nm was probed to scan a thin metallic glass foil in two dimensions with a scanning step of ~0.2 nm. During the scanning a series of local electron diffraction patterns are acquired as a 2D image with the positioning information (x and y axis). Each pixel (0.2 nm×0.2 nm) in the 2D image corresponds to one ABED pattern.

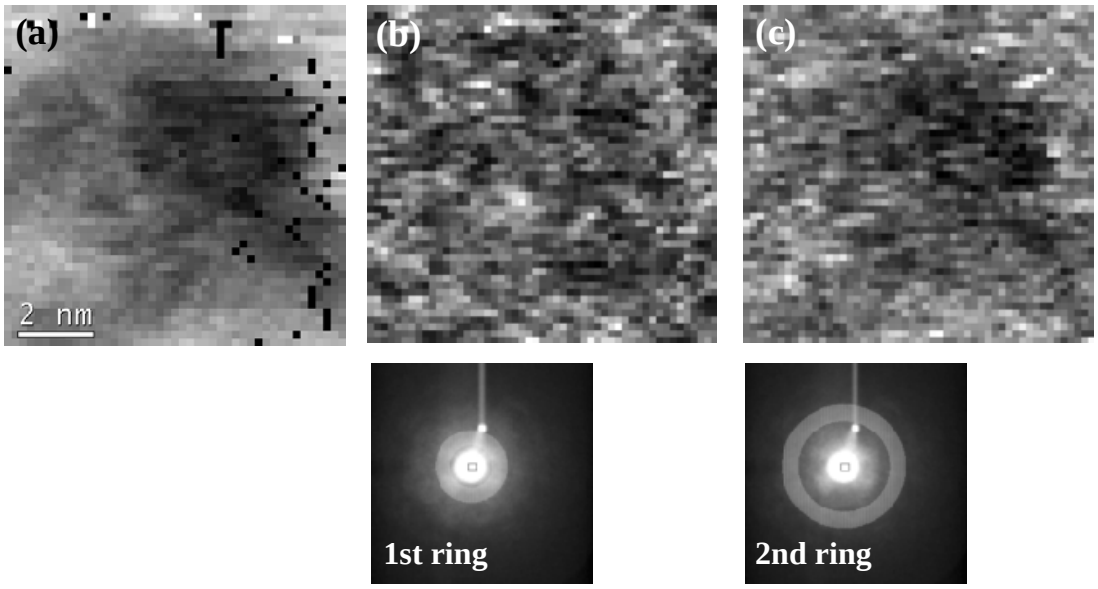

Figure 6.23. (a) HAADF-STEM image and its corresponding ABED mapping formed by selecting (b) the 1st ring of the diffraction halo and (c) the 2nd ring of the diffraction halo.

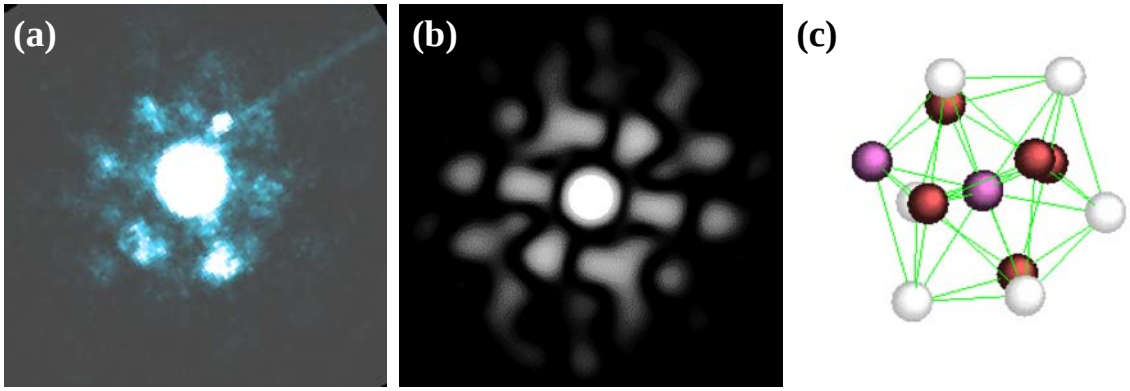

Figure 6.24. (a) ABED experimental data; (b) ABED simulation and (c) the atomic packing of Al-centered icosahedra $<0\ 0\ 12\ 0>$.

6.4 Summary

In this chapter, the STEM was introduced to characterize the spatial heterogeneities in metallic glasses. The spatial heterogeneities observed by STEM agree well with the results measured by the AM-AFM (see chapter 4) for both the hyper-quenched metallic glass and La-Ni-Al as-spun ribbons before and after the enthalpy relaxation. The spatial heterogeneity was proven to be intrinsic and come from the density or thickness variations. Using the STEM, we systematically investigate the Zr-base, Pd-base, La-base and Cu-base metallic glasses, demonstrating the difference in geometry of spatial heterogeneity for strong and fragile metallic glasses. The relative intensity of β-relaxation to α-relaxation was found to be strongly correlated with the sizes or volumes of spatial heterogeneity in metallic glasses. The volumes and geometry of the strong regions and spatial heterogeneity also influenced the glass-forming abilities of metallic glasses. The ABED indicated that the atomic packing in the spatial heterogeneity was more disordered than the remaining part in metallic glasses. After sub-T_g relaxation, diffraction patterns corresponding to icosahedra can be observed.

Our method provides a direct characterization tool to see the spatial heterogeneity, the basic structure units in metallic glass that determine the relaxations (chapter 3), mechanical properties (chapter 5), fragilities (chapter 6) and glass-forming ability (chapter 6) of metallic glasses. It gives metallic glasses, whose structure was thought to be amorphous before, a microstructure which will facilitate the investigation of metallic glasses and the fabrication of novel metallic glasses with superior properties.

References

[1] P. G. Debenedetti, and F. H. Stillinger, Nature 410, 259 (2001).

[2] M. D. Ediger, Annu. Rev. Phys. Chem. 51, 99 (2000).

[3] G. P. Johari, J. Non-crystal. Solids. 307, 317 (2002).

[4] Z. Wang, B. A. Sun, H. Y. Bai and W. H. Wang, Nature Commun. 5, 5823 (2014).

[5] A. S. Argon, Acta Metall. 27, 47 (1979).

[6] M. L. Falk and J. S. Langer, Phys. Rev. E 57, 7192 (1998).

[7] W. L. Johnson, and K. Samwer, Phys. Rev. Lett. 95, 195501 (2005).

[8] D. Pan, A. Inoue, T. Sakurai, and M. W. Chen, Proc. Natl. Acad. Sci. U.S.A. 105, 14769 (2008).

[9] W. H. Wang, J. Appl. Phys. 110, 053521 (2011).

[10] H. B. Yu, K. Samwer, W. H. Wang and H. Y. Bai, Nature Commun. 4, 2204 (2013).

[11] H. B. Yu, W. H. Wang, K. Samwer, Mater. Today 16, 183 (2013).

[12] H. B. Yu, W. H. Wang, H. Y. Bai, and K. Samwer, Natl. Sci. Rev. 1, 429-461 (2014).

[13] T. Ichitsubo, E.Matsubara, T. Yamamoto, H. S. Chen, N. Nishiyama, J. Saida, and K. Anazawa, Phys. Rev. Lett. 95, 245501 (2005).

[14] T. Ichitsubo, H. Kato, E. Matsubara, S. Biwa, S. Hosokawa, K. Matsuda, H. Uchiyama, and A. Q. R. baron, J. Non-Cryst. Solids 357, 494 (2011).

[15] A. Hirata, P. F. Guan, T. Fujita, Y. Hirotsu, A. Inoue, A. R. Yavari, and M. W. Chen, Nature Mater. 10, 28 (2011).

[16] A. Hirata, L. J. Kang, T. Fujita, B. Klumov, K. Matsue, A. R. Yavari and M. W. Chen, Science 341, 376 (2013).

[17] H. Wagner, D. Bedorf, S. Küchemann, M. Schwabe, B. Zhang, W. Arnold, and K. Samwer, Nature Mater. **10**, 439 (2011).

[18] Y. H. Liu, D. Wang, K. Nakajima, W. Zhang, A. Hirata, T. Nishi, A. Inoue and M. W. Chen, Phys. Rev. Lett. 106, 125504 (2011).

[19] J. Saida, M. Matsushita, and A. Inoue, Appl. Phys. Lett. 79, 412 (2001).

[20] B. B. Sun, Y. B. Wang, J. Wen, H. Yang, M. L. Sui, J. Q. Wang and E. Ma, Scripta Mater. 53, 805 (2005).

[21] T. Miyauchi, H. Kato, and E. Abe, Mater. Res. Lett. 2, 94 (2014).

[22] C. A. Angell, K. L. Ngai, G. B. McKenna, P. F. McMillan and S. W. Martin, J. Appl. Phys. 88, 3113 (2000).

[23] C. A. Angell, J. Non-Cryst. Solids 131, 13 (1991).

[24] J. L. Green, K. Ito, K. Xu and C. A. Angell, J. Phys. Chem. B 103, 3991 (1999).

[25] C. A. Angell, Science, 267, 1924 (1995).

[26] W. H. Wang, Prog. Mater. Sci. 57, 487 (2012).

[27] Z. Wang, H. B. Yu, P. Wen, H. Y. Bai, and W. H. Wang, J. Phys. Condens. Matter 23, 142202 (2011).

[28] C. Z. Zhang, L. N. Hu, Y. Z. Yue, and J. C. Mauro, J. Chem. Phys. 133, 014508 (2010).

[29] N. A. Mauro, A. J. Vogt, M. L. Johnson, J. C. Bendert, and K. F. Kelton, Appl. Phys. Lett. 103, 021903 (2013).

[30] C. Zhou, L. N. Hu, Q. Sun, J. Y. Qin, X. F. Bian, and Y. Z. Yue, Appl. Phys. Lett. 103, 171904 (2013).

[31] C. Zhou, L. N. Hu, Q. Sun, H. J. Zheng, C. Z. Zhang, and Y. Z. Yue, J. Chem. Phys. 142, 064508 (2015).

[32] Z. Evenson, T. Schmitt, M. Nicola, I. Gallino, and R. Busch, Acta Mater. 60, 4712 (2012).

[33] S. Wei, F. Yang, J. Bednarcik, I. Kaban, O. Shuleshova, A. Meyer, and R. Busch, Nat. Commun. 4, 2083 (2013).

[34] A. Inoue, Atca Mater. 48, 279 (2000).

[35] W. L. Johnson, MRS Bull. 24, 42 (1999).

[36] A. Inoue, N. Nishiyama, and H. M. Kimura, Mater. Trans. JIM 38, 179 (1997).

[37] M. Telford, Mater. Today 7, 36 (2004).

[38] N. Nishiyama, K. Takenaka, H. Miura, N. Saidoh, Y. Zeng, and A. Inoue, Intermetallics 30, 19 (2012).

[39] A. Inoue, and T. Zhang, Mater. Trans. JIM 37, 185 (1996).

[40] H. W. Sheng, W. K. Luo, F. M. Alamgir, J. M. Bai, and E. Ma, Nature 439, 419 (2006)

[41] D. Turnbull, Contemp. Phys. 10, 473 (1969).

[42] D. B. Miracle, Nature Mater. 3, 697–702 (2004).

[43] T. Fujita, K. Konno, W. Zhang, V. Kumar, M. Matruura, A. Inoue, T. Sakurai, and M. W. Chen, Phys. Rev. Lett. 103, 075502 (2009).

[44] T. Egami, Mater. Sci. Eng. A 226, 261–267 (1997).

[45] Z. P. Lu, and C. T. Liu, Acta Mater. 50, 3501 (2002).

[46] Y. Li, , Q. Guo, , J. A. Kalb, and C. V.Thompson, Science 322, 1816 (2008).

[47] E. S. Park, and D. H. Kim, Appl. Phys. Lett. 92, 091915 (2008).

[48] J. C. Bendert, A. K. Gangopadhyay, N. A. Mauro, and K. F. Kelton, Phys. Rev. Lett. 109, 185901 (2012).

[49] S. Ding, Y. H. Liu, Y. L. Li, Z. Liu, S. Sohn, F. J. Walker, and J. Schroers, Nature Mater. 13, 494 (2014).

[50] W.H.Wang, Prog. Mater. Sci. 52, 540 (2007).

[51] A. Inoue, T. Nakamura, T. Sugita, T. Zhang, and T. Masumoto, Mater. Trans. JIM 34, 351 (1993).

[52] A. Inoue, T. Zhang, and T. Masumoto, J. Non-Cryst. Solids 156, 473 (1993).

Chapter 7

Conclusions

Starting from the sub-T_g relaxation processed by β-relaxations in a hyper-quenched metallic glass, we performed AM-AFM, Nanoindentation and TEM on the hyper-quenched metallic glass whose β-relaxation could be "tuned" gradually to investigate the correlations of β-relaxations with the spatial heterogeneity and mechanical properties in metallic glasses.

Chapter 3: The enthalpy relaxation below $0.8T_g$ or sub-T_g relaxation in the hyper-quenched metallic glass was linked with the β-relaxation. The excess enthalpy trapped in the hyper-quenched metallic glass was successively released by annealing the samples at high temperatures T_a below T_g for different durations. The process can be well expressed by the KWW function from which the characteristic relaxation time for the sub-T_g relaxation can be derived. The characteristic relaxation time became shorter at higher T_a implying it as a thermo-activated process. According to the Arrhenius equation, the activation energy was calculated to be $27.2RT_g$ which was in accord with the empirical value of β-relaxations. The extrapolation of the plot to the glass transition temperature gave a characteristic relaxation time merging with the α-relaxation, another feature of β-relaxation. The above results proved that the sub-T_g relaxation was processed by β-relaxation.

Chapter 4: The evolution of spatial heterogeneity during the sub-T_g relaxation was measured by AM-AFM. The hyper-quenched metallic glasses were relaxed below T_g, and the spatial heterogeneity was sequentially decreased from around 6.1 nm for the hyper-quenched one to around 2.59 nm for the most relaxed one. The shrinkage of the spatial heterogeneity behaved as a relaxation process. We used KWW function to derive the characteristic relaxation time for the process. The activation energy for the evolution was calculated to be $25.1RT_g$ almost the same as the β-relaxation. The evolution of spatial heterogeneity was correlated with the β-relaxation.

Chapter 5: The effects of sub-T_g relaxation on the mechanical properties of metallic glasses were investigated. The hardness and modulus of the metallic glasses gradually increased after the sub-T_g relaxation. The creep in the relaxed metallic glass became inferior and slower. The activation energy for the creep derived from the CSM model indicated that the anelastic deformation in metallic glass was strongly correlated with the β-relaxation.

Chapter 6: The STEM was proven to be a useful tool to directly see the spatial heterogeneity in metallic glasses. The sizes of heterogeneity observed by STEM were comparable with those measured by AM-AFM. The strong Zr-Cu-Ni-Al metallic glass showed a black-in-white feature, while the fragile Pd-Cu-Ni-P metallic glass exhibited the opposite white-in-black feature. The intermediate La-Ni-Al showed a structure of interpenetration between them. The metallic glasses with higher volumes of spatial

heterogeneity were found to have more prominent β-relaxations. The metallic glasses with high glass-forming ability have large volumes of strong regions with isotropic geometry. Base on the above observations, the β-relations were determined to be relics of the frozen liquids. With the STEM observation of spatial heterogeneity, more structural origins of properties of metallic glasses can be revealed.

In general, we put three aspects of metallic glasses together: their relaxations, spatial heterogeneity and mechanical properties. What make the materials different from the matter are their microstructures. For conventional metals and alloys, their grain boundaries or dislocations can be used to predict the strength or other properties. For metallic glasses, such microstructure was missing until this work which gives metallic glasses a fingerprint of their properties. Our work will help the better understanding of dynamics and mechanical behaviors of metallic glasses and accelerate the production of novel metallic glasses with superior properties.

Acknowledgements

When I was a child, I thought the scientists were the pioneers of human beings. As I grow up, this mind never changes. Great thanks to my supervisor Prof. Mingwei Chen who gives me a chance to catch that dream to be one of them. Prof. Chen has broad and deep horizons of knowledge on science. He is a captain of the lab who knows the right direction to the wealth of science, and helps me go deep into it. Under his supervising, I take systematic academic training to learn the knowledge, the operation of devices and the methodology of doing high-quality researches which will be the precious for my future academic life. The thesis is finished under his supervising.

I am grateful to the thesis committee members: Prof. Mingwei Chen, Prof. Junji Saida and Prof. Hidemi Kato for their invaluable time and helpful suggestions on my thesis. Prof. Saida is highly appreciated for his important suggestion on the local structures of metallic glasses. Prof. Kato is highly appreciated for his enlightening suggestion on the correlations of fragility and the glass-forming abilities with the spatial heterogeneity in metallic glasses.

Special thanks to Assoc. Prof. Akihiko Hirata, Assoc. Prof. Takeshi Fujita and Dr. Daisman Aji who teach me the fundamental knowledge and the operation of devices. I also want to thank Dr. Yanhui Liu and Dr. S. X. Song. Although I don’t meet you, you teach me much. More special thanks to Assist. Prof. Y. Ito, Dr. P. Liu, Mr. J. H. Han, and Mr. Z. Q. Wang who take pleasures for my daily life. I am very thankful to Ms. C.

Cheng for her help during the daily life and important suggestions on preparing for the thesis and defense.

The members and staffs of Chen's lab are highly appreciated. They are Assist. Prof. L. Y. Chen, Dr. K. M. Reddy, Dr. L. Zhang, Dr. X. B. Ge, Dr. H. Wang, Dr. Y. W. Tan, Dr. X. W. Guo, Dr. Z. L. Wang , Mr. X. D. Xu, Mr. C. Li, Dr. K. M. Ji, Dr. Y. Hou, Dr. Y. R. Wen, Dr. L. J. Kang, Mr. H. Kashani and Ms. Aso.

Prof. T. G. Nieh and Prof. J .S. Langer are highly appreciated who shared their thoughts about life and researches with me. Prof. W. H. Wang, Prof. Y. Z. Yue, Prof. Y. Wu, Prof. J. Xu and Prof. D. Pan are acknowledged for their enlightening discussions.

At last I want to express deep gratitude to my parents and grandparents who raise me, give me power when I suffer, and support me to go abroad to finish the Ph.D. study. I want to say sorry to my wife Yu Wang. Thanks for your understanding, tolerance and support across the East China Sea, and I will get along with you for the rest of my life.